

ANALYSIS OF IRRADIATION INDUCED DEFECTS ON CARBON NANOSTRUCTURES
AND THEIR INFLUENCES ON NANOMECHANICAL AND MORPHOLOGICAL
PROPERTIES USING MOLECULAR DYNAMICS SIMULATION

By

SHARON KAY PREGLER

A DISSERTATION PRESENTED TO THE GRADUATE SCHOOL
OF THE UNIVERSITY OF FLORIDA IN PARTIAL FULFILLMENT
OF THE REQUIREMENTS FOR THE DEGREE OF
DOCTOR OF PHILOSOPHY

UNIVERSITY OF FLORIDA

2008

© 2008 Sharon Kay Pregler

To my family and friends with love and gratitude

ACKNOWLEDGMENTS

I would like to express my sincere gratitude to Prof. Susan Sinnott, for her encouragement and support during my graduate career. Her guidance and optimism has helped me accomplish my goals and tackle obstacles in academic research. I would also like to thank Prof. Simon Phillpot for guidance and valuable ideas on my research. Their care and enthusiasm for the members of the Computational Focus Group have truly made my last years at the University of Florida memorable and fulfilling. I would also like to acknowledge my supervisory committee, Prof. Jiangeng Xue, Prof. Wolfgang Sigmund, and Prof. Nam-Ho Kim, for their advice and support.

I would also like to thank the members and graduated members of the computational focus group as well as fellow department colleagues, Abby Queale, Jillian Leifer, and Sean Bishop. Their encouragement and support especially during rough times have greatly impacted my time at UF.

Especially, I show my deepest gratitude and appreciation to my parents, John and Norma Pregler, who have been compassionate and understanding throughout my collegiate studies.

TABLE OF CONTENTS

	<u>page</u>
ACKNOWLEDGMENTS	4
LIST OF TABLES.....	7
LIST OF FIGURES	8
ABSTRACT.....	10
 CHAPTER	
1 INTRODUCTION	13
General Introduction.....	13
Carbon Nanostructures	13
Graphene and Graphite.....	14
Fullerenes	16
Carbon Nanotubes	17
<i>Structure and chirality</i>	17
<i>Mechanical properties and sword-in-sheath deformation</i>	19
Composites	20
<i>Polymer as the composite matrix</i>	21
<i>Carbon nanostructured based composites</i>	23
Interfacial Engineering of Nanocomposites	24
Irradiation Effects in Carbon Systems and Composites	27
Graphite	28
Fullerenes and Carbon Onions	29
Carbon Nanotubes	30
Composites	32
Photovoltaic Applications of Fullerenes and Hydrocarbons	34
2 COMPUTATIONAL METHODS	40
Classical Molecular Dynamics	40
Reactive Bond Order Potential	41
Lennard Jones Potential	46
Adaptive Intermolecular Reactive Bond Order Potential	47
Periodic Boundary Conditions.....	49
Predictor Corrector Algorithm.....	50
Langevin Thermostats	52
Primary Knock on Atoms	53
3 ARGON IRRADIATION ON GRAPHITE AND EVOLUTION OF DEFECTS	57
System Setup	57

Experiment	57
Computation	58
Irradiation Results.....	59
Defect Analysis.....	61
Conclusions.....	65
4 IRRADIATION AND AXIAL PULLOUT EFFECTS ON MWNTS.....	72
System Background	72
Results.....	74
Irradiation	74
Pullout.....	76
Conclusions.....	79
5 ARGON BEAM MODIFICATION OF NANOTUBE BASED COMPOSITES	87
System Background	87
Results.....	88
Effects on Irradiation	88
Nanotube Pullout Analysis	92
Conclusions.....	94
6 MOLECULAR DYNAMICS AND MONTE CARLO STRUCTURE EVALUATION WITH ORGANIC SEMICONDUCTORS	101
System Background	101
Ordered Structures.....	102
Random Structures	103
Equilibration Using Molecular Dynamics.....	105
Results.....	106
Phase Separation in Pentacene:C ₆₀ Mixtures	106
Controlling Film Morphology	109
Conclusions.....	111
7 GENERAL CONCLUSIONS	120
LIST OF REFERENCES	123
BIOGRAPHICAL SKETCH	132

LIST OF TABLES

<u>Table</u>	<u>page</u>
3-1 Defect formation energies of defects observed in graphite after Ar irradiation	66
4-1 The hybridization of the carbon atoms in MWNTs following irradiation.	81
5-1 Angle effects of the incident beam during C ₃ F ₅ irradiation.	96
6-1 Cohesive energies calculated by AIREBO compared to experiment.	112

LIST OF FIGURES

<u>Figure</u>	<u>page</u>
1-1 Graphene being transformed into a fullerene, carbon nanotube, and graphite.....	36
1-2 Graphene plane with directional vectors mapping the carbon nanotube	36
1-3 Radial and axial views of armchair, chiral, and zig zag nanotubes.....	37
1-4 Mechanisms and micrograph images of fracture mechanisms in a nanotube composite.....	38
1-5 Aggregation of self interstitials in graphite as a result of irradiation	38
1-6 Organic photovoltaic semiconductors	39
2-1 Orthogonal periodic boundary conditions	56
2-2 Energetic particle bombardment, describing primary knock on behavior in irridiation.....	56
3-1 STM image of graphite surface irradiated by Ar ⁺ at the collision energy of 50±5 eV.....	67
3-2 Distribution of the apparent diameter of the defects measured by STM.....	68
3-3 Side view of graphite during Ar irradiation.....	68
3-4 Top view of graphite during Ar irradiation	69
3-5 Irradiation damage in graphite.....	69
3-6 Percentage of <i>sp</i> ³ - and <i>sp</i> -hybridized carbon atoms in graphite system after irradiation.....	70
3-7 Snapshot of cross-link defects in graphite	70
3-8 Snapshots illustrating the formation of a Stone Wales defect	71
4-1 Side view snapshots of Ar irradiated MWNTs.....	81
4-2 Side view snapshots of CF ₃ irradiated MWNTs.....	82
4-3 Crosslink count from the processes of CF ₃ and Ar impact during irradiation.....	82
4-4 Side view snapshots of electron irradiated MWNTs	83
4-5 Pullout of electron-irradiated, Ar-irradiated MWNT, and pristine MWNT	84
4-6 Pullout of the innermost shell at 40 m/s of the FRMWNT and the HRMWNT	85
4-7 Pullout of irradiated MWNT compared to FRMWNT and HRMWNT	85

4-8 Effect of pullout rate on the electron irradiated MWNT	86
5-1 Nanocomposite structures of bundle, B) DWNT, and C) SWNT before irradiation.	97
5-2 Snapshots of bundle, DWNT, and SWNT composites after Ar irradiation	97
5-3 Hybridization analysis of CNT damage under Ar irradiation.	98
5-4 Average number of trapped Ar atoms.	98
5-5 Effects of curvature in irradiation damage between DWNT and SWNT bundles	99
5-6 Average masses of the polymer products after irradiation and equilibration.....	99
5-7 Pullout load curves of CNT-PS composites after irradiation	100
6-1 Plot of interfacial energy between (100) surfaces of FCC C ₆₀ and (100) Pentacene.	112
6-2 Pentacene:C ₆₀ (1:1) molar ratios of structures that were built by the ordered method	113
6-3 Model of pentacene:C ₆₀ (6:1) molar ratio mixture	113
6-4 XRD pattern performed by Ying of pure pentacene and varying weight ratios of C ₆₀	114
6-5 AFM images by Ying pentacene, C ₆₀ , and pentacene:C ₆₀ of varios weight ratios.....	115
6-6 Pentacene stacking analysis for the pentacene:C ₆₀ (6:1) molar ratio	116
6-7 Pair distribution analysis of the C ₆₀ interactions in the pentacene:C ₆₀ (6:1) mixture.....	116
6-8 AFM images of pentacene:C ₆₀ weight ratios deposited at 0.6 Å/s.....	117
6-9 AFM images of pentacene:C60weight ratio at 0.6 Å/s and 6 Å/s deposition rate.	117
6-10 Random layer built C ₆₀ :Pentacene (1:1) molar ratio films.	117
6-11 Pair distribution plot of FCC ordered (6:1) and random built (1:1) molar ratio.	118
6-12 Random layer built films on low deposition	118
6-13 Pair distribution function plot between pentacene:C ₆₀ (1:1) and (1:2) molar ratios	119

Abstract of Dissertation Presented to the Graduate School
of the University of Florida in Partial Fulfillment of the
Requirements for the Degree of Doctor of Philosophy

ANALYSIS OF IRRADIATION INDUCED DEFECTS ON CARBON NANOSTRUCTURES
AND THEIR INFLUENCES ON NANOMECHANICAL AND MORPHOLOGICAL
PROPERTIES USING MOLECULAR DYNAMICS SIMULATION

By

Sharon Pregler

August 2008

Chair: Susan B. Sinnott

Major: Materials Science and Engineering

Mechanisms such as nanomechanics, changes in chemical structure, and van der Waals interactions are difficult to observe on the atomic scale by experimental methods. It is important to understand the fundamentals of these processes on a small scale to reach conclusions of results that are observed on a larger scale. Computational methods may be readily applied to investigate these mechanisms on models a few nanometers in dimension and the results can give insights to processes that occur during real time experiments. The classical molecular dynamics simulations here utilize the reactive empirical bond-order (REBO) or adaptive intermolecular REBO (AIREBO) potentials, to model short range behavior, coupled with the Lennard Jones potential (and torsion for AIREBO), to model long range interactions of carbon nanostructures and hydrocarbons.

The bond order term in the REBO/AIREBO potential allows for the realistic treatment of these materials as it correctly describes carbon (and silicon and germanium) hybridizations, and allows for bond breaking and reformation unlike basic molecular mechanics. This is a key feature for simulating irradiation and pullout mechanics on graphite and carbon nanotube and their composites.

The irradiation simulations on graphite, with the same conditions as the experimental irradiation of highly pyrolytic graphite, provide insight to the types of defects that were observed on a larger scale by Scanning Transmission Microscopy (STM) images. Experimental characterization from collaborators mapped out the surface of irradiated graphite while computational theory further described the defects and observed the evolution of the defects during the irradiation procedure.

Multi walled carbon nanotubes (MWNT) were irradiated with different particles to compare the effect that incident species have on the nanotubes' surfaces as well as the crosslink distribution of the radial cross sections. Irradiation is a common technique to modify the interfacial areas between the fiber and matrix to improve compatibility in polymer composites. Inducing crosslinks between shells of the MWNT by irradiation drastically decreased the sword in sheath deformation, where inner shells slip out with respect to outer shells, that was computationally demonstrated.

A similar procedure was also carried out on carbon nanotube – polystyrene composites. Argon irradiation was simulated for three different types of nanotubes: double-walled, single-walled, and a bundle of four single-walled nanotubes, in a polystyrene matrix. The polymer emission, depth of particle penetration, and nanotube pullouts were observed, it was shown that the presence of carbon nanotubes limited these processes.

Atomic Force Microscopy (AFM) and X-Ray Diffraction (XRD) images in conjunction with AIREBO molecular dynamics simulation trajectories of C₆₀ and pentacene films of various ratios gave theoretical and experimental insight on the molecular evolution of donor and acceptor aggregation for optimizing the design of effective organic semiconductors.

Atomic-scale simulations are thus shown to be a powerful computational tool to better understand the properties of carbon nanostructures and hydrocarbons. This dissertation illustrates how effective they are for providing insight on chemical modification, nanomechanical deformation, and equilibration mechanisms on the atomic scale.

CHAPTER 1

INTRODUCTION

General Introduction

By the mid-1980s, the study of carbon nanostructures and technological applications were thought to be well established. The carbon atom has only six electrons, and four valence electrons, and it was possible to accurately perform first principles calculations and understand carbon bonding in both molecular and condensed phases.¹ On the macroscale, the details of carbon chemistry in soot and the metastable Wurzite crystal structure phase had been examined and the phase diagram of carbon appeared to be well established.² Carbon materials were being applied to technologies such as solid and liquid lubricants, batteries, rubbers, and fillers for polymer matrix composites; thus, carbon was incorporated into applications of commercial and military interest. The rest of carbon research in the 1980s dealt with diamond-like carbon and deposition, doping, and the growth of single-crystal diamond.

Carbon Nanostructures

In the mid-1980s Smalley, Kroto, Curl, and co-workers opened doors for carbon and revealed that the element may not be as well understood as was thought.³ The group discovered fullerenes and the bulk production of these materials by Krätschmer et al.⁴ ignited a new interest in carbon nanomaterials. When Iijima discovered carbon nanotubes (CNTs) in 1991,⁵ research interest in these and related forms of carbon materials exploded, a trend that continues today.⁶ New technological applications continue to develop that include x-ray emitters for medical applications,⁷ field emitters for display technology,⁸ nanowires and junctions for nano and macroelectronics,⁹ nanofibres for composites, and scanning probe tips.¹⁰

One of the popular features of carbon research is the strong interplay between theoretical and experimental work. Theorists were the first to discover a unique relationship between the

band gap and helical structure of CNTs,¹¹ which experimentalists confirmed.¹² Another example is the reversible formation of kinks in bent CNTs that were observed in both experiments and simulations.¹³ In the field of carbon material research, theoretical calculations have thus played an important role in making predictions that lead the way for experimental work.

Graphene and Graphite

Graphene is a single sheet of carbon atoms whose arrangement is packed into a benzene-ring structure similar to a honeycomb lattice. Because of the covalent (sp^2 -hybridized) bonding of the carbon atoms, graphene is widely used to describe many carbon based materials such as, carbon nanotubes, fullerenes, and graphite, as illustrated in Figure 1-1.¹⁴ Graphene sheets have a density ~ 1 g/cc in the solid form, and exhibit a diffraction peak at 0.34 nm, which is similar to some single-walled CNT structures.¹⁵

Graphene was considered to be the first true two-dimensional crystal.¹⁶ However, an infinitely large single crystal of graphene in a 3D environment is subject to oscillations and instability over long distances.¹⁷ Researchers have observed ripples in suspended graphene and attributed them to thermal fluctuations.¹⁷⁻¹⁹ As an integral part of these three dimensional relatives, graphene was assumed to not exist in the free state and was believed to be unstable.¹⁹ Recently, a free-standing graphene was found and experiments confirmed their charge carriers to be massless Dirac Fermions.^{16,20} Fermions are particles with a half-integer spin, such as protons or electrons.²⁰ The electrical transport in graphene are goverened by Dirac's equations.²⁰

This recent discovery in graphene has granted graphite a spotlight in research for its potentials in electronic devices. Graphene has also been cut in different configurations to form graphene nanoribbons (GNRs)^{21,22} which have either metallic or semi-conducting properties. They are an attractive choice for ballistic transistors due to their high electronic quality. In

addition, graphene has high optical transparency that allows for applications in transparent conducting electrodes such as organic photovoltaic cells and organic light emitting diodes.²³

Another potential application involves using graphene for single molecule gas detection.²⁴

In this case the entire volume of graphene can interact with gas molecules, making it efficient for the detection of adsorbed molecules. Graphene powders are also used in electric batteries, where their large surface-to-volume ratio and high conductivity improve battery efficiency.^{19,25} Despite the optimism about graphene's electronic properties, graphene-based electronics are not expected to be fully developed for another decade or two.¹⁹

Bulk graphite consists of sheets of graphene arranged in a three-dimensional structure and stacked in a hexagonal closed packed manner. The sheets are bonded to one another through van der Waals interactions. Stacking sheets of graphene to form graphite drastically changes the properties of the material. Therefore, graphite has a lower conductivity between the basal planes. Although conduction is present across each individual graphene plane, the overall conductance of graphite is lower since graphite is not defect free and contains many grain boundaries. Highly ordered pyrolytic graphite has a low spread of the *c*-axis, or axis normal to the graphene plane, angle and is generally used as the most crystalline graphite available.²⁶ The thermal conductivity across the graphene plane is comparable to diamond at 1000 W/mK.²⁷ The ballistic thermal conductance of a graphene sheet is at the lower limit of ballistic thermal conductance.^{28,29}

Graphite is used for many of applications, from writing implements (pencils) to advanced aircraft materials; the field of interest for this dissertation is its use in fusion reactors.³⁰ The graphite materials in this environment are subjected to damage from energetic particles, or radiation damage. The irradiation effects in graphite are discussed in more detail in Chapter 3 and further on in this chapter.

The structure of bulk graphite complicates the computational study of it by requiring that the computational methodology adequately describes both strong covalent bonds and weak van der Waals bonds. It also complicates the experimental study of graphite, since no true large single crystals of graphite are available. Consequently, most experimental studies are carried out with highly pyrolytic graphite.

Fullerenes

Fullerenes are spherical, closed, cage-like structures of carbon that have polygon shaped interatomic arrangements of carbon atoms that are similar to those of graphite.³¹ The entire family of fullerenes range from thirty carbon atom C₃₀ to structures that contain up to about a thousand atoms.³² The buckyball, or C₆₀, is the most common fullerene. It was discovered by Kroto, Smalley, Curl and coworkers³ and was initially produced in microscopic amounts by laser vaporization techniques. Krätschmer and co-workers⁴ were able to make gram quantities of fullerenes by producing an arc of carbon between two graphite electrodes. Arc discharge,³³⁻³⁵ laser ablation,^{36,37} and oxidative combustion of benzene or acetylene³⁸ have all been used to produce mixtures of different sized fullerenes.

The buckyball has a unique shape where its faces of twelve pentagons and twenty hexagons resemble a soccer ball.³ This hollow structure results in its distinctive physical, chemical, and biological characteristics. The electrophilic properties of the buckyball have facilitated its modification through organic chemistry and synthesis routes.³¹ Atoms and molecules can attach to the C₆₀ fullerene without disrupting its spherical hollow shape. Pure C₆₀ has semiconducting properties based on electronic structure observations.³¹ However C₆₀ can be converted to a conductor or superconductor with electron donor dopant molecules or atoms, such as alkali metals.

Carbon Nanotubes

Carbon nanotubes may be thought of as graphene rolled into a cylindrical shape that can be capped at the end with a hemisphere of a fitted buckyball structure, although in some cases tapered and other non-spherical caps are formed. Since the discovery of CNTs by Iijima in 1991,⁵ there have been numerous research projects devoted to exploring their use in applications that take advantage of their unique properties. As ballistic conductors, they exhibit unique electrical properties, and are efficient heat conductors.^{28,39} Because of their high length to width ratio, they are considered to be one-dimensional structures.^{31,40} A single walled tube may be as small as 1 nm in diameter, yet be several millimeters in length.

Structure and chirality

The face of a nanotube is similar to graphene, as it has the same honeycomb carbon structure. However, the curving of the sheet alters the material's chemical reactivity and bonding nature. This increased curvature results in π -orbital mismatch,⁴¹ which makes CNTs with smaller diameters more reactive than larger-diameter CNTs.

Figure 1-2 plots the relevant vectors on graphene that define a carbon nanotube, where the point O is chosen as the origin. The CNT is formed when the head A , and tail O , of vector C_h meet and points B and B' meet, making the CNT axis parallel with vector. The vector C_h is defined as

$$C_h = na_1 + ma_2 \quad (1-1)$$

where a_1 and a_2 are the unit cell basis vectors with integers (n,m) .⁴²

The way that the graphene sheet is wrapped to form a CNT is characterized by the chiral vectors of indices (n,m) . These integers signify the number of unit vectors in two directions across the graphene face. If the indices are equal then the nanotube has an armchair arrangement.

If n or $m=0$, the carbon nanotube is termed as zig-zag. A nanotube is chiral if none of the indices are the same or are zero. Figure 1-3 illustrates the differences in the three types of carbon nanostructures.

The diameter of a carbon nanotube is given as

$$d_t = \frac{|C_h|}{\pi} = \frac{(\sqrt{3}a_{c-c})}{\pi} \sqrt{n^2 + nm + m^2} \quad (1-2)$$

where a_{c-c} is the distance between neighboring carbon atoms in the flat sheet, 14.4 nm. The chiral angle, θ , is calculated as

$$\sin \theta = \frac{\sqrt{3}m}{2\sqrt{n^2 + nm + m^2}}, \quad \cos \theta = \frac{2n + m}{2\sqrt{n^2 + nm + m^2}} \quad (1-3)$$

which in turn gives

$$\theta = \tan^{-1}\left(\frac{\sqrt{3}m}{2n + 3m}\right) \quad (1-4)$$

The lattice constant L, or vector OB , is given as

$$L^2 = a^2 s^2 \left[(n+m)^2 + \frac{1}{3}(n-m)^2 \right] = \frac{4}{3} s^2 C_h^2 \quad (1-5)$$

where s depends whether $n-m$ is a multiple of three. The lattice constant is simplified into the following expression with d as the highest common divisor, or tube diameter.

$$L = \begin{cases} \frac{\sqrt{3}C_h}{d} & \text{if } n - m \text{ is not a multiple of } 3d \\ \frac{C_h}{\sqrt{3}d} & \text{if } n - m \text{ is a multiple of } 3d \end{cases} \quad (1-6)$$

A single rolled graphene sheet as described above is termed a single walled nanotube (SWNT) with a diameter as low as 1 nm. Concentric SWNTs, or multiwalled nanotubes (MWNT), consist of two or more concentric tubes with outer diameters that range from 5 to 350

nm. MWNTs can be specifically described as

$(n_{innershell}, m_{innershell}) @ (n_{middleshell}, m_{middleshell}) @ (n_{outershell}, m_{outershell})$, where “@” implies that the nanotube rests concentrically with the other tubes.

Mechanical properties and sword-in-sheath deformation

Carbon nanotubes have a high elastic modulus, as do graphene sheets. Experimental results from Treacy et al.⁴³ and Krishnan et al.⁴⁴ determined the Young's modulus in the axial direction for isolated nanotubes to be around 1.8 TPa for MWNTs and 1.25 TPa for SWNTs. These values were obtained by measuring intrinsic thermal vibrations in a transmission electron microscope. Robertson et al.⁴⁵ explored the elastic properties of CNTs with empirical potentials and first principle simulator methods. They found that the strain energy per carbon atom relative to an unstrained graphite sheet varies as $1/R^2$ (where R is the tubule radius).

The concentric shells that form the MWNTs make them harder to bend than SWNTs. The buckling force on the MWNT is dependent on the number of inner nanotubes or shells.⁴⁶⁻⁴⁹ Simulations of MWNT buckling have shown that there is a sudden increase in strain per atom in each shell of an MWNT. Experiments concluded that MWNT buckling is intrinsic to the nanotube and not mediated by defects and that the buckles appear with a characteristic interval independent of their absolute position on the tube.⁴⁶⁻⁴⁹ Akita estimated the Youngs' moduli for MWNTs of innershells of different diameters are to be 0.77 TPa and 0.80 TPa from the Euler's buckling model.⁵⁰ The outermost shell of a MWNT is shown to absorb applied external stresses. However, the inner shells of the MWNT contribute to the stiffness of the tube in the radial direction and have an effect on buckling and bending modes.⁵¹

A direct way to measure the mechanical properties of a MWNT was developed by Yu et al. Using two AFM tips to pull the nanotube's ends, Yu found a range of modulus and strength,

from 11 to 63 GPa.⁵² Under axial stress, the inner shells slipped out from the outer shells, a failure known as “sword in sheath” deformation.⁵³

One of the questions that arise concerning innershell sliding of a MWNT is “What is the magnitude of the minimum force required to pull the innertube out?” With the case of a defect-free MWNT consisting of two shells, also known as a double walled carbon nanotube (DWNT), the sliding force depends on two contributions. The first contribution is the retracting or capillary force that is associated with how the tube responds when the inner tube is pulled. The second contribution is related to atomic friction, which is more important when sliding a finite tube with respect to a much longer tube.^{52,54,55}

Huhtala et al.⁵⁶ performed computational studies on pulling out the inner shell of a DWNT to measure the capillary force needed for pullout. During the simulation when the inner tube was far from the end of the outer tube, there were oscillations in the force which indicates that there was only shear contribution to the force since the contact area was the same. A rise in the force developed as the inner tube translated with respect to the axial direction of the outer tube. The rise in the force indicated that the capillary force has come into effect due to a decrease in the overlap area.

Composites

Advanced aerospace, aquatic, and transport applications require materials with unusual combination of properties that may not be achieved with conventional metal alloys, ceramics, or polymers. Transportation applications, for example, require parts to be lightweight, yet strong and impact resistant and not susceptible to corrosion. To engineer these characteristics, different materials that posses the features of interest are artificially formed into a composite material.

Composites are engineered materials that consist of at least two components, usually of different chemical or physical properties. Combining the two materials creates one material that

benefits from key features of its constituents. For example, a polymer mixed with carbon fibers may create a composite that has the flexibility from the polymer phase and the strength and stiffness from the carbon phase.

Most of the composites simply have only two phases; the matrix phase is the material which encases the other material or the dispersed phase. The properties of the composites are a function of the phases' properties and the amount. This relation is known as the rule of mixtures.⁵⁷ Specifically, these equations predict that the elastic modulus of the composite is defined by an upper bound between the modulus of each phase and their volume fraction:

$$E_c^{upper} = E_m V_m + E_p V_p \quad (1-7)$$

Conversely, the lower bound limit is defined as:

$$E_c^{lower} = \frac{E_m E_p}{V_m E_p + V_p E_m} \quad (1-8)$$

Advances in composite technology have stimulated interest in nanocomposites, which are defined as systems that have at least one material with one dimension of the order of 0.1-100 nm and that would produce a material of enhanced properties due to their nano-size.⁵⁸ In nanomaterials, their construction differs from macroscale processing, since building nanostructures is considered a “bottom-up” approach, or, building from atoms and molecules.⁵⁸

Polymer as the composite matrix

Polymers are structured as repeating units or monomers that are connected by covalent bonds to form giant chain-like macromolecules. Generally, polymers have a lower strength and modulus than metals and ceramics, are only useful at lower temperatures, and are electrical and thermal insulators. Polymers may be separated into thermoset or thermoplastic types.^{57,59}

Thermoset polymers are processed by a curing action where a hardening agent, thermal, irradiation, or pressure increase induces a chemical reaction that crosslinks the chains in the resin. Upon heating, thermosetting polymers decompose. Epoxy and polyester are among the common thermosetting polymer matrices. A large fraction of polymer composites use epoxy matrices since they have moisture resistance, low shrinkage on curing, and good adhesion with glass fibers.⁵⁹ The crosslinking in the matrix that contributes to a high modulus, however, also causes brittleness. In processing a fiber-epoxy composite, the fibers are incorporated into a slightly cured epoxy and held at a low temperature until it is ready to be heated processed into a composite with a fully cured and hardened epoxy.⁵⁹

Thermoplastic polymers are typically bounded by chain entanglement and have the ability to heat and cool while retaining their basic chemical structure. Examples include polyethylene and polystyrene. Thermoplastic materials are tougher than thermosetting polymers and have a failure strain ranging between 30 to 100% where thermosetting polymers fail at strain ranges of roughly 3%.⁵⁹ Generally, the fracture energy for thermoplastic polymers are an order of magnitude higher than unmodified epoxies and polyesters. The higher fracture energy of the thermoplastic polymers is contributed by the larger free volume which absorbs crack propagation energy in the material.^{57,60}

The polymer matrix used in this dissertation is polystyrene (PS), a thermoplastic and widely used commercial polymer. Polystyrene is also computationally inexpensive to model as it only consists of carbon and hydrogen bonds. Polystyrene-CNT composites have been used in aerospace applications; where the presence of CNTs on the surface layers of the polystyrene effectively protect the underlying material. The effects of CNTs in PS are discussed in detail in Chapter 6.

Carbon nanostructured based composites

Fullerenes have been incorporated in polymer matrices to form composite films. It has been found that the presence of C₆₀ lowers the thermal degradation of polystyrene which gives the material as a whole improved thermal stability.^{58,61} In addition, C₆₀ in polyethylene has increased composite hardness compared to pristine polyethylene.^{62,63} The most attractive application of C₆₀ in composites results from the high photoconductivity of the fullerene polymer mixture. Wang measured a fast and complete photo-induced discharge in C₆₀/C₇₀ doped polyvinylcarbazole (PVK) at the fullerene – polymer interface.⁶⁴ Furthermore, Sariciftci et al. observed the same behavior in C₆₀ doped poly[2-methoxy,5-(2'-ethyl-hexyloxy)-*p*-phenylene vinylene] (MEH-PPV).⁶⁵ They showed that photoinduced electrons transfer from the polymer to C₆₀s effectively, since C₆₀ has extraordinary electron acceptability. This induces anions and mobile holes in the polymer. Similar charge transfer is found in other composites of fullerenes and conjugated polymers, and the effect has potential use for photovoltaic devices.⁶⁶⁻⁶⁹

Both SWNTs and MWNTs have been used as fibers to reinforce polymer materials such as epoxies, polystyrene, nylon 12, and poly ether ether ketone. Tai et al. processed a phenolic-based nanocomposite with MWNT.⁷⁰ Gojney and coworkers incorporated only 0.1 wt% of highly dispersed DWNT in unreinforced epoxy.⁶⁰ Ogasawara used MWNTs to reinforce phenylethyl terminated polyimide through mechanical mixture and curing.⁷¹ All the composites exhibited an increase in Young's modulus, strain to failure, and strength relative to the polymers alone. Thostensen and Chou⁷² dispersed 5 wt% MWNT with a micro-scale twin screw extruder to mechanically blend and uniformly disperse the nanotubes in polystyrene. The extrusion induced a continuous ribbon of aligned nanocomposites.

Interfacial Engineering of Nanocomposites

The effectiveness of a nanocomposite depends to a large extent on the interaction between the fibers and the matrix, as well as on fiber dispersion and alignment.^{57,59} The performance of a composite depends critically on its interfacial properties.⁶¹ If the interfacial strength of the composite is too strong, the overall composite is not effective. In this case, the interface will have the highest stress to failure and thus decreasing the composites' toughness. The composite will fail at weak spots on the brittle interface, resulting in catastrophic failure. If the interface bonding between the matrix and fiber is weak, then stress will not effectively transfer to the fibers and composite failure occurs from matrix fracture.

Acquiring a uniform dispersion of the CNTs is an important factor in processing nanocomposites.⁶³ Carbon nanotubes must be separated from their bundled form and dispersed uniformly to maximize their surface area in the matrix. Exfoliation of the CNTs from their bundles increases the interfacial area and thus improves their overall effectiveness in a composite. Interfacial sliding between the CNTs occurs if the tubes are grouped in bundles or ropes, which adversely affects their load carrying capability. The alignment of the CNTs in the matrix is important to achieving anisotropic mechanical or electrical properties. They can be processed by applying shear forces or an electrical field.^{58,63,73}

The interfacial area to volume ratio is extremely high for CNT composites due to the fiber's large aspect ratio. Schadler and co-workers monitored the load transfer in a CNT-epoxy nanocomposite in tension and compression by Raman spectrometry.⁷⁴ They found that the nanocomposite's load transfer was effective during compression but was weak in tension, implying poor load transfer across the CNT-polymer interface.

Various mechanisms can be responsible for the failure of nanocomposites, including fiber pullout from the polymer matrix, fiber fracture, fiber/matrix debonding/crack bridging, and

matrix cracking.⁷⁵ Figure 1-4 is an illustration of the types of failure mechanisms at a composite's crack tip that is paired with the respective micrograph image. An ideal composite would not have too strong or too weak interfacial strength, and would therefore appropriately transfer load from the matrix to the fiber.

Additionally, deformation of a CNT-polymer composite can cause the inner shells of the nanotube to slip out of the outer shells and thus promote failure. Therefore, independent of the carbon nanotube's referenced strength, the composite strength also depends on the interaction and sliding of the inner tubes, or "sword-in-sheath" deformation.⁵⁶ If the bonding between the shells is weak, they will not contribute to the axial strength of the MWNT regardless of the number of shells present. Instead they will act like ropes of SWNTs where the load is absorbed on the SWNT perimeter.⁵⁵ However, it would be desirable for the inner shells of the MWNTs to absorb applied loads as well, especially when MWNTs are used as reinforcements in composites. The combination of these two types of bonding gives MWNTs anisotropic mechanical properties because the shells of MWNTs can readily slide and rotate with respect to one another.⁶³

When a nanocomposite without chemical modification undergoes shearing stress, the pullout forces are normally greater than the weak van der Waals interactions between the nanotube and the matrix. Therefore, the nanotube slides with respect to the matrix, or "pulls out." Frankland et al. modeled CNT pullout in polymer matrices and recorded force variations in displacement and velocities of the nanotube.^{76,77} On the nanoscale, the behavior of nanotube pullout is closely related to friction models. They have shown linear trends in the nanotube's velocity to force relationship and estimated an effective viscosity coefficient for interfacial sliding at the interface. The average shear stress for the nanotube's sliding is described as

$$\langle \tau_{rz} \rangle_{pull} = \tau_0 + \mu_{eff} \frac{\partial \langle V_z \rangle}{\partial r} \quad (1-9)$$

where τ_0 is the initial threshold pullout stress, μ_{eff} is the effective viscosity for the nanotube sliding in polymer, and $\frac{\partial\langle V_z \rangle}{\partial r}$ is an estimate of the strain rate, $\dot{\gamma}$, with V_z as the average nanotube velocity for distance r .⁷⁷

The walls of a carbon nanotube are chemically stable because of the aromatic nature of the bonding. Therefore the interface between the walls in a MWNT, and between the outershell and most polymer matrices rely on van der Waal interactions, which may not provide a sufficient load transfer. Unlike conventional carbon fibers, the nanotube length is much shorter than the polymer chains which also lead to weaker interfacial bonding. Due to the lack of load transfer between the matrix and the fiber, pristine carbon nanotubes in a polymer matrix slip out of the polymer during deformation resulting in failure of the composite.⁷⁸ This type of failure is also seen in MWNTs where innershells slip out from the outershells.

Therefore one of the challenges inherent to incorporating inert carbon nanotubes into a composite is engineering the strength of the interaction between the nanotube walls and the surrounding polymer matrix.⁶³ Efforts have been made to chemically modify CNTs to improve the load transfer across the fiber/polymer interface.^{54,79,80} If the nanotube is chemically functionalized, it may attach to the surrounding polymer matrix and would allow for better load transfer during deformation. An optimal level of covalent bonding, as opposed to van der Waals interactions, between the nanotubes and the polymer improved the shear yield strength of the overall composite. Covalent bonds on the nanotube walls weaken their modulus,⁸¹ although a slight modification has been shown to effectively reduce pullout forces while maintaining CNT structure, as discussed in Chapter 4.

The caps of the CNT are more reactive than the walls because they are under higher levels of strain as a result of their high degree of curvature.⁸² It has been shown experimentally that an

acidic solution removes the capped ends of a CNT so that the new ends react with functional groups such as carboxylic acids (-COOH groups) or hydroxylic acids (-OH groups). Successful replacements of carbon atoms by functional groups or fluorine have also been performed. These groups have the potential to induce further chemistry in a matrix and improve the interfacial load transfer by reducing slippage of the CNT with respect to the matrix. This method of functionalization only improves interfacial interaction at the tip of the tube. Interfacial properties are more effective with functionalization along the full length of the fiber.

As previously mentioned, functionalization methods have been performed on the carbon nanotubes to increase the attraction between the fiber and matrix. It has also decreased delaminating and pullout failure. One of the major approaches involves irradiating the materials with ions or electrons. Their effects on carbon structures and nanocomposites are discussed in the next section.

Irradiation Effects in Carbon Systems and Composites

Irradiation particle effects in solids have been of interest in research since the 1950s. The early studies primarily focused on metals, semiconductors, and insulators to determine the materials' resistance in a radiation heavy environment. With the newly discovered allotropes of carbon, fullerenes and carbon nanotubes, irradiation on graphitic structures has arisen.

A highly energetic particle has several primary mechanisms when it impacts its target substrate atom. In ballistic conductors studied under the computational methods discussed in this dissertation, the mechanisms of interest include, bond breakage or crosslinking, atom interstitials and displacements, sputtering of atoms and polyatomic products from the surface. Other effects include electronic excitation or ionization of atoms and plasmons, phonon generation, and emissions of photons and/or Auger electrons.^{83,84}

Graphite

Graphite is an unusual material due to its anisotropy in the lattice. It can be considered as a two-dimensional metal being electrically conductive across the basal plane, or along the graphene sheets. The bulk graphite relies on van der Waal forces to hold the graphene sheets in its hexagonal lattice. Electronic excitations from irradiated particles are quenched by the conduction electrons therefore negating the effects of this irradiation mechanism. Knock-on atom displacement is the primary irradiation mechanism in graphite due to its open structure in the normal direction, or *c*-axis.^{83,85-88}

The irradiation effect in graphite has been studied extensively for its use in fission and fusion reactors. The anisotropic nature in graphite results in irradiation mechanisms that are distinct from metals or ceramic materials. This is due, in part, to the fact that displacing an atom along the *c*-axis requires less energy than is required to displace an atom along and within the basal plane because of the open channels between the planes.⁸³

Studies have shown that radiation in graphite has induced defect agglomerates and a rupture in the basal planes due to atoms ejecting from the respective graphene sheet. The aggregation and vacancies combine and form dislocation loops between the graphene sheets, illustrated in Figure 1-5. Once the loop is formed it is stable at high temperatures up to 1000°C.⁸³

One of the unfavorable effects of irradiation on graphite is the dimensional change in the *c*-axis. The agglomerates from Figure 1-5 push the graphene sheets apart and swell the *c*-lattice spacing. The swelling grows when atoms are emitted by knock on displacement and diffuse to the agglomeration site, leading to a formation of new lattice planes. The vacancies in the basal planes also cause shrinkage at that site.⁸³

Consequently, there is a wide range in the reported data for the atom displacement threshold, T_d , simply because of discrepancy in graphite samples between researchers. Iwata and

Nihira found the T_d value to be 24 eV along the basal plane and 42 eV along the c -axis.^{86,89}

These findings agree with the results of Ohr et al., who also found T_d of 24 eV⁹⁰ within the basal plane, and Montet et al., who found T_d of 31-33 eV within the basal plane and 60 eV along the c -axis.⁹¹ Recent T_d reports by Banhart et al. include values between 15-20 eV for the c -axis value.⁸³ Specific defects and their respective activation energies are reviewed in Chapter 3.

Fullerenes and Carbon Onions

Ionization is the dominant factor with high irradiation of fullerenes. The fragmentation of the fullerene leads to smaller fullerenes, for example $C_{60}^+ \rightarrow C_{26}^{2+}$.⁹² Irradiation energies that are large enough to break the fullerene's bond energy are 7.4 eV.³¹ A series of fullerenes under irradiation have been seen to fuse and lead to larger, yet irregular, fullerenes.^{93,94} When the fullerenes are encased in a SWNT to produce a structure known as a peapod, the system has been shown to transform into a MWNT under electron irradiation.⁹⁵⁻⁹⁸ The displacement energy of a carbon atom from a fullerene is slightly lower than for graphite since the knocked out atom has ample space to move away from the cage structure and no recombination can occur. Fullerenes have also been known to disintegrate under irradiation, by Coulomb explosion and knock-on atom displacement.^{99,100}

Fullerenes can also be formed by irradiation of graphitic nanostructures. Structures of different cage sizes, C_{32} , C_{60} , and C_{240} , can be formed on a graphite surface this way. The formation occurs during an unwinding and curling of a graphene sheet from the graphite surface, until the sheet is closed.⁹³

Carbon onions or a series of concentric fullerenes are also formed by irradiation of amorphous carbon; the entropy of the entire system decreases as the ordering increases. Entropy is exported through the irradiation process since a small fraction of energy entering the system is

stored in bonding or defects, thus following non-equilibrium principles.⁸³ The curling of the graphene sheets under irradiation influences the environment until the favorable structure of a sphere is obtained, and stable under irradiation. The irradiation temperature is relatively high enough so that *in situ* annealing prevents the formation of agglomerates; however, graphene curling also occurs at high temperatures.^{83,93} The formation is governed partially by geometric structuring as a Stone-Wales transformation which ensures the onion's spherical shape.¹⁰¹

Irradiating carbon onions has been shown to nucleate diamond structures. Under irradiation the shells of the onion undergo compression toward the core which leads to diamond nucleation. Ion irradiation is more effective than electron irradiation since it has a cascading effect from incident particles having a much larger mass transfer than electrons, creating up to 600 displacements by one knocked out atom. The transformation is facilitated by the high pressure in the onion core and the sharp curvature of the inner shells. Once the diamond structure is nucleated, it grows outward and consumes the shells of the carbon onion with continuing irradiation.^{83,93}

Carbon Nanotubes

Irradiating carbon nanostructures chemically modifies the properties of the tubes whether it is used in composite applications or nanoelectronics. Recent studies have shown that crosslinks and functionalization can be induced through electron or ion irradiation. Carbon nanotubes with several shells can also be used as a protection mask from ion irradiation. The mechanisms for irradiation damage in CNTs are very similar to graphite due to the same carbon hybridizations and open structures. Banhart et al. found the threshold energy to be similar to graphite at $T_d \approx$ 15-20 eV for multi-shell tubes.¹⁰²

However, the curvature of the carbon nanotubes is the cause of the differences between graphite and CNT irradiation. Tubes of smaller diameters are under more strain than tubes of larger diameters, thus their bonds are more likely to break under particles of the same incident energy.⁴¹

The collision of energetic particles on single-walled carbon nanotubes (SWNTs) results in a carbon atom knocked out leaving one or more vacancies in the tube wall's graphite lattice. If the primary knock-on atom (PKA) has enough energy, it can leave the tube to displace other atoms. If the impact energy is low, and the incident particles are chemically reactive, they can chemically attach to one or more carbon atoms in the CNT wall, functionalizing the wall and changing the character of the involved carbon atoms from sp^2 to sp^3 hybridization, and acting as interstitials. The incident particles and sputtered carbon atoms that result may also functionalize neighboring nanotubes.

Early experiments found that CNTs develop diameter shrinkage and neck-like features under electron irradiation. This phenomenon occurs when irradiation induces vacancies on the walls of the CNTs. These vacancies are unstable and the CNT reconstructs itself to compensate for the atom loss, which results in a reduced diameter size. However, in most cases the nanotube experienced the most damage in the area beneath and normal to the direction of the beam rather than a uniform damage along the axial direction of the tube.^{83,84,103}

Other defects that occur during irradiation include non hexagonal faces, amorphous complexes, and the Stone-Wales (SW) defects on the carbon nanotube wall.¹⁰¹ These CNT defects are created only if the energy of the incident particle is strong enough to displace atoms in the tube wall. The minimum energy required to produce a Frenkel defect without recombining (threshold energy) on graphite is 20-30 eV.⁸⁴ Because of their open structure, carbon nanotubes

respond differently than most other solids; the displaced atom from the nanotube structure can travel far from its original position, unlike most other solid materials.

These vacancies from irradiation induce coalescence of SWNT with a zipper like motion where the atoms reorganized with adjacent tubes. This method is used in welding carbon nanotubes together under an electron beam.¹⁰⁴⁻¹⁰⁷ Generally, MWNTs are more stable than SWNTs during irradiation since the vacancies can easily recombine with an underlying shell in the MWNT. In some ways, irradiating MWNTs is similar to the carbon onion. When an atom is knocked from the outer shell of a MWNT, it can affect the atoms of the underling shells and may either form a covalent bond or crosslink the shells, or knock out another atom for a cascading effect. Crosslinks between the shells of a MWNT is a common defect observed in irradiation, as well as a tool that is used to decrease sword-in-sheath deformation.¹⁰⁸ Therefore, the advantages of incorporating covalent bonds between the shells without sacrificing too much of the MWNT structure is of concern. However, researchers have found that the buckling wavelength of MWNTs does not change appreciably when the tube is axially deformed or bent.⁴⁹ The effects on irradiating MWNTs and sword in sheath deformation are discussed in detail in Chapter 4.

Composites

Irradiation and ion bombardment of polymer based composites have three major effects: electronic excitations and ionization events, doping or implantation, and atomic collisions.^{83,84} Electronic excitations occur at all energies of ion irradiation which may result in bond breaking and reformation, luminescence, radiation emission, and electron-hole generation. In the doping or implantation processes, the material's composition changes with the introduction of new ions. The atomic collision mechanism, or primary knock on of atoms, is a direct momentum transfer of energy from the incident particle to the substrate.⁸³

Energetic particles that bombard a polymer composite induce several effects even when only considering the atomic collision mechanism. Particles that have enough energy may break the bonds in the polymer matrix and emit smaller products and fragments from the surface, creating an etching effect. The presence of carbon nanotubes in the polymer matrix has been found to limit the effects of etching, as the carbon nanotube effectively absorbs the particles' energy without deteriorating.^{79,109}

Light ion bombardment can also create crosslinking between polymer chains, or between polymer chains and the carbon nanotube fibers.^{79,109} This method of modification has been shown to reduce sliding between the fiber interfaces and improving the interfacial interactions.⁵⁶ This novel approach to *in situ* chemical modification of the composite avoids deterioration of CNTs by acidic approaches to functionalization. Low energy irradiation has been found to keep CNTs intact.⁸¹

Atomic irradiation of CNTs or composites to slightly change the chemical structure are common methods to improve the interfacial load transfer.^{54,79,108} Inducing crosslinks between the shells of a MWNT or between the outer shell of a CNT and the matrix has been shown to restrict sword-in-sheath deformation. However, excessive irradiation creates defects on the nanotubes which have a negative effect on the mechanical properties. It has been found that covalent bonds from chemical attachments on a SWNT have decreased the buckling force by about 15%.⁸¹ This indicates that a functionalized tube is expected to deform easier than an unfunctionalized carbon nanotube. Still, the degradation from light irradiation is generally small, and the overall benefits from an improved fiber-matrix interface are greater. The effects of irradiating CNT composites are further discussed in Chapter 5.

Photovoltaic Applications of Fullerenes and Hydrocarbons

The previous sections described carbon nanostructures for mechanical applications. This section summarizes organic electronic materials that utilize carbon nanomaterials such as the C₆₀ fullerene and pentacene hydrocarbons.

Organic semiconductors have attracted interest in research due to their lightweight, low material cost, processing ease, and flexibility as compared to their inorganic counterparts.¹¹⁰⁻¹¹² Some of these applications include photovoltaic cells, organic light emitting devices for display and lighting technology, photodetectors, and thin film transistors.¹¹³

An efficient organic photovoltaic cell requires good transport of donor and acceptor molecules, or heterogeneous junction. Figure 1-6 shows a schematic of the energy level between the donor and acceptor molecules and illustrates the charge transfer process.¹¹⁴ The dissociation of excitons leads to holes in the highest occupied orbital (HOMO) in the donor material and electrons in the lowest unoccupied molecular orbital (LUMO).¹¹⁵ The LUMO has the highest electron affinity and the HOMO has the smaller ionization potential. The electrons are transported through the donor molecules to the anode which creates the photocurrent. The external quantum efficiency can be described as:

$$\eta_{EQE} = \eta_A \times \eta_{ED} \times \eta_{CT} \times \eta_{CC} = \eta_A \times \eta_{IQE} \quad (1-10)$$

where η_A is the absorption efficiency, η_{ED} is the exciton diffusion efficiency, $\eta_{CT} \approx 1$ is the charge transfer efficiency at the interface, η_{CC} is the charge collection efficiency, η_{IQE} is the internal quantum efficiency.¹¹⁵

The efficiency of a heterogeneous junction is dependent on the exciton diffusion, which can be short in films of molecules which are bound together with van der Waal forces.¹¹¹ Blends of conjugated molecules have been used to form bulk mixtures to increase the exciton efficiency,

η_{ED} . The molecules distributed in the bulk structure resulted in spatially distributed donor-acceptor (DA) molecules, reducing their distances and effectively improving exciton travel and raising η_{ED} . However a high density of interfacial area will reduce charge carrier mobility, lowering η_{CC} the charge collection efficiency, as conducting holes will be confined in donor materials.^{110,111}

Therefore, it is considered that microstructure/nanostructure and degree of phase separation are critical factors in the photovoltaic properties of an organic DA mixture. Large domains of donor and acceptor materials will restrict the passageway of excitons, thus reducing η_{ED} , as a high degree of phase separation will percolate charge conduction and raise η_{CC} . Computational efforts have been performed to better understand the nanostructure of these materials.

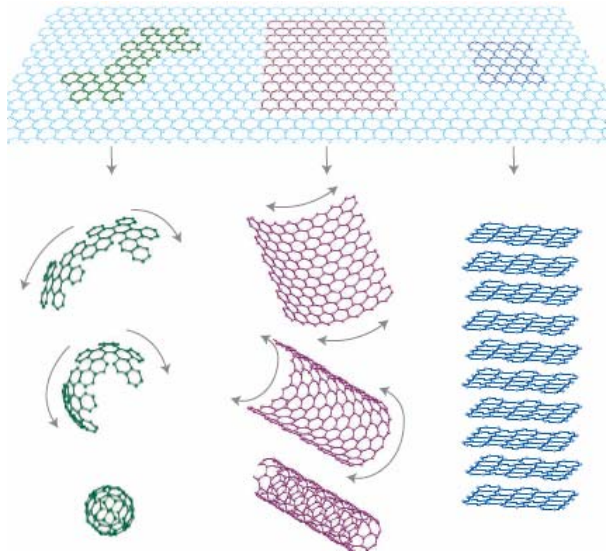


Figure 1-1. A single sheet of graphene being transformed into a fullerene, carbon nanotube, and graphite.¹⁹

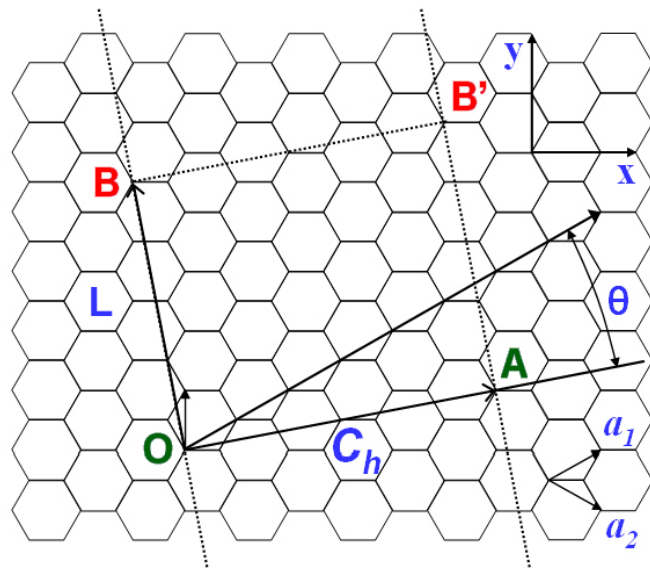


Figure 1-2. Graphene plane with directional vectors mapping the carbon nanotube.^{42,116}

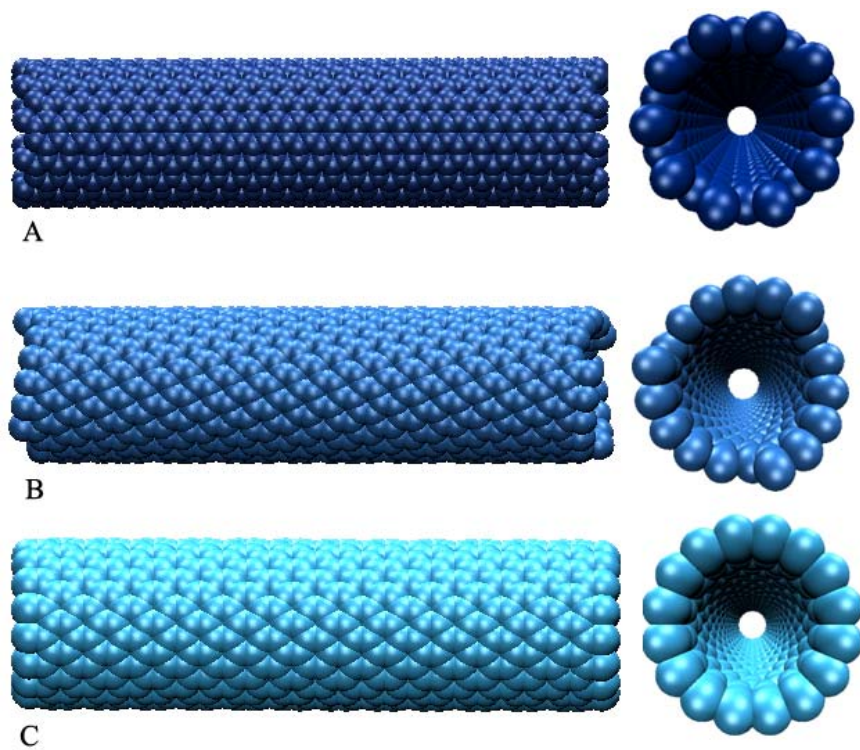


Figure 1-3. Radial and axial views of A) armchair carbon nanotubes where $n=m$, B) chiral nanotubes where $n \neq m$, and C) zig zag nanotube where either n or $m = 0$.

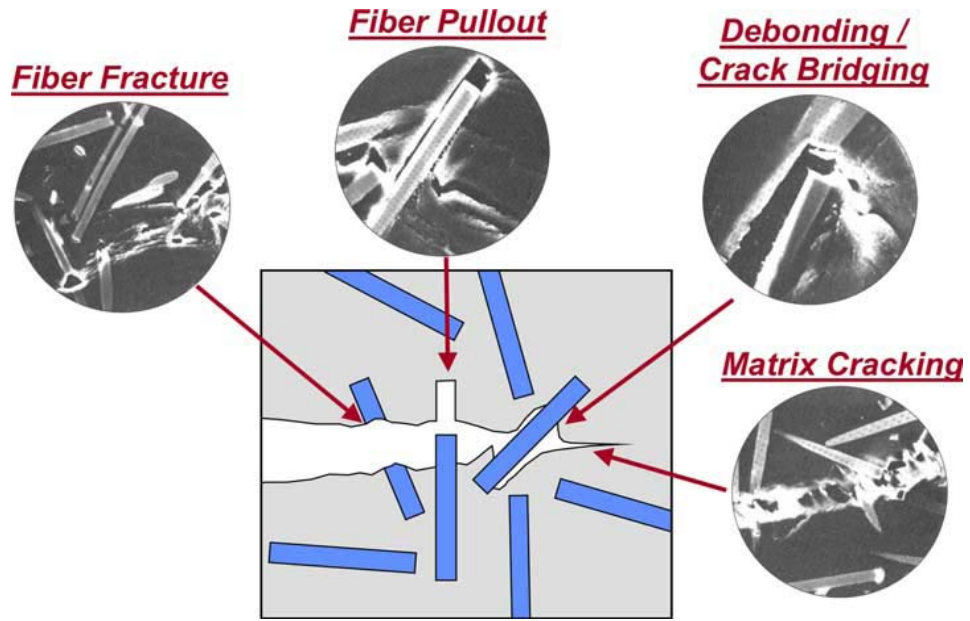


Figure 1-4. The mechanisms and respective micrograph images of different fracture mechanisms in a nanotube polymer composite.^{58,117}

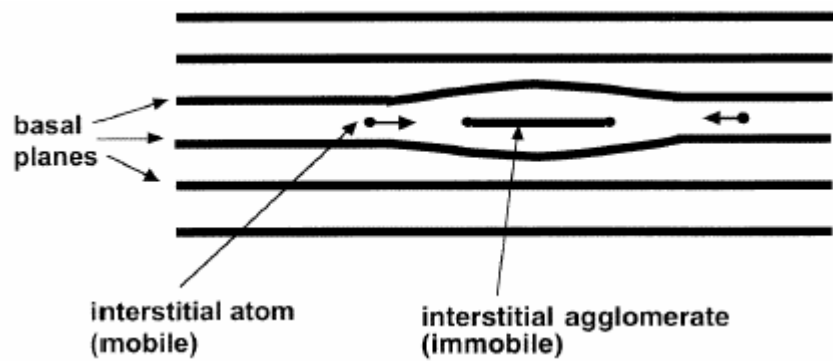


Figure 1-5. Aggregation of self interstitials in graphite as a result of irradiation. A dislocation loop has occurred between two graphene sheets.⁸³

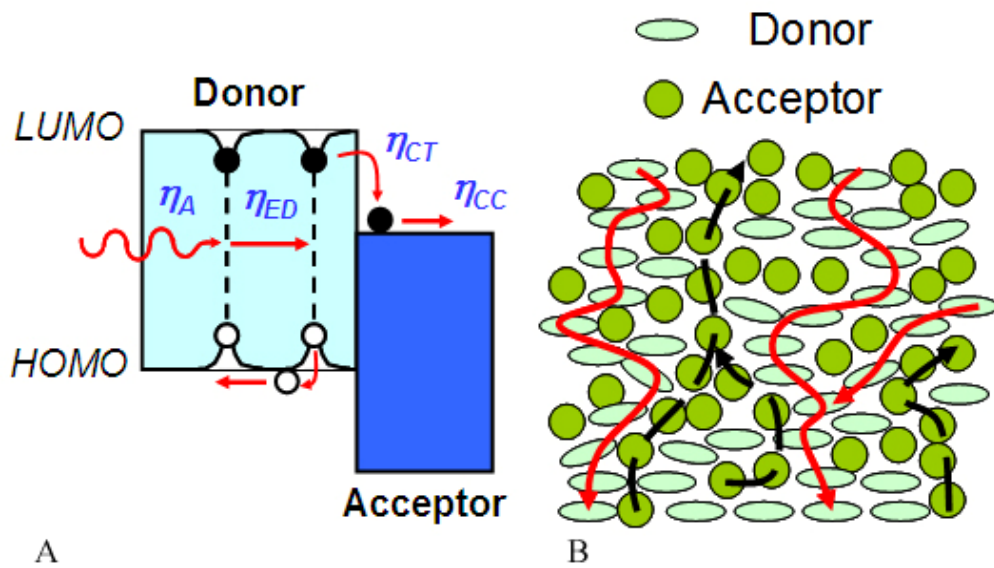


Figure 1-6. Organic photovoltaic semiconductors. A) Schematic of the energy levels between donor and acceptor molecules illustrating the photovoltaic process. B) Continuous path of charge conduction through a desired degree of phase separation.¹¹⁸

CHAPTER 2

COMPUTATIONAL METHODS

Classical Molecular Dynamics

Molecular dynamics (MD) simulation is a technique that computes the equilibrium and transport properties of classical many-body systems. Here, *classical* is termed as nuclear motion of particles that obey the laws of classical mechanics.

The structure of MD simulations is similar to real experiments in many respects. Generally, to start an experiment, one starts and prepares the material to study, then connects it to a measuring instrument such as a thermometer or manometer, and measures the materials' property changes over a given interval of time. MD simulations follow the same basic approach. In preparing the sample, a model system of N particles is initialized. The MD process then uses Newton's equations of motion for the particles until their properties no longer change with time, also known as equilibrating the system. After equilibration, an analysis of atom displacements, bond lengths, crystal structure, or other properties of interest are calculated.

Therefore, MD simulations can be simplified into five general steps. First, parameters are provided as input, which include initial temperature, number of particles, density, time step, etc. Second, the system is initialized where starting positions and velocities are assigned to all particles in the system. Third, the forces acting on all the particles in the system are calculated. In our systems we consider many-body interactions, and must consider the force on particle i due to its nearest neighbors. There are efficient techniques we use to calculate the short-range and long range interatomic interactions.^{119,120} These techniques are discussed in some detail later in this chapter. Fourth, molecular dynamics simulations integrate Newton's equations of motion to calculate the motion of atoms with time and the results are observed from several output files describing properties of interest such as atom placement and bond length.

The motions of the particles are expressed by the second law of motion where the force vector F_i of atom i is equal to the product of the atom's mass, m_i , and acceleration a_i

$$F_i = m_i a_i \quad (2-1)$$

Two more models are needed to relate the position of the particles and time. The first model is based on the conservation of energy that relates the forces between atoms i and j to the potential energy:

$$F_{ij} = -\left(\frac{\partial PE}{\partial r_{ij}} \right) \quad (2-2)$$

where r_{ij} is the distance between atoms i and j . The second model uses a numerical analysis algorithm of the acceleration to describe locations with respect to time with the following derivative:

$$a = \frac{dv}{dt} = \frac{d}{dt} \left(\frac{dr_{ij}}{dt} \right) \quad (2-3)$$

where v is the velocity with respect to dt which is on the order of picoseconds. The integration of the Newtonian equations of motion yield the positions of the particles, and in turn their velocities, accelerations, and higher derivatives of position with respect to time. The integration is handled with a predictor corrector algorithm which is explained in detail later in this chapter. These factors are the basis to describe the fundamental properties of a given system. After this central loop completes for the desired length of time, the average output of the measured quantities are analyzed, completing the simulation.^{119,120}

Reactive Bond Order Potential

Abell derived a general chemical binding energy term which is the starting point for the Reactive Bond Order (REBO) potential. Tersoff developed Abell's work to simulate the

potential energy and interatomic forces of the covalent bonds in C and Si systems.¹²¹ Brenner modified the Tersoff potential to improve its performance for carbon and hydrocarbon systems by introducing an analytical bond order form.¹²² Brenner then further improved the potential in the second generation REBO by refining its analytical terms and increasing the fitting database used to obtain the potential's parameters, thus creating a better description for conjugation, bond angles, bond lengths, torsion, coordination, and other effects for carbon and hydrocarbon systems.¹²³ Variations of the second-generation REBO potential were then optimized for hydrocarbon and fluorocarbon systems,¹²⁴ and for C-O and O-H covalent bonding.¹²⁵

The first generation hydrocarbon expression used Morse-type terms including pairwise and many body terms. This potential can describe carbon bonding in hydrocarbon molecules and chains, graphite, and diamond. It is, however, too restrictive to simultaneously fit equilibrium distances, energy, and force constraints for these bonds. Furthermore, modeling energetic atom collisions is limited as terms approach finite values. Abell showed that the chemical binding energy is simply a sum over nearest neighbors, as

$$E_b^{REBO} = \sum_i \sum_{j(>i)} [V^R(r_{ij}) - b_{ij} V^A(r_{ij})]. \quad (2-4)$$

The functions $V_R(r)$ and $V_A(r)$ are pair additive interactions for core-core repulsive and attractive interactions, respectively, with r_{ij} as the distance between atoms i and j . Abell argued that the coordination number N controls the bond order in regular structures and used a Bethe lattice¹²⁶ to describe the relation as,

$$b \propto (N)^{-\frac{1}{2}} \quad (2-5)$$

In equations 2-5 and 2-6, Morse-type pair interactions describe energy versus volume relations that are similar to a general binding energy curve. A universal binding curve, however,

is too restrictive to simultaneously describe energy and equilibrium distances in carbon and Group IV elements. This form also has another disadvantage in which the repulsive and attractive terms approach to a finite value as distances between atoms decrease. This flaw restricts the ability to model bond breaking and reforming. Tersoff built on Abell's work and refined the bond order and analytical terms from equation 2-5, thus developing the second generation REBO.

The analytical form from equation 2-5 is refined below for the 2nd generation REBO.

$$V_R(r_{ij}) = f_c(r_{ij}) \left[1 + \frac{Q}{r_{ij}} \right] \cdot A \cdot e^{-\alpha \cdot r_{ij}} \quad (2-6)$$

$$V_A(r_{ij}) = f_c(r_{ij}) \sum_{n=1,3} B_n \cdot e^{-\beta \cdot r_{ij}} \quad (2-7)$$

where A, B, Q, α , and β are two-body parameters that depend on the types of atoms that are interacting. The $f_c(r)$ function from equation 2-7 and 2-8 restricts covalent interactions to only nearest neighbor atoms where $D_{ij}^{\max} - D_{ij}^{\min}$ defines the distance over where the function varies from one to zero.

$$f_c(r_{ij}) = \begin{cases} 1 & \text{if } r_{ij} < D_{ij}^{\min} \\ \frac{1 + \cos \left[\frac{r_{ij} - D_{ij}^{\min}}{D_{ij}^{\max} - D_{ij}^{\min}} \right]}{2} & \text{if } D_{ij}^{\min} \leq r_{ij} \leq D_{ij}^{\max} \\ 0 & \text{if } r_{ij} > D_{ij}^{\max} \end{cases} \quad (2-8)$$

The bond order term b_{ij} is known as the many-body empirical bond-order term and is a key variable in the REBO potential. There are numerous types of chemical effects that are fitted for this term, including bond angles, torsion angles, coordination number, and conjugation

effects. This term allows atoms to inhibit these effects according to their environment, whether if its bond breaking, bond formation, or changes in atomic hybridizations. This feature allows a more realistic simulation for a relatively large number of carbon atoms while utilizing the computational efficiency of an empirical method. The bond order b_{ij} is described below:

$$b_{ij} = \frac{1}{2} [b_{ij}^{\sigma-\pi} + b_{ji}^{\sigma-\pi}] + b_{ij}^{\pi} \quad (2-9)$$

Values for $b_{ij}^{\sigma-\pi}$ and $b_{ji}^{\sigma-\pi}$ are determined by local coordination and bond angles for atoms i and j and are defined as

$$b_{ij}^{\sigma-\pi} = \left[1 + \sum_{k(\neq i,j)} f_{ik}^c(r_{ik}) G(\cos(\Theta_{jik})) e^{\lambda_{ijk}} + P_{ij}(N_i^C, N_i^H) \right]^{-\frac{1}{2}} \quad (2-10)$$

The $f_c(r)$ term ensures that the interactions are limited to the nearest neighbors. The term $G(\cos(\Theta_{jik}))$ regulates the dependency on the nearest neighbor according to the bond angle between atoms i and j and atoms i and k , which is determined by the angles in a diamond lattice (109.47°) and graphite plane (120°). The term λ_{ijk} is a fitting parameter that describes three-body transition states around H atoms. The function P_{ij} is a bicubic spline and a correction term to the bond order based on the environment of the atom neighbor i . The terms N_i^C and N_i^H are the number of carbon and hydrogen atoms respectively of atom i . These are defined by

$$N_i^C = \sum_{k(\neq i,j)}^{carbon} f_{ik}^c(r_{ik}) \quad (2-11)$$

and

$$N_i^H = \sum_{l(\neq i,j)}^{hydrogen} f_{il}^c(r_{il}) \quad (2-12)$$

The neighboring atom is assigned a value of 0 to 1 for distances between atoms i and k which guarantees that the overall function, E_b , is continuous during bond breaking and reforming.

The term b_j^π is defined as

$$b_{ij}^\pi = \Pi_{ij}^{RC} + \Pi_{ij}^{DH} \quad (2-13)$$

where Π_{ij}^{RC} the radical term and Π_{ij}^{DH} the dihedral term. The value of Π_{ij}^{RC} determines whether the atoms i and j have a radical component or are part of a conjugated system. This term defines a key difference between the first and second generation REBO, since it accounts for the conjugation of carbon atoms and correctly describes radical structures such as vacancy formation in diamond and accounts for non-local conjugation effects as seen in graphite and benzene. The term Π_{ij}^{RC} is expressed as

$$\Pi_{ij}^{RC} = F_{ij}(N_i^t, N_j^t, N_{ij}^{conj}) \quad (2-14)$$

The two spline functions are coupled and yield N_i^t or N_j^t . N_{ij}^{conj} is defined as

$$N_{ij}^{conj} = 1 + \left[\sum_{k(\neq i, j)}^{carbon} f_{ik}^c(r_{ik}) F(X_{ik}) \right]^2 + \left[\sum_{l(\neq i, j)}^{carbon} f_{jl}^c(r_{jl}) F(X_{jl}) \right]^2 \quad (2-15)$$

where

$$F(x_{ik}) = \begin{cases} 1 & x_{ik} < 2 \\ \frac{[1 + \cos(2\pi(x_{ik} - 2))]}{2} & 2 < x_{ik} < 3 \\ 0 & x_{ik} > 3 \end{cases} \quad (2-16)$$

and

$$x_{ik} = N_k^t - f_{ik}^c(r_{ik}) \quad (2-17)$$

The term Π_{ij}^{DH} defines the dihedral angle for the carbon-carbon bonds as

$$\Pi_{ij}^{DH} = T_{ij}(N_i^t, N_j^t, N_{ij}^{conj}) \left[\sum_{k(\neq i,j)} \sum_{l(\neq i,j)} (1 - \cos^2(\Theta_{ijkl})) f_{ik}^c(r_{ik}) f_{jl}^c(r_{jl}) \right] \quad (2-18)$$

where Θ_{ijkl} is the torsional angle between atoms i, j, k , and l and the function $T_{ij}(N_i^t, N_j^t, N_{ij}^{conj})$ is a tricubic spline interpolation.

As a result, the binding energies and bond length databases were expanded and carbon bonds have the ability to break and rebond or create new bonds while appropriately describing atomic hybridizations.¹²³ This version of the REBO potential produces an improved fit for the elastic properties in diamond and graphite and is better able to describe defect energies. In addition, hydrocarbon molecules are more accurately modeled with a better description for bond length, energies, and force constants.

The REBO potential is exclusively short ranged, which only describes the interaction of two atoms within a less than covalent-bonding cutoff of r_{ij}^{\max} , 2.0 Å, for C-C bonds. Long range potentials such as the Lennard Jones potential have been splined to REBO to account for interactions greater than 2.0 Å. The REBO potential also lacks a model to describe torsional interactions for hindered rotation about single bonds which is fixed in the AIREBO potential.

Lennard Jones Potential

The Lennard Jones potential is smoothly connected to the REBO potential by a cubic spline to account for long range, or van der Waal interactions between particles. The research here uses the 12-6 form

$$V_{LJ}(r_{ij}) = 4\epsilon \left[\left(\frac{\sigma}{r_{ij}} \right)^{12} - \left(\frac{\sigma}{r_{ij}} \right)^6 \right] \quad (2-19)$$

where $V_{LJ}(r_{ij})$ is the cohesive energy for the distance r between atoms i and j . The Lennard-Jones parameters ε , denoting the depth of the potential well, and σ , finite distance where the interparticle potential is zero, are for particular types of atoms. The $\left(\frac{1}{r}\right)^{12}$ term describes the repulsion interaction of the atoms based on the Pauli principle, when electron clouds overlap, the energy of the system increases abruptly. The $\left(\frac{1}{r}\right)^6$ term describes the long range attractive interactions derived from dispersion or dipole-dipole interactions.

The parameters ε and σ between two different types of atoms are calculated with the Lorentz-Berelot rule which is described below

$$\sigma_{AB} = \frac{(\sigma_{AA} + \sigma_{BB})}{2} \quad (2-20)$$

$$\varepsilon_{AB} = \sqrt{\varepsilon_{AA} \cdot \varepsilon_{BB}} \quad (2-21)$$

The REBO potential is exclusively short ranged, which only describes the interaction of two atoms within a less than covalent-bonding cutoff 2.0 Å for C-C bonds. The potential has been splined with the 12-6 Lennard Jones potential to account for van der Waals interactions however, this results in large barriers for radical species and small barriers for saturated compounds.

Adaptive Intermolecular Reactive Bond Order Potential

A new potential, based on the original REBO, introduced non-bonded interactions through an adaptive treatment of intermolecular interactions, or AIREBO.¹²⁷

Chemical characteristics of the system are considered to preserve the reactive character of the potential, and whether to include the LJ interaction. The decision is made adaptively under three conditions: (i) the distance between the atom pair of interest, (ii) strength of their bonding

interaction, and (iii) the network of bonds connecting the pair. The complete expression for the LJ interaction is as follows

$$E_{ij}^{LJ} = S(t_r(r_{ij}))S(t_b(b_{ij}^*))C_{ij}V_{ij}^{LJ}(r_{ij}) + [1 - S(t_r(r_{ij}))]C_{ij}V_{ij}^{LJ}(r_{ij}) \quad (2-22)$$

where the universal switching function is represented by

$$S(t) = \Theta(-t) + \Theta(t)\Theta(1-t)[1 - t^2(3 - 2t)] \quad (2-23)$$

The switching function is unity for $t < 0$ and zero for $t > 1$ and uses a cubic spline to switch smoothly at an intermediate t . The scaling function between the distances of the atom pair that affects the strength of the LJ interaction in $S(t_r(r_{ij}))$ as

$$t_r(r_{ij}) = \frac{r_{ij} - r_{ij}^{LJ \min}}{r_{ij}^{LJ \max} - r_{ij}^{LJ \min}} \quad (2-24)$$

The bonding switch that can affect the LJ interaction in $S(t_b(b_{ij}^*))$ converts the REBO b_{ij} to a range to fit with the cubic spline is

$$t_b(b_{ij}) = \frac{b - b_{ij}^{\min}}{b_{ij}^{\max} - b_{ij}^{\min}} \quad (2-25)$$

The AIREBO potential allows nonbonded interactions to switch smoothly as bonding configurations change.

A new term in the AIREBO potential is a torsional model that is dependent on dihedral angles. The generic form for torsion is a cosine power series in

$$V = \frac{1}{2} \sum_{k=1}^3 V_k [1 - (-1)^k \cos(k\omega)] \quad (2-26)$$

where the coefficients V_k must depend on changes to the energy barriers, preferably from the local coordination environment which is accomplished through a single minimum in

$$V^{tors}(\omega) = \varepsilon \left[\frac{256}{405} \cos^{10}\left(\frac{\omega}{2}\right) - \frac{1}{10} \right]. \quad (2-27)$$

The torsional potential for all dihedral angles with a proportion to contributing bond weights in the system is implemented into the AIREBO model

$$E^{tors} = \frac{1}{2} \sum_i \sum_{j \neq i} \sum_{k \neq i, j \neq i, j \neq k} w_{ij}(r_{ij}) w_{jk}(r_{jk}) w_{kl}(r_{kl}) \times V^{tors}(w_{ijkl}) \quad (2-28)$$

thus updating the entire system energy to

$$E = E^{REBO} + E^{LJ} + E^{tors} \quad (2-29)$$

The introduction of the LJ interactions predicts the diamond's crystal lattice 0.004 Å shorter than REBO and experiment and also slightly changes the elastic constants. However this contraction is balanced by an predicted increase in the tensile covalent bonding force parameters which lead to a slightly stiffer force constant and larger elastic constants. The properties in graphite display the same trend in diamond, in this case shortened bonds by 0.02 Å. The LJ potential correctly parameterizes the graphite layer distance at $r_l = 3.354$ Å. This parameter is absent in REBO, therefore modeling sheets of graphene require AIREBO. Since REBO has fewer calculations than AIREBO, the calculation time is significantly (approximately five times) shorter than AIREBO for the same set of atoms.

Periodic Boundary Conditions

The sample size studied with MD normally models systems sizes on the order of nanometers for efficient calculations. If the properties of a small liquid drop or nanocrystal are of interest, then the simulation conditions would be straightforward. The cohesive forces between particles in the system may be strong enough to hold the system together during the course of the simulation. However, these conditions are not satisfactory when simulating a bulk material.^{119,120}

Implementing periodic boundary conditions is a technique to replicate a unit cell to effectively form a bulk lattice. During the simulation as particles move in their original box, the clone particles in the periodic image move the same way. If a particle leaves its primary boundary, it will reappear on the opposite face of the box, thus the number of particles in the entire system is conserved. It is often thought that the two-dimension primary box is rolled into a three-dimension doughnut.

The number of particles in a cubic cell, N , are surrounded by an infinite array of duplicated cells as shown in Figure 2-1. Each cell has particle i , with its replicated particles at the same relative position in their neighboring cells. All the minimum images of particle i are found within the potential cut-off r_c . The contributions to the force are calculated with equation 2-2. The potential cut-off must be less than cell size L to prevent over counting of particles. For a system of Lennard-Jones particles, it is possible to perform simulations without the particles interacting with its duplicates in the primary box of side $L \approx 6\sigma$.

Predictor Corrector Algorithm

The predictor-corrector algorithm is a finite difference approach to solve ordinary differential equations, such as the Newtonian equations of motions used in MD.¹¹⁹ There are four basic steps for the general scheme of step-wise MD simulations with a predictor-corrector algorithm. First positions, velocities, and accelerations are predicted at a time $t + \delta t$. Second, the forces and accelerations are evaluated from the new positions. Next the predicted positions, velocities and accelerations are corrected with new accelerations. Lastly, calculations are performed on the variables of interest, such as energy, and the time averages accumulate prior to repeat the steps.

Given the particle information at time t , position, velocity, and other dynamic data, new dynamic information at a later time $t + \delta t$ can be solved by Taylor expansion. This dissertation used the third-order Nordsieck-Gear predictor-corrector algorithm.¹¹⁹

$$\begin{aligned}\vec{r}^p(t + \delta t) &= \vec{r}(t) + \delta t \vec{v}(t) + \frac{1}{2} \delta t^2 \vec{a}(t) + \frac{1}{6} \delta t^3 \vec{b}(t) \\ \vec{v}^p(t + \delta t) &= \vec{v}(t) + \delta t \vec{a}(t) + \frac{1}{2} \delta t^2 \vec{b}(t) \\ \vec{a}^p(t + \delta t) &= \vec{a}(t) + \delta t \vec{b}(t) \\ \vec{b}^p(t + \delta t) &= \vec{b}(t)\end{aligned}\tag{2-30}$$

where \vec{r} and \vec{v} are the atoms' position and velocity; \vec{a} is the acceleration, and \vec{b} is the third time derivative of the position. The superscript p denotes the terms 'predicted' version.

The interatomic forces at the predicted positions for time $t + \delta t$ are calculated with a potential energy gradient, in this case REBO, AIREBO, LJ, etc. since the predicted values are not based on physics. Without incorporating the equations of motion, the predictor equations will not generate accurate trajectories as time progresses. With the correction step, the new positions at time $t + \delta t$ may be calculated with the correct acceleration $\vec{a}^c(t + \delta t)$. The estimated size of error in the prediction step is as follows:

$$\Delta \vec{a}(t + \delta t) = \vec{a}^c(t + \delta t) - \vec{a}^p(t + \delta t)\tag{2-31}$$

Working backwards from the corrected step, the new position and derivates can be recalculated to reflect better approximations of the true values:

$$\begin{aligned}\vec{r}^c(t + \delta t) &= \vec{r}^p(t + \delta t) + c_0 \Delta \vec{a}(t + \delta t) \\ \vec{v}^c(t + \delta t) &= \vec{v}^p(t + \delta t) + c_1 \Delta \vec{a}(t + \delta t) \\ \vec{a}^c(t + \delta t) &= \vec{a}^p(t + \delta t) + c_2 \Delta \vec{a}(t + \delta t)\end{aligned}$$

$$\vec{b}^c(t + \delta t) = \vec{b}^p(t + \delta t) + c_3 \Delta \vec{a}(t + \delta t) \quad (2-32)$$

The new ‘correct’ accelerations are calculated from \vec{r}^c and compared to the current value of \vec{a}^c to further refine the atoms’ positions and velocities, etc. The coefficients for the third order are $c_0 = 1/6$, $c_1 = 5/6$, $c_2 = 1$, and $c_3 = 1/3$. The predictor gives an initial guess, but the successive corrector iterations allow the solution to converge into an accurate answer. Greater accuracy can be achieved by higher orders of derivatives or using a smaller time step, δt ; however this drastically increases the computation time.

Langevin Thermostats

Thermostats are used in MD simulations to ensure that the system is at a constant temperature.¹¹⁹ They are intended to match experimental conditions either by fixing particle number, volume or pressure, and temperature. They are also used to study a thermal dependent process, and mitigate excess heat avoiding energy drift from accumulation of numerical errors.

The temperature is defined as an average internal kinetic energy $\langle K \rangle$ of all particles N , thus allowing to these thermostat atoms to fix the temperature T at a set point

$$\langle K \rangle = \left\langle \sum_{i=1}^N \frac{1}{2} m v_i^2 \right\rangle = \frac{3}{2} k_B T \quad (2-33)$$

where m is the mass of the particle, v is velocity, and k_B is the Boltzmann’s constant.

The Langevin thermostat is developed from the generalized Brownian motion of theory, instead of the Newtonian equations.¹²⁸ A frictional force which is proportioned to the velocity is added to the conservative force to adjust the kinetic energy of the particles to set the system’s temperature to the desired value. The Langevin thermostat equation is

$$m \vec{a}(t) = f(t) - \zeta v(t) + f'(t) \quad (2-34)$$

where $f(t)$ is the conservative force at a time t . The term $-\zeta v(t)$ is the frictional drag between the particles, decreasing the temperature as ζ is a fixed positive constant for friction. The friction constant is based in terms of the Debye frequency ω_D which is related to the Debye temperature T_D .

$$\zeta = \frac{1}{6} \pi \omega_D \quad (2-35)$$

$$\omega_D = (k_B T_D) / \hbar \quad (2-36)$$

where \hbar is Plank's constant.

The random force $f'(t)$ is determined from a Gaussian distribution in order to add kinetic energy to the particle varying by the temperature and the simulation time step, Δt . The Gaussian distribution is expressed as

$$\sigma^2 = \frac{2m\zeta k_B T}{\Delta t} \quad (2-37)$$

The random force $f'(t)$ is balanced by the frictional force; therefore, the system's temperature is maintained at the set value.

Primary Knock on Atoms

As indicated earlier in this chapter, the REBO potential does not include electronic excitations. However, it is assumed that the ballistic electrical and thermal conductive nature in highly conducting carbon materials dissipate this effect, making it negligible. Some materials such as carbon nanotubes and graphene have generally high thermal and electrical conductivities, thus lessening the importance of ionization and electronic excitation mechanisms. Thermostat atoms maintain the system's desired temperature and absorb phonons generated which prevent the system from heating.

When carbon nanostructures are the target, the most important mechanism involved is primary knock-on atom (PKA).⁸³ Atoms are displaced when a highly energetic electron or ion collide with the nuclei. The geometry of the mechanism is described below in Figure 2-2. The angular dependence of Θ , the angle between the direction of motion of the incident particle and the direction of the scattered particle, is defined by T as:

$$T(\Theta) = T_{\max} \cos^2 \Theta \quad (2-38)$$

T_{\max} is defined as the maximum transferred energy from a head on collision, or when Θ equals 0. The probability of an incident particle skewing from the define head on collisions is far greater, so T_{\max} is defined using momentum conservation laws for the maximum energy transfer of the particle.

$$T_{\max} = \frac{2ME(E + 2mc^2)}{(m + M)^2 c^2 + 2ME} \quad (2-39)$$

Where M and T is the mass and transferred energy of the target particle, m and E are the mass and initial energy of the incident particle, respectively. For electron irradiation, the incident mass of the particle is relatively far less than the target mass ($m_e \ll M$) and initial energy ($E \ll Mc^2$) thus reducing equation 2-39 to:

$$T_{\max} = \frac{2E(E + 2m_e c^2)}{Mc^2} \quad (2-40)$$

The minimum energy that is required to displace an atom to form a vacancy – interstitial pair is known as the threshold energy, T_d . The corresponding threshold energy of the incident particle E_d , has dependency on the atom's crystal lattice. In the open structure of carbon nanotubes and graphite, the atoms can be displaced more easily if the incident particle hits the atom at an angle normal to the basal plane.

When an atom is knocked from its initial position with enough energy to exceed the surface binding energy of the specimen, the atom becomes ejected or sputtered. The atoms on the surface are less tightly bound than the atoms underneath, so the required energy for atoms to leave the surface simply needs to overcome the sublimation energy. Ion irradiation produces more sputtering than electron irradiation due the higher energy transfer of ions vs. electrons.

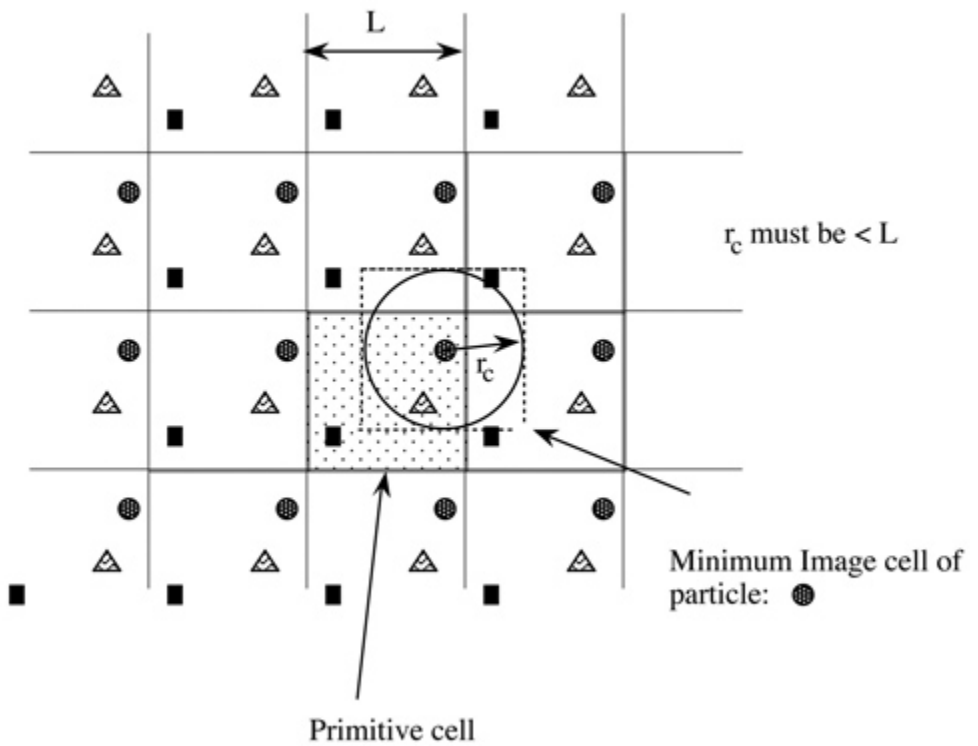


Figure 2-1. Orthogonal periodic boundary conditions.¹²⁹

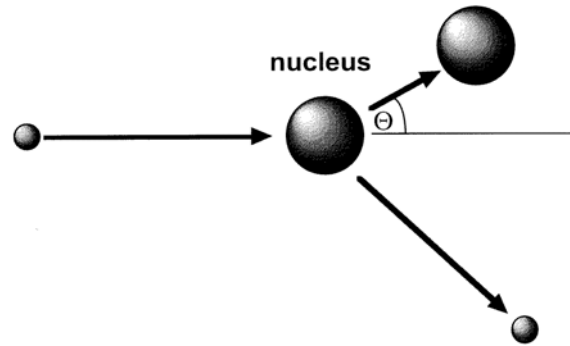


Figure 2-2. Energetic particle bombarding the incident nucleus, describing primary knock on behavior in irriadiation.⁸³

CHAPTER 3

ARGON IRRADIATION ON GRAPHITE AND EVOLUTION OF DEFECTS

Radiation damage in graphite is of particular interest because of its widespread occurrence in nuclear reactors. In the Windscale reactor fire in 1957, defects in graphite led to a spontaneous release of energy.³⁰ This motivated the study of defects in graphite to address safety in reactors that are being decommissioned. There has also been an effort to determine and engineer favorable structures in nanostructured carbon materials and assess their effects on defect formation under electron or ion-beam irradiation.^{86,88,130}

The most common processes that occur in graphite materials as a result of irradiation are bond-breaking, cross-linking, displacement of target atoms, electronic excitation, phonon generation, and sputtering of surface atoms. Graphitic structures, including carbon nanotubes, are essentially immune to electronic excitation because sp^2 -hybridized carbon materials are ballistic conductors with high thermal and electrical conductivity. However, unlike metals, graphite and carbon nanotubes have more occurrences of atom displacement because of their open structures.

This chapter discusses defect formation and growth in graphite under ionic irradiation using a combination of experimental and computational methods. This project was in collaboration with the Kondow group at the Cluster Research Laboratory in the Toyota Technological Institute: The East Tokyo Laboratory carried out the reported experimental work.¹³¹ In both cases, graphite was irradiated with Ar atoms with incident energies of 50 eV. The system was replicated by MD simulation and the nature of the defects was analyzed.

System Setup

Experiment

Our collaborators setup their apparatus similar to those discussed in reference.^{131,132} Argon ions, Ar^+ , were produced by discharging argon gas (NIPPON SANSO, 99.9995% pure) by a

magnetron. The argon ions selected in a quadruple mass-filter were allowed to collide onto a graphite (0001) surface at a collision energy of 50 ± 5 eV. The Ar^+ beam of 20 pA was irradiated on the graphite surface in a circular area of 7 mm^2 for ~ 3000 s. The Ar^+ beam is deflected by 7 mm off the original beam axis by a parallel-plate deflector placed in front of the surface in order to prevent neutral species in the beam from admitting onto the surface. The ion beam deviated by approximately 10° from the surface normal direction. The surface was maintained at a temperature of 300 K under an ambient pressure of 5×10^{-8} Pa. STM images of the graphite surface were measured with an STM probe made of Pt-Ir alloy at a surface temperature of 300 K and at a pressure less than 1×10^{-8} Pa. The graphite surface was prepared by cleaving highly oriented pyrolytic graphite (ZY-A grade, Union Carbide Inc.) in air, and no further cleaning was carried out since this method of cleaving gives an atomically flat surface. An STM image of the graphite (0001) surface prior to Ar^+ irradiation (not shown) indicated that it was free of defects.

Computation

The graphite system used in the simulations consists of 5,040 total atoms of four sheets that are 64 nm by 520 nm. A Langevin thermostat is applied to a 50 nm perimeter of atoms in each graphite sheet to maintain the system temperature at 300 K. These thermostat atoms also mimic thermal dissipation properties of the much larger experimental graphite sheets. Ninety atoms of 50 eV/atom were irradiated over a $186,200 \text{ nm}^2$ area around the center of the graphite system. After each Ar impact, the structure is allowed to equilibrate before the next deposition event. Although, the computational fluence was 5.37 Ar/nm^2 which was much higher than the experimental flux of 0.05 Ar/nm^2 , however, the information gained from the simulations can still be used to interpret the experimental findings to determine defect evolution formation and

thresholds of damage. After 90 Ar atoms had bombarded the graphite, the system was allowed to relax at 300 K for 20 more ps until the total energy of the system oscillates around a constant value with time.

Irradiation Results

Figure 3-1 is an STM image of a graphite surface after Ar^+ irradiation performed by our collaborators. The bright spots are an indication of defects formed by impinging Ar^+ and denote a variation in the electronic structures which is caused by structural change from the pristine structure. Therefore, the bright areas are points of where defects are present. Our collaborators plotted a distribution of the defects' apparent diameters in Figure 3-2. The mean value and the standard deviation of the distribution are 1.59 nm and 0.42 nm, respectively. A relatively large standard deviation of the apparent diameter distribution leads us to conclude that several different types of defects are created on the graphite surface although all the defects are observed similarly as small hills.

The random dispersion of the bright spots in Figure 3-1 implies that the damage is independent of a single ion impact on a larger scale. The computational snapshots Figure 3-3 and Figure 3-4 demonstrate the evolution of damage under continuous Ar irradiation. The simulations predict that defects prefer to grow on existing defect sites rather than pristine sites. Under continuous irradiation, defects may be forced to repair back to the pristine structure or develop into a cluster of several defects. For example, a cross-link shown in Figure 3-3 after 30 deposited Ar is no longer present as more Ar atoms are deposited. Instead, the site has transformed into a larger clump which consists of combinations of cross-links, polygons, and other defects.

During the early stage of irradiation, up to 30 deposited Ar particles, a few sites containing defects start to appear. No defects are formed after 10 Ar atoms are deposited but two Frenkel

defects appear after 20. The top view in Figure 3-4 suggests that Ar atoms impact the defective area and break bonds between the two carbon atoms which rehybridize with the graphite layer underneath. As a result, a cross-link is formed, shown in Figure 3-3's cross-section view.

The defects grow during the middle stage of irradiation, between 40 and 60 deposited Ar atoms have impacted the surface. Various types of defects start to appear: adatom-vacancy pairs, sp^3 - sp^3 cross-links, and another Frenkel defect at the site of the first two. As the interlayer defects increase surface defects grow as well. Carbon atoms transform out of their hexagon arrangement and merge to form larger polygon defects. During this middle stage, defects attempt to find a stable configuration while being bombarded by incoming Ar atoms. This stage suggests processes where defects are growing and undamaged areas are struggling to remain pristine.

Fewer events occur in the last stage of irradiation when compared to the middle stage. Many interlayer defects find a stable and tougher configuration and are not affected by incoming Ar atoms. However, there is still surface reconstruction in response to the existing damage and ongoing irradiation. Carbon atoms swell away from the graphite plane to compensate from the damage. A perfect Stone-Wales 5-7-7-5 pair appears after 60 Ar, but is lost by the end of the irradiation event.

A top view of the graphite after irradiation and equilibration is shown in Figure 3-5. The cross-links are shown in purple, and carbon atoms that have curved above their original graphene plane are shown in green. The cross-links cause a retraction toward the defect, thus the surrounding atoms curve up to balance. This finding is consistent with the results of Koike and Pedraza¹³⁰ and Muto and Tanabe,¹³³ who observe swelling in the direction perpendicular to the graphite basal plane and contractions within the basal plane during electron irradiation. The predicted defects shown in Figure 3-5 are comparable to those in Figure 3-1. Mochiji et al.

observed variances in height on graphite surfaces that underwent high-energy bombardment on the order of 2-15 keV¹³⁴ which is apparent from the STM and computation results. Furthermore, the clusters of defects measured in Figure 3.5 fit with the measurements of the histogram in Figure 3.2 which suggests that damaged areas indicated in the STM images are clumped, rather than individual, defects.

Defect Analysis

The hybridizations of the carbon atoms were tracked over the course of the irradiation. Atoms may cross-link and become sp^3 -hybridized or an atom may partially dislodge itself, “punch out,” of the graphene plane to become sp -hybridized. Certain types of cross-links have one or two atoms that are sp^3 -hybridized and some have an interstitial atom connecting the planes that is sp - or sp^2 -hybridized. Figure 3-6 indicates the percentage of sp^3 - and sp -hybridized carbons during the irradiation. The percentage increase of both types of hybridizations indicates that the defects containing these hybridizations are also increased.

Figure 3-6 shows the three stages that the graphite experienced during irradiation based on the sp^3 hybridization results. In the first stage where up to 30 Ar atoms have been deposited, carbon atoms start to dislodge from the graphene plane and contribute to a rise in the sp curve. Here, the atoms try to heal the damaged structure by either forming cross-links or reforming back into its original position. The sp^3 slope starts to broaden in the middle stage, between 40 and 60 deposited Ar, but the sp curve spikes. Carbon atoms that are sp -hybridized are abundant in polygon type surface defects, so an increase in the sp -curve indicates that these types of defects are growing. The final stage shows a slight decrease in the sp^3 curve and a sharp rise in the sp curve. This trend is a sign that the structure is swelling around the sites of cross-links to compensate for the retraction.

Defect formation energies were calculated in the AIREBO and compared to DFT results to understand the defect events that occurred in the simulation. The defect formation energies (E_f) are calculated from the total energies of the supercell with a defect as follows:

$$E_f = E_d - E_{bulk} - n\mu. \quad (3-1)$$

Where, E_d is the total energy of the defect containing system and E_{bulk} is the total energy of the pristine graphite sample, n is the number of carbon atoms that are added and μ is the chemical potential of carbon. For most defects, no carbons are added, therefore the equation is simplified.

There are several types of defects that appeared in the simulations and the defect formation energies are listed in Table 1. There are two possible sites for vacancies on the graphite plane. Vacancy A defined as a missing atom that normally sits directly above an atom from the layer beneath, while vacancy B sits directly above the center of a hexagon in the under-layer. The AIREBO potential predicts the E_f of vacancies A and B to be 7.4 eV and 7.8 eV, respectively. These values are slightly lower than density functional theory (DFT) calculations,¹³⁵ however the trends and orders of magnitude are consistent. During relaxation, carbon atoms around the vacancy site move away from the defect, which agrees with the DFT predictions, but disagrees with tight-binding results¹³⁶ which predicted neighboring atoms move closer to the vacancy site by 0.03 nm.

Adatoms are a defect common in graphite and have several different types. The two considered here are an “on top” adatom and “punch” defect. The “on top” adatoms consists of a single carbon atom that sits directly above a carbon atom in the basal plane and bonds only to this atom, which strains the surrounding carbon atoms in the graphene plane. E_f for this defect is 6.8 eV. The “punch” defect is a combination of an adatom and vacancy. This type of defect is

also very common in irradiated graphite. It occurs when an atom receives enough kinetic energy to be displaced from the basal plane, but does not have enough energy to fully leave the lattice. Instead, two of the three bonds are broken such that the carbon atom dangles between two graphite layers. This defect generally does not remain in this configuration and can revert back to its initial location, or bond with a carbon atom in the underlying graphene layer, creating a Frenkel defect.

There are three different types of cross-links that have occurred during the irradiation: Frenkel defect, sp^3 - sp^3 pair, and bridge or interstitial link. The IV Frenkel defect, illustrated in Figure 3-8A, is a combination of a carbon interstitial and a vacancy is formed when a carbon atom is punched out of the graphene plane and cross-linked with two carbon atoms in the layer below. The other two atoms around the vacancy site, where the carbon atom was punched from, interact through a weakly reconstructed bond. It is the most common type of cross-link to form in these simulations, despite having the highest defect formation energy. These outcomes agree with Ewels et al.,¹³⁷ who found that IV Frenkel pairs can result from irradiation. The defect energy is found to be 11.8 eV in AIREBO which is comparable to Li et al.'s value of 10.8 eV from DFT calculations.¹³⁵ The bond from the interstitial atom to the upper graphite layer is relatively short at 0.133 nm, while the other two bonds are 0.145 nm in DFT and in our simulation. The short bond is a distorted double bond which accounts for the stability of the Frenkel defect, despite its high formation energy. The complex can recombine into perfect graphite structure if the recombination barrier of 1.3 eV is overcome.¹³⁷

The sp^3 - sp^3 bond, illustrated in Figure 3-7B, is the second most predominant cross-link defect in our graphite system. It is formed when a carbon atom in one layer impacts the carbon atom in the layer beneath. This defect is also known to occur in large ion irradiation cases since

carbon atoms gain enough kinetic energy over a considerable area on the graphite plane to hybridize with a carbon underneath. However, in order for the top carbon atom to get close enough to the carbon atom below, the graphene plane must be strained in that direction, otherwise a vacancy will occur. It is more unstable than the interstitial cross-link based on the formation energies, but the orientation and incident particle during irradiation allows this type of cross-link to occur more than the interstitial type. However as mentioned previously, the Frenkel defect appeared more often in our graphite system after irradiation despite the higher defect energy formation.

A bridged shear interstitial defect, shown in Figure 3-7C, is also predicted to form and is seen less often in the simulation than the other two cross-links. Here, the graphite forms cross-links between the layers through self-interstitials. The interstitial sits in between two graphene planes and covalently bonds evenly to four carbon atoms on the top and bottom layers create a four-fold defect with bonds averaging to be about 0.151 nm long. The graphite layers shear around the site to lower their energy. In crystalline graphite, the defect may not spontaneously nucleate since it would result in undesired faults and dislocation loops over a large area.⁸⁸ However, most graphite is naturally defective so these defects are known to be attracted to existing shear sites.¹³⁸ In our case, more interstitial-type defects are apparent once the irradiation dose exceeds 50 Ar atoms.

The easiest surface defect to form is the Stone-Wales (SW) defect and is also a common defect in our system, shown in Figure 3.8.¹³⁹ We found the defect formation energy to be 4.6 eV with AIREBO which is in agreement with *ab initio* of 4.8 eV. Other values reported for a Stone Wales defect are 5.2 eV and 5.9 eV by Li et al.¹³⁵ and Jensen et al.¹⁴⁰, respectively, using DFT calculations and 6.02 eV by Zhou and Hi using Hückel calculations.¹⁴¹ The transition state

occurs when the rotation angle is 45°. The reason for the large barrier at this angle is that the carbon atoms need to rearrange themselves, which involves bond breaking. However, Li et al. found that the associated energy barrier is 4.4 eV above the SW defect level, or 9.2 eV at the top of the barrier (in DFT calculations).¹³⁵

Some of the E_f values reported in Table 1 are close to the *ab initio* values and some are not. This is because some defects, for example vacancies have been included in the fitting for the AIREBO potential. Other defects such as the adatom or Frenkel defect are not included in the potential but are still a close comparison considering that AIREBO does not account for electronic structure or spin polarity.

Conclusions

Layers of graphite were irradiated experimentally and computationally normal to the basal plane. The STM image of the graphite shows bright spots which indicate areas where Ar⁺ ions at 50 eV impinged the surface and induced defects. The simulations and experiment showed that defects occur over a broad distribution and each site contains several combinations of defects. The structure shows little damage during the first stage of irradiation, starts to grow during the second stage as well as fighting to retain its pristine structure, and in the final stage starts to rearrange itself to be stable. Analysis shows that several types of defects occur, and their defect formation energies are consistent with DFT-calculated values. Comparison of the defect patterns and sizes formed in the experimental samples are consistent with the defect complexes that are predicted to form in the simulations. Importantly, the simulations illustrate how defects accumulate under repeated Ar impacts.

Table 3-1. Defect formation energies of various defects observed in graphite after Ar irradiation calculated by AIREBO and DFT.

Individual defects	E_f (eV) from AIREBO	E_f (eV) from DFT 135
Vacancy A	7.4	7.6
Vacancy B	7.8	8.0
Adatoms	6.8	7.2
Punch	9.5	--
<i>Cross-links</i>		
sp^3 Link	7.7	--
Interstitial	7.5	7.2
Frenkel	11.8	10.8
<i>Stone-Wales</i>		
Stone-Wales	4.6	4.8
Stone-Wales Barrier	10.9	9.2
Stone-Wales Transition	5.3	4.4

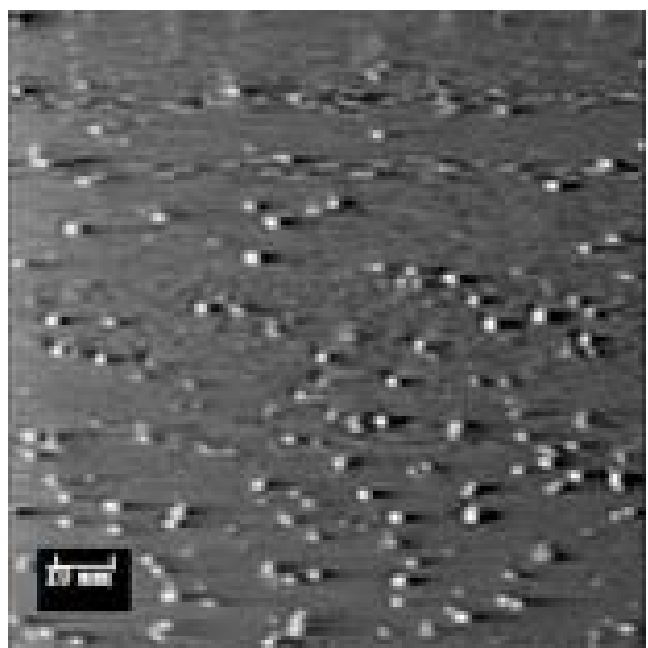


Figure 3-1. STM image of graphite surface irradiated by Ar^+ at the collision energy of 50 ± 5 eV.

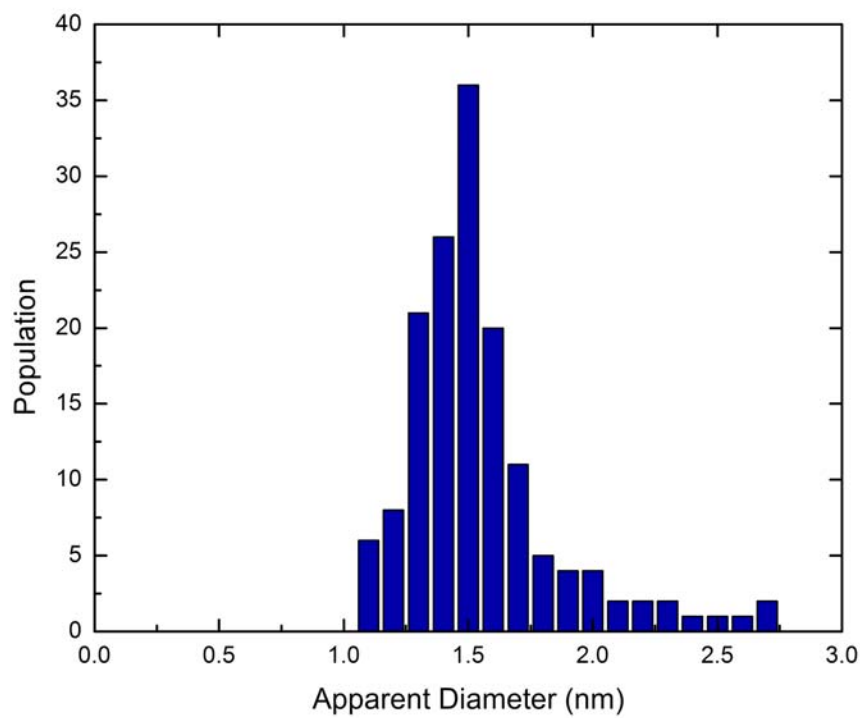


Figure 3-2. Distribution of the apparent diameter of the defects measured by STM.

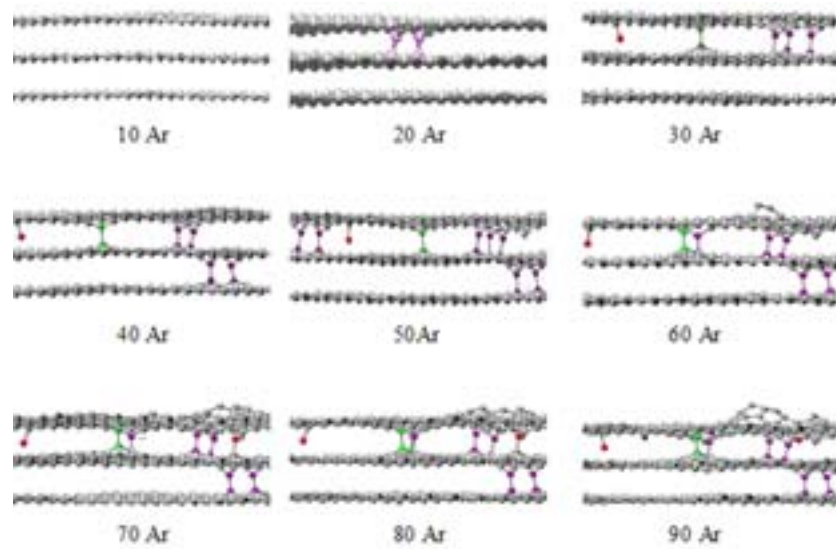


Figure 3-3. Side view of graphite during Ar irradiation. These snapshots show how cross-links and punch outs form and evolve with more Ar atoms are deposited.

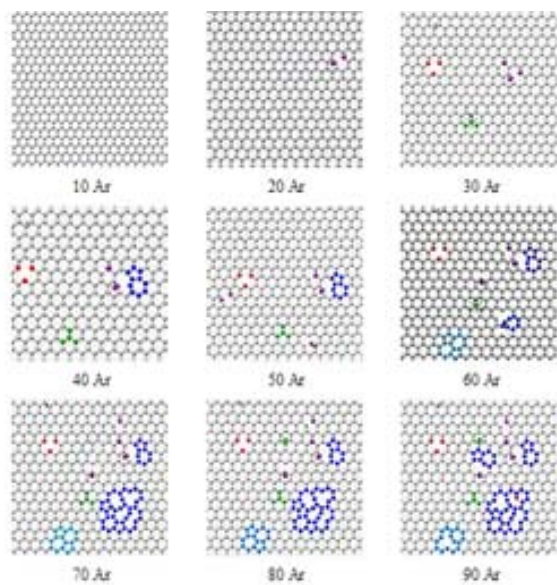


Figure 3-4. Top view of graphite during Ar irradiation. These snapshots show how the polygons/Stone-Wales and other surface defects evolve.

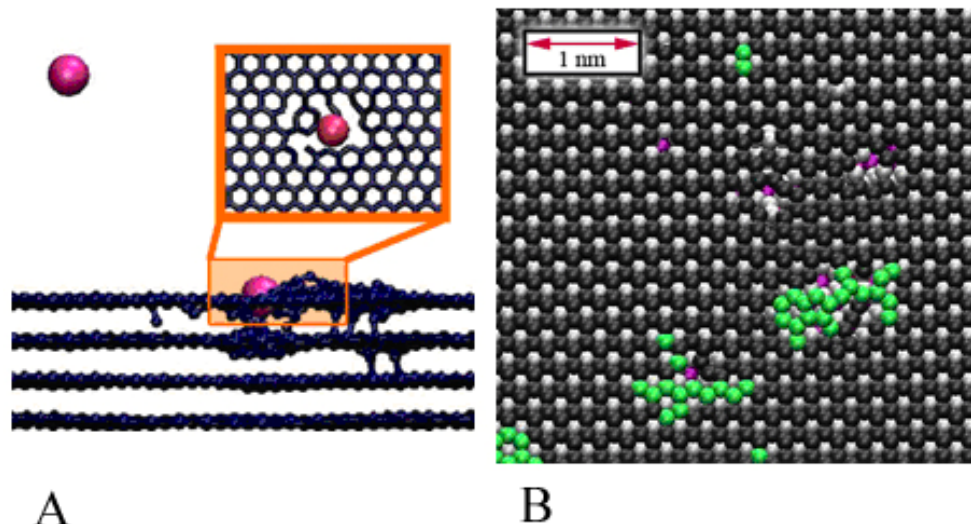


Figure 3-5. Irradiation damage in graphite. A) Side view snapshot of Ar atoms impacting the graphite surface. The inset shows a top view close-up that illustrates the additional damage that occurs in the graphite as a result of the deposition event. No Ar atoms are implanted during the simulation. B) Top view snapshots of the graphite after the deposition of 90 Ar atoms. Areas shown in green are where atoms have popped out of the basal plane of the graphene sheet. Areas shown in purple contain either Frenkel or sp^3 - sp^3 cross-links. The grey atoms in the top view are atoms in the underlying layer.

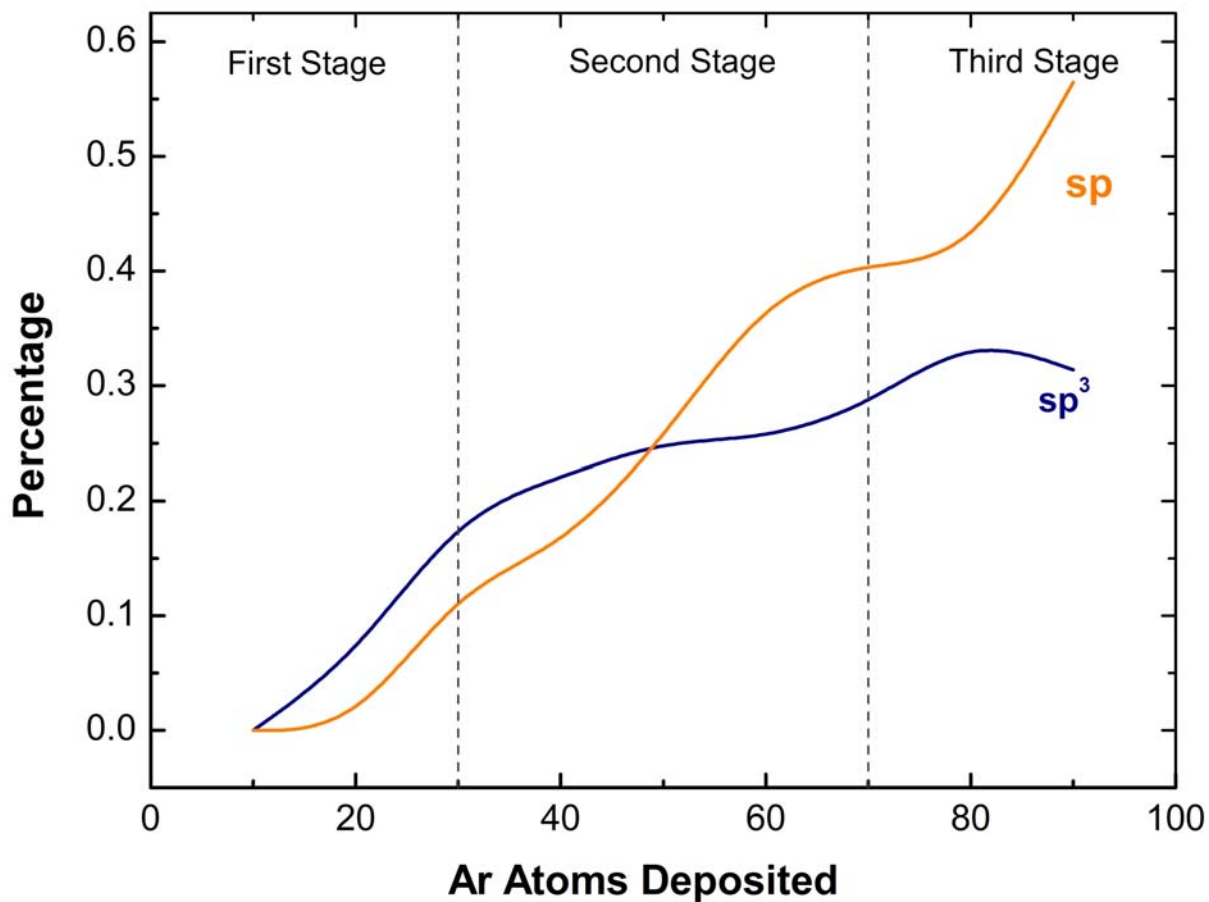


Figure 3-6. Percentage of sp^3 - and sp -hybridized carbon atoms in graphite system after 90 Ar atoms have been deposited.

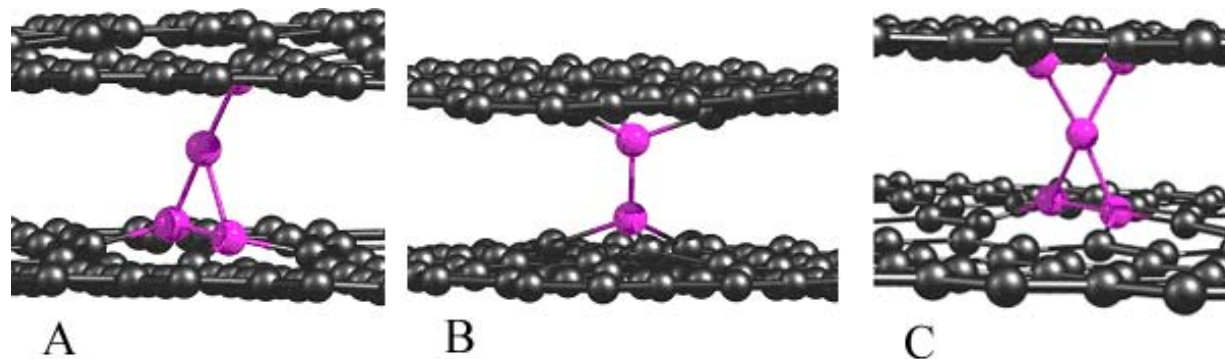


Figure 3-7. Snapshot of A) a Frenkel defect (an interstitial-vacancy pair), B) a sp^3 - sp^3 cross-link, and C) an interstitial cross-link.

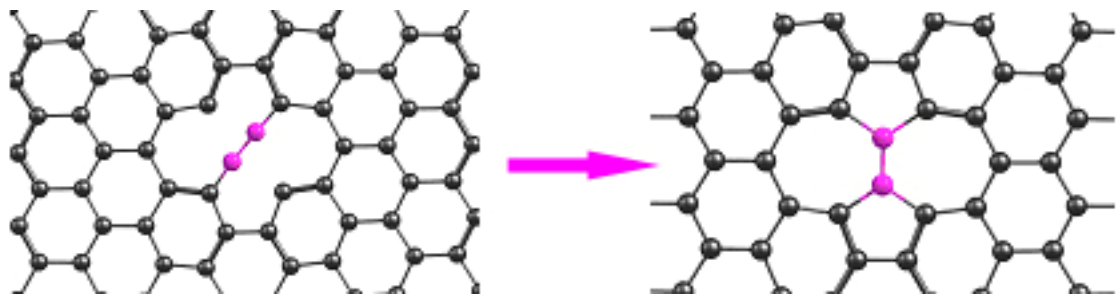


Figure 3-8. Snapshots illustrating the formation of a Stone Wales defect, where the purple atoms turn 90°. The point of highest energy occurs when the atoms are turned 45° since bonds are being broken to arrange themselves to the Stone Wales defect.

CHAPTER 4

IRRADIATION AND AXIAL PULLOUT EFFECTS ON MWNTS

Computational methods, especially molecular dynamics with REBO, have been widely used to study carbon nanotubes. The second generation REBO potential allows for bond breaking and reformation in carbon systems and can accurately model CNTs on the nanometer scale without expensive computation. Because of their small size, certain properties such as irradiation mechanics and shell sliding prove to be difficult to observe in experimental methods.⁷⁵

The previous chapter investigated defect-formation in graphite during ion-beam irradiation. Since graphite sheets and carbon nanotube walls have similar geometry, the irradiation study was branched to explore ion bombardment and defect-formation in multi walled carbon nanotubes. The resulting comparison provides information on how curvature influences the results of irradiation. In addition, nanomechanical pullout simulations were performed to analyze the extent of irradiation-induced defects on the interactions of the nanotube shells with one another.

Here, two different nanotubes were irradiated with three different methods: polyatomic ion (CF_3), single ion (Ar), and electron irradiation. After the irradiation process, the innermost shell was pulled axially with respect to the outer shell to examine the effects that different types of irradiation have on pullout forces.

System Background

Two different types of multi-walled nanotubes were used in this study, each with three concentric shells. One was an armchair MWNT that consisted of $(5,5)@(10,10)@(15,15)$. The second was a chiral MWNT that consisted of $(6,4)@(15,4)@(24,4)$. These different structures were chosen to investigate the effect of chirality between carbon nanotubes during irradiation and axial pullout. Both of the tubes were 11 nm in length, but the diameters between the inner,

middle, and outer shell are the same between the two tubes. Only the chirality or arrangement of carbon atoms is different between these systems.

The nanotubes were allowed to equilibrate at 300 K before irradiation. The irradiation area was 4.0 nm long in the axial direction and 1.6 nm long in the radial direction. A region on each end of the nanotube, 2.0 nm wide, was set as Langevin thermostat atoms to maintain the MWNT at 300 K temperature. A virtual substrate is placed beneath the nanotube during irradiation to mimic a support plate and to prevent the nanotube from deflecting.

In the case of CF_3 ion irradiation, 50 ions were placed starting at 1.0 nm above the nanotube and were spaced at 10.7 nm apart so that the MWNT is impacted every 2 ps. The incident energy was 50 eV/ion. This gave enough time for the nanotube to equilibrate after each impact, otherwise the effective result will simulate an irradiation with an extremely high flux. The same procedure was used for the Ar irradiation, 50 incident atoms at 50 eV.

The electron irradiation had a different approach than the above methods. The method used is known as the primary knock-on method, or PKA. Rather than assigning kinetic energy to an incident particle, a random carbon atom in the nanotube received a transferred kinetic energy of 10 eV which is the equivalent energy it would receive from a 50 keV electron source. Random PKAs are assigned throughout the MWNT over 3.0 nm axial length, 1.0 nm in the radial length, and 1.0 nm vertical cross-section. One PKA is assigned every ten steps for 2 ps followed by 1 ps of system relaxation. The temperature of the irradiated area rises to about 3500 K after the 2 ps collision period and cools to 1600 K after the 1 ps relaxation period that follows, which is higher than the experimental values of 1000 K. Nevertheless, these computational conditions are acceptable as they allow for reconstruction of the bonds without melting or thermal degradation.

After each set of irradiation events, the MWNT structure is cooled to 300 K prior to structural analysis.

Results

Irradiation

The molecular dynamics simulations indicate that the helical structures of MWNTs can influence the outcome after irradiation. Figure 4-1 below shows that the armchair MWNT on the left has considerably fewer defects than the chiral MWNT on the right. Figure 4-2 shows that there is slight deformation with the CF_3 ion beam irradiation.

Both the chiral and armchair have the same atomic concentration so the differences in irradiation outcome are due to the varying carbon arrangements between nanotubes. Particularly in the case of the armchair MWNT, the row of carbon atoms on the outer shell are directly above another row of carbon atoms in the underlying shells. For the chiral MWNT, the atoms follow a helical arrangement so the underlying shells may not follow the same pattern. The differences in the atom arrangements affect the crosslink concentration in the sense that the impact on the outer shell received from an incoming particle may or may not directly transfer the kinetic energy to the atoms in the underlying shell. If the atoms below are shifted or skewed, they may not receive enough kinetic energy from the upper layer to create a bond.

The simulations show that different mechanisms occur when the nanotube is irradiated with Ar as opposed to CF_3 . Ar is chemically inert so the collisions between the incident ion and the target MWNT are purely elastic. The CF_3 ions react with the MWNT surface and dissipate their kinetic energy in various physical and chemical routes, which may not always include crosslinking. Figure 4-3 summarizes the processes that occurred during the CF_3 irradiation and compares them with the processes that occurred from the Ar irradiation. There are many occurrences of dissipation with CF_3 and as a result, the incident CF_3 particle loses energy and

does not always transfer enough energy to a carbon atom on the MWNT to induce damage or crosslinks than pure knock on Ar collisions. Most of the crosslinks are formed during a pure impact or “bounce” of the Ar or CF₃ ion with the MWNT wall, but other processes that occur during CF₃ irradiation can also induce crosslinks. These processes include dissociation of the CF₃ particle into various other particles that either adhere to the MWNT surface or scatter away.

Figure 4-4 illustrates the results of an electron beam irradiation on the MWNTs. The defects and crosslinks are more radially distributed when compared to the Ar and CF₃ beam deposition. This reflects that the electron beam has the ability to affect the underlying shells and is not surface limited in the way the ions are surface limited. The results show that the armchair MWNT experiences more damage than the chiral MWNT. The extensive damage caused the MWNT to collapse, yet the chiral structure maintained its tubular shape.

The hybridization of the carbon atoms in the MWNTs following irradiation is shown in Table 4-1. These values consider the areas that were under irradiation and exclude the thermostat atoms. The analysis shows that the carbon arrangement on the MWNT, armchair or chiral, has little effect on the final distribution of carbon hybridization following irradiation. The table also indicates that the damage outcome of the MWNTs following ion-beam irradiation are not greatly different from each other despite the fact that the images shown in Figure 4-1 and Figure 4-4 appear to show significant damage. Since the sp² hybridization is close to 100% in all cases, the nanotube as a whole has little damage. However the few crosslinks induced show significant effects on pullout forces.

The snapshots of the irradiated MWNTs indicate obvious crosslinking and well as clusters of defects that may be difficult to visually organize. The hybridization analysis indicates what carbon atoms experienced sp³ hybridization, but does not necessarily give an indication whether

the atom is part of a crosslink. Atoms may be partially knocked out of the shell's pristine structure and bridge the gap between two shells resulting in a sp -hybridized state. The figures show that the electron irradiated samples have more crosslinking than the ion irradiated tubes. These differences in damage are indicative of the differences in the mechanisms on how virtual electrons and physical ions impact the MWNT. For example, an incident ion can hit more than one carbon atom and transfer its energy to two or three atoms upon impact. Consequently, the outer shell of the MWNT will recoil toward the middle shell, where two carbon atoms can get close enough to hybridize in a sp^3 crosslink. In contrast, the virtual electrons as modeled by PKA affects only one carbon atom at a time, but that carbon atom receives the full energy of an impact and has more chance to form a sp -hybridized crosslink.

Pullout

A method to explore the effectiveness of the crosslinks between the shells of the MWNT, is axially pulling the innermost shell with respect to the outermost shell, otherwise known as "sword-in-sheath" deformation. MD simulations were carried out to pull the innershell completely out of the MWNT that was hydrogen-terminated at the ends at rates of 40 m/s. The MWNT was equilibrated at 300 K and the innershell was pulled 0.05 nm and then relaxed at each step. This process was performed on the irradiated representative MWNTs as well as a pristine MWNT.

A band of 1.0 nm of atoms on the end of the innershell of the MWNT was assigned as moving atoms while the rest of the atoms on the innershell were kept as active. On the outermost shell, a 2.0 nm band of atoms on the opposite end from the moving atoms were assigned to Langevin thermostats. The rest of the atoms including the entire middle shell were kept as active. As the innershell moved out of the MWNT, the force resistance was recorded by the atoms using

the 1.0 nm band of moving atoms. The axial load is recorded as a function of displacement until the innershell dislodged from the MWNT.

The distances between the shells of the MWNT are 0.34 nm and are large enough to resist atomic friction on a pristine MWNT. Therefore, the chiralities of the MWNT have little effect on the pullout forces. When a pristine MWNT is tested for sword-in-sheath failure by pulling out the innermost shell at a rate of 40 m/s, the simulations predict that the middle shell also travels in the axial direction of the pullout for 5.0 nm or more if the innershell does not break free from the middle or outer shells.

The variations in the force curves over displacement during inner-tube sliding for the Ar-irradiated, electron-irradiated, and non-irradiated MWNTs are plotted in Figure 4-5. The curves show that there is a dramatic increase in the pullout force on the irradiated MWNTs when compared to the pristine MWNT. There are also differences in the pullout mechanism based on the type of irradiation process. Specifically, the localized defects from ion irradiation allow the innershell of the MWNT to break its crosslinks. This type of deformation follows a plastic-type behavior. The electron-irradiated MWNT has a radial distribution of crosslinks and its innershell breaks during pullout. It requires a higher pullout force and breaks with a much shorter displacement than the ion-irradiated pullout, which is comparative to a brittle type fracture.

The differences in the curves for the ion-irradiated and electron irradiated pullout suggest that there is a dependence on radial distribution of crosslinks on the pullout force. To explore the distribution effect, crosslinks were induced in two armchair MWNTs, one with a radial distribution to mimic an electron irradiated MWNT (full radial MWNT or FRMWNT) and the other half radially distributed to mimic an ion-irradiated MWNT (half radial MWNT or HRMWNT). Both have a crosslink density of 2.3/nm which is approximately the same number

of crosslinks produced in the electron irradiated MWNT and the same pullout rate of 40 m/s. The results of these simulations are shown in Figure 4-6.

In the case of the HRMWNT the innermost shell does not break, but the crosslinks between the inner shell and the middle shell do break as the innershell is dragged out. When the innershell of the FRMWNT is pulled, it breaks within itself similar to the electron irradiated MWNT pullout. The FRMWNT needed a higher force for pullout than the HRMWNT. In addition, the FRMWNT shows the same brittle type of fracture as the electron irradiated MWNT since the crosslinks are efficiently holding the nanotube in place and do not let it plastically deform. The HRMWNT shows the same plastic type of fracture as the ion irradiated MWNT. The crosslinks in these cases are concentrated on one side of the tube and therefore the nanotube is flexible enough to slide with respect to its outershells. Therefore, the crosslink distribution of the MWNT has an effect on the breaking mechanism as well as the pullout force.

The region of both curves up to 11.0 nm of displacement in Figure 4-6 indicates that the innershell experienced elastic stretching as the links between the shells contribute to the linear rise in the force. The drop and oscillations in the HRMWNT's force curve show when bonds between the middle and outer shell have broken. The slight rise in the force curve between 100 ps and 140 ps is indicative of where the links between the middle shell and inner shell contribute to the pullout force, until no more links are left to hold the shell in place.

Figure 4-7A and B shows how the ideal FRMWNT and HRMWNT are comparable to the electron irradiated and ion irradiated MWNT, respectively. In particular, the electron irradiated MWNT has a similar crosslink formation as the FRMWNT and breaks the same way, as indicated in the sudden drop in the forces in Figure 4-7A. The trend in the two curves are almost identical yet there is a slight difference in the time it takes to break the FRMWNT's innermost

shell, which is most likely due the effect of other defects (such as atomic disorder and vacancies) on the behavior of the electron irradiated MWNT.

Figure 4-7B shows more variation in the force curve than Figure 4-7A, however the trend is the same for the HRMWNT and Ar-irradiated curve. This comparison shows that the MWNT pullout is affected by other defects, such as atomic disorder and vacancies, to a much larger extent than the electron-irradiated MWNT. Unlike the HRMWNT pullout where the middle shell smoothly separates from the outershell first, the innermost shell of the Ar irradiated MWNT rips from the rest of the tube first. In particular, there is a slight drop in the force curve of the Ar-irradiated MWNT at 10 nm where the weakest parts of the MWNT break. The rise in the force curve, at displacements of 10.0 nm to 35.0 nm, shows where the links between the middle shell and outer shell are resisting the inner shell pullout.

The effect of pullout rate on the results is examined by considering two pullout rates of 40 and 20 m/s for the electron irradiated MWNT, and the results are shown in Figure 4-8. The slower pullout rate, or strain rate, yields a higher modulus than the faster pullout rate. This is because the lower pullout rate gives the nanotube atoms more time to relax. This, in turn, adds resistance to the pullout modulus.⁵⁷ Nevertheless, the maximum pullout force is about the same for both pullout rates, as are the qualitative responses of the nanotubes to pullout.

Conclusions

The simulations here showed how irradiation can induce defects and crosslinks between shells on MWNTs and how different types of irradiation, CF₃, Ar, and electron, effect the “sword-in-sheath” deformation. Specifically, MWNTs with defects and crosslinks on the upper radial part, as with the ion irradiated MWNTs, shows a plastic type of deformation when the innershell is pulled axially from the outer shell. Conversely, on tubes where the crosslinks are radially distributed, result of the electron irradiated MWNT; the pullout deformation exhibited a

brittle type fracture. The force to pull out the electron irradiated MWNT is significantly higher than the pullout force for the ion irradiated MWNT. In all these cases, the hybridization analysis showed that the MWNT maintained its integrity and a relatively small concentration of crosslinks significantly reduce sword in sheath deformation.

Table 4-1. The hybridization of the carbon atoms in the armchair and chiral MWNTs following irradiation.

	Armchair			Chiral		
	<i>Ar</i>	<i>CF₃</i>	<i>Electron</i>	<i>Ar</i>	<i>CF₃</i>	<i>Electron</i>
<i>sp</i> ³	1.5%	1.7%	1.0%	1.5%	1.6%	1.0%
<i>sp</i> ²	97.6%	97.7%	92.3%	97.9%	98.2%	90.6%
<i>sp</i>	1.2%	0.6%	6.6%	1.1%	0.0%	7.9%

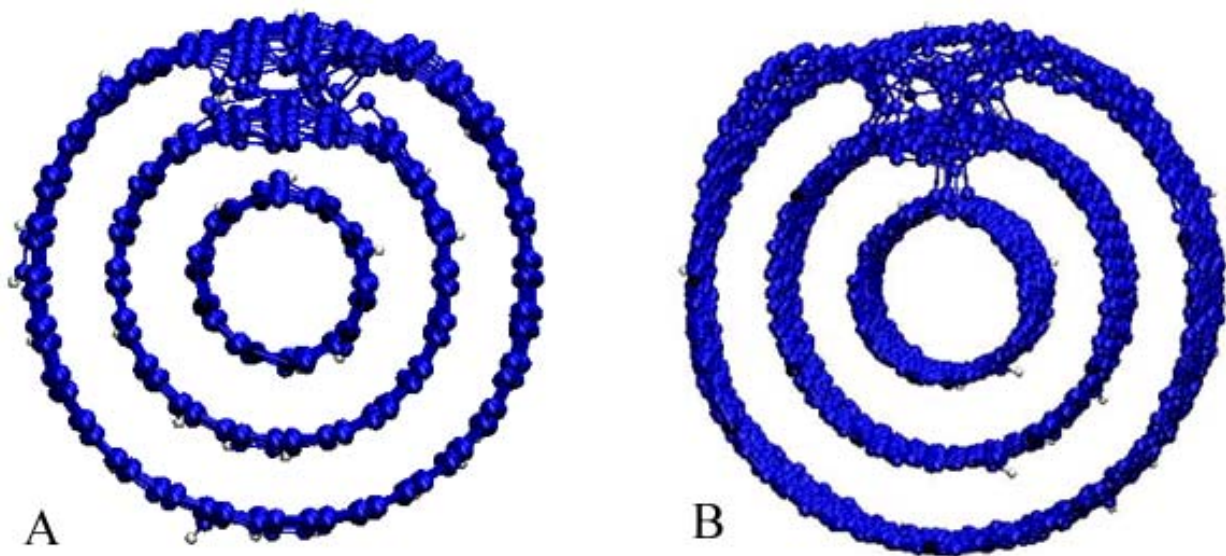


Figure 4-1. Side view snapshots of Ar irradiated A) armchair and B) chiral MWNTs following irradiation by a beam of 50 Ar ions at 50 eV/ion and equilibration.

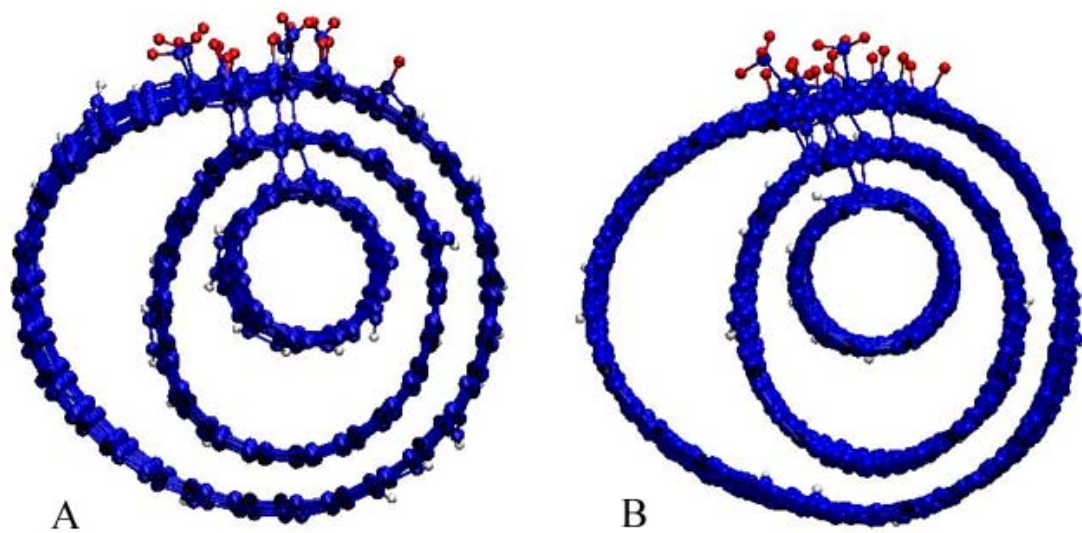


Figure 4-2. Side view snapshots of CF_3 irradiated A) armchair and B) chiral MWNTs following irradiation by a beam of 50 CF_3 particles at 50 eV/ion and equilibration.

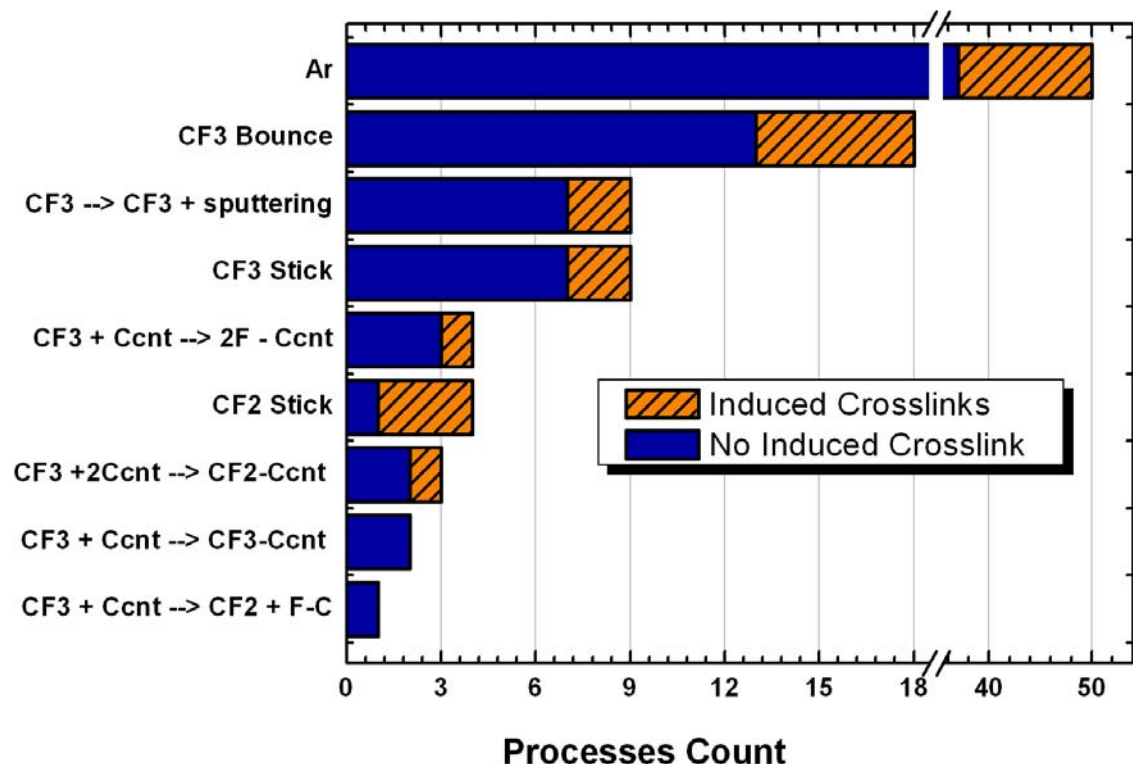


Figure 4-3. Crosslink count from the processes of CF_3 and Ar impact during irradiation at 50 eV/ion. C_{cnt} are carbon atoms pertaining to the carbon nanotube.

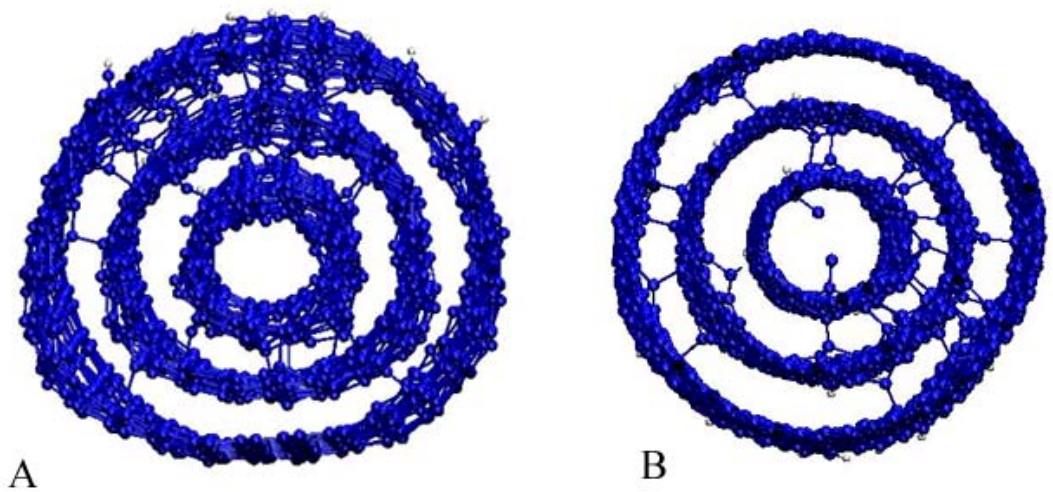


Figure 4-4. Side view snapshots of electron irradiated A) armchair and B) chiral MWNTs with a simulated beam of 50 virtual electrons through the PKA approach. The conditions correspond to an electron source of 50 keV.

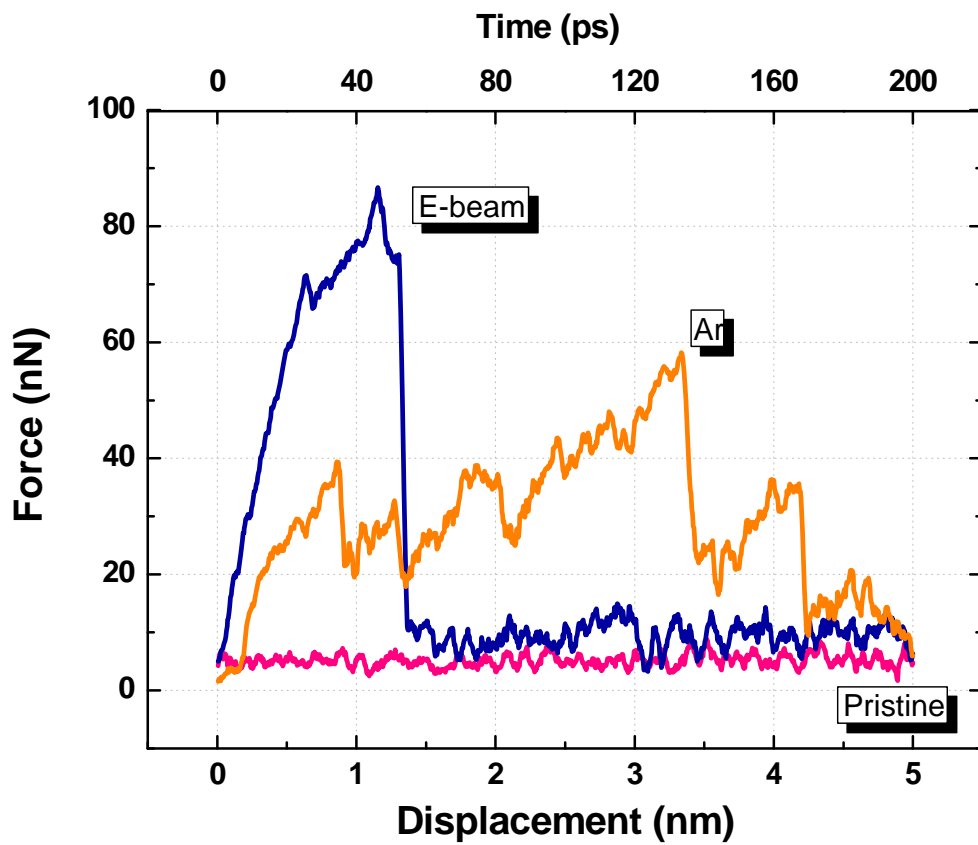


Figure 4-5. Simulated mechanical innershell pullout of electron-irradiated MWNT, Ar-irradiated MWNT, and pristine MWNT at 40 m/s. The features in the force curves are correlated to snapshots from the respective simulations.

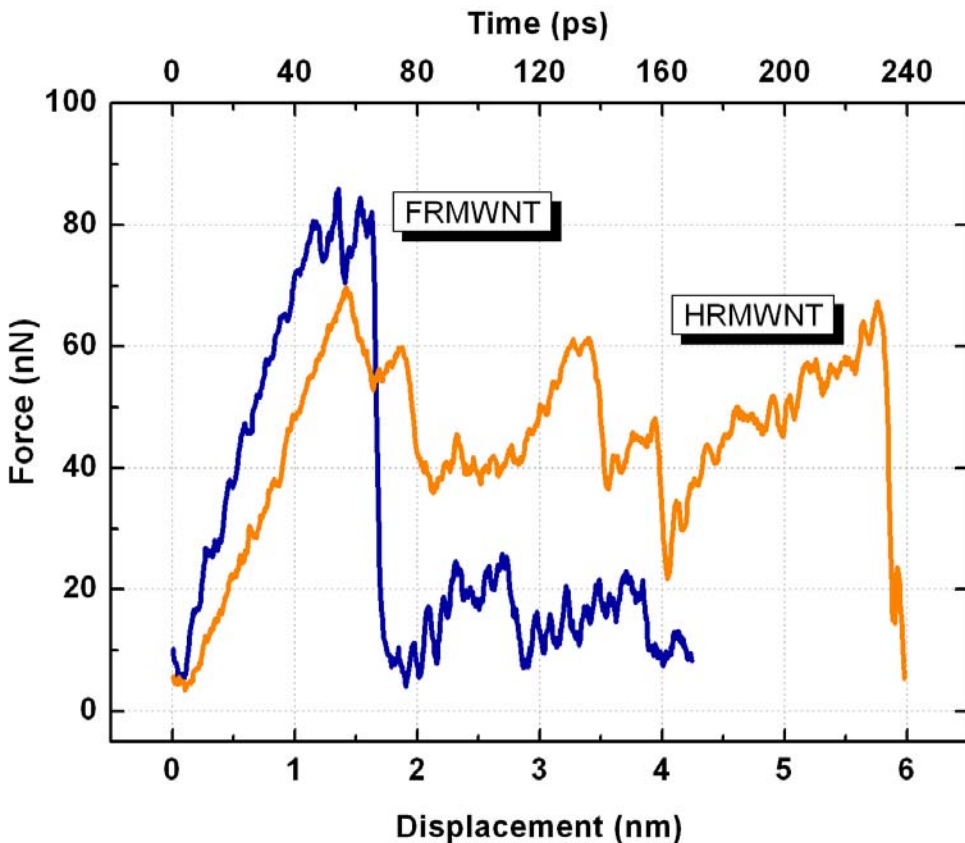


Figure 4-6. Simulated mechanical pullout of the innermost shell at 40 m/s of the FRMWNT and the HRMWNT.

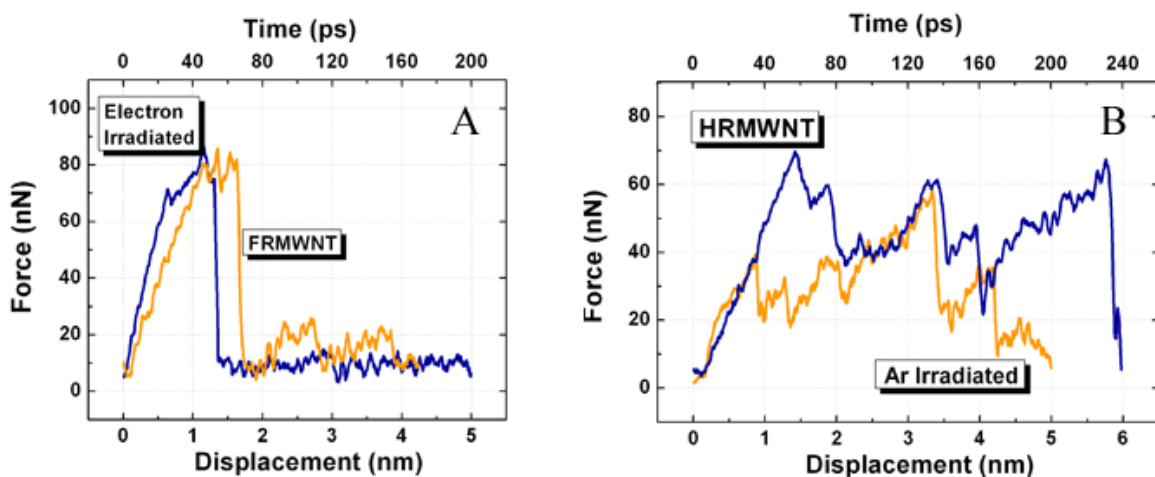


Figure 4-7. Simulated mechanical pullout of the innermost shell at 40 m/s of the A) electron irradiated MWNT compared to the FRMWNT and B) the Ar irradiated MWNT compared to the HRMWNT.

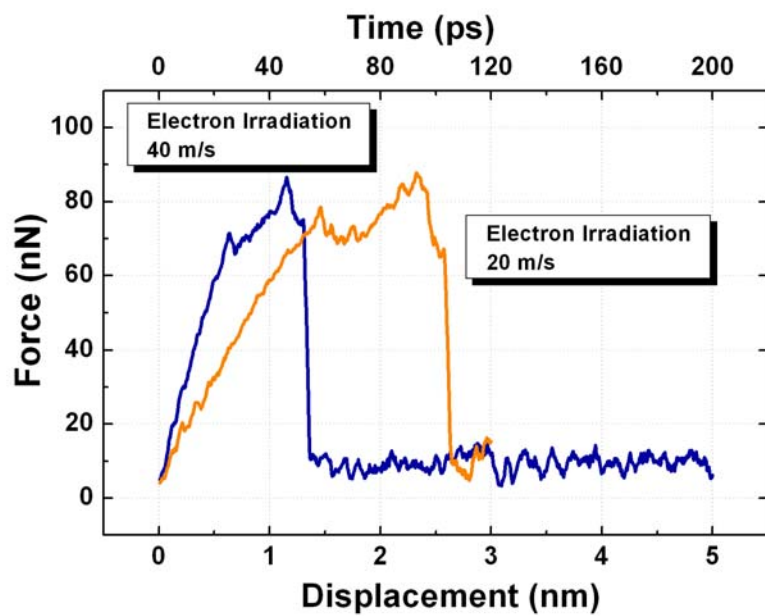


Figure 4-8. Effect of pullout rate on the electron irradiated MWNT. A slower rate decreases the pullout modulus.

CHAPTER 5

ARGON BEAM MODIFICATION OF NANOTUBE BASED COMPOSITES

The previous chapter discussed irradiation and pull out forces in bare MWNTs to simulate an experimental procedure where CNTs were modified before they were mixed with a polymer matrix. Here a similar study is performed on pristine CNTs of different types embedded in a polymer matrix. Different types of carbon nanotubes were used to investigate how the curvature plays a role during irradiation considering neighboring tubes or inner shells, such in a double-walled CNT. The composite is irradiated and then pulled out with respect to the polymer surrounding, in collaboration with Byeongwoo Jeong.

The study here not only investigates the interfacial strength between the CNT and the polymer matrix post-irradiation, but also structural changes to the composite as whole. Carbon nanotube composites are used for materials in low orbital satellites which are exposed to low energy bombardment from free radicals and ions. The previous chapter gave insight to how a MWNT responds to ion bombardment. In pure polymer systems, irradiation etches the surface away, decreasing the material's longevity.¹⁴² The effect that the CNTs have in the polymer and their contribution to etching effects after irradiation are observed, as well as limited sword and sheath deformation.

Ar deposition on polystyrene-carbon nanotube composites is examined on three different carbon nanotube – polystyrene composites. The nanotubes were then pulled axially with respect to the polymer surround to analyze effect of the irradiation-induced cross-linking and polymer etching on the mechanical properties of the composite.

System Background

Three different composites were examined, and each had a different arrangement of the carbon nanotube under two layers of polystyrene, shown in Figure 5-1. The first structure is a

bundle of four (10,10) SWNTs, the second is a (5,5) @ (10,10) DWNT, and the last was a (10,10) single walled nanotube (SWNT).

Langevin thermostats are applied to each structure in a heat bath formation to mimic the thermal dissipation that occurs in macroscale composites. All three composites have the same irradiation area (160 nm^2) and percentage of thermostat atoms (60%) even though the bundle composite has 15% more polymer volume than the DWNT-PS and SWNT-PS.

The Ar atoms in the beam have an incident energy of 80 eV/atom. The system temperature is maintained at 300 K by the thermostat atoms even though local heating at the site of impact may occur at the site of impact. Each structure, single-walled, double-walled, and bundle composites, has the same temperature during the irradiations.

Each structure is allowed to relax at 350 K for 10 ps and then cooled to 300 K before deposition for 20 ps until the potential energy oscillates around a constant value. The spacing of the Ar atoms in the beam is far enough so the structure has 1.8 ps to equilibrate between impacts. The entire deposition process takes 200 ps to complete and is held at 400 K for 20 ps before being cooled to 300 K for 20 ps.

Results

Effects on Irradiation

Polyatomic irradiation of C_3F_5 was performed in collaboration with Yanhong Hu on the SWNT-PS structure from Figure 5-1B with varying angle and incident energy. The incident beam angles considered are 0° , 30° , and 45° from the normal angle and the energies were 50 eV/ion and 80eV/ion. The results are shown in Table 5-1. The system size and computational resources were too small to effectively simulate the 80 eV beam at 45° . Nevertheless, the trend in Table 5-1 indicates that increasing the beam angle decreases the penetration depth of the ion. In addition, there is a higher percentage of ion implantation for both energies at 30° . At this angle,

the beams suffer fewer steric interactions with the PS chains compared to the beams deposited at normal angles and 45°. In all cases, the incident energy of the incident particles of 50 eV is not high enough to functionalize the SWNT under two layers of PS chains.

In subsequent simulations, the effect of CNT type in a CNT-PS composite during Ar irradiation at normal incidence was considered. Figure 5-2 shows snapshots of the final structures after Ar deposition and equilibration. The trajectories show that some Ar atoms remain in the surface following deposition, while others bounce off or diffuse out after impact. The figure also illustrates how the nanotubes and the composites as a whole have changed under Ar irradiation. The carbon nanotubes' modification is analyzed by the hybridization of the carbon atoms. In particular, the sp and sp^3 hybridization of the carbons are counted after each set of 5 deposited Ar. Each count is averaged over five (four for the DWNT-PS system) trajectories and presented as a percent of the total number of carbon atoms in each nanotube system.

Figure 5-3A indicates that the SWNT has more sp -hybridized atoms than the SWNT bundle or the DWNT following irradiation. This is because the carbon atoms on the nanotube wall have more space available to form a “punch-out” defect, where a carbon atom bonds with the lattice is partially broken but does not break free. The atoms around the defect on the SWNT wall react chemically with atoms from the surrounding PS since there is no inner shell. The opposite trend is seen in Figure 3b, where the DWNT has more occurrences of sp^3 -hybridization that reflects the fact that the inner shells of the DWNT are able to form more cross-links.

Defects that occur on the outer shell of the DWNT are more readily functionalized with the inner shell than with the neighboring PS, since the inner shell of the DWNT is under more strain and is therefore more reactive than the PS chains. However, the top of the DWNT closest to the surface experiences more damage than the portions further from the surface, and, consequently,

has a higher density of cross-links with the polymer matrix. Many of the sp^3 sites on the SWNT wall are bonded with polymer fragments or hydrogen atoms rather than linking with the polymer backbone. Under irradiation, the hydrogen atoms on the PS backbone require less energy to dissociate from the backbone than a carbon atom and more H atoms are available to react with the CNT.

Figure 5-4 indicates the average percentage of Ar atoms trapped in the composite following irradiation and equilibration. The outer shell of the DWNT and the SWNT are the same diameter so they take up the same volume inside the PS matrix and the volume of polymer in both cases. However, the SWNT composite traps more Ar atoms than does the DWNT composite.

The bundle-PS composite has significantly fewer Ar atoms trapped in the matrix than either the SWNT-PS or the DWNT-PS composites. The irradiation area is the same for the three composites, but the bundle-PS composite has less polymer volume than the DWNT-PS or SWNT-PS composites and consequently fewer opportunities for the Ar atoms to be trapped in the polymer matrix.

Figure 5-2 also indicates that the DWNT-PS composite has fewer trapped Ar atoms than the SWNT-PS composite. The inner shells in the DWNT make the overall nanotube stiffer than the SWNT^{46,143}, which cause incoming Ar atoms to bounce off the DWNT and still have enough energy to eject from the composite. The SWNT is more flexible and absorbs some of the incident energy which prevents the Ar atom from bouncing out. During the collision, some of the Ar atom's incident energy is transferred to the DWNT and, as a result, the number of carbon atoms dislodged from their initial lattice positions is high. In the case of the more flexible SWNT, the energy that is transferred from the impacting Ar is more easily dissipated by SWNT vibrations

and by the surrounding polymer. As the simulations proceed, this difference in mechanical response influences the number of Ar atoms that remain embedded within the composites following impact, with more remaining in the SWNT-PS composite than the DWNT-PS composite.

Bare bundles of DWNTs and SWNTs were built and irradiated with Ar at the same incident energy of 80 eV to better understand the nature of the differing responses of the SWNT-PS and DWNT-PS composites under irradiation. Figure 5-5 shows axial views of the bundles after the deposition of 40 Ar atoms. The figure clearly indicates that the structural changes are more significant in the case of the DWNT bundle than the SWNT bundle. Niyogi et al.⁴¹ suggested that the curvature of CNTs shift the π orbitals so that they are denser on the convex side, which is also consistent with the increased bonding predicted here. Therefore, CNTs with smaller radii are more reactive⁴¹ than CNTs with larger radii since the smaller tubes are under more strain than the larger tubes. There are fewer links between the neighboring DWNTs than the SWNTs, which implies that the inner tubes in the DWNT reacted more readily compared to its outer shells.

When a DWNT embedded in a polymer composite is irradiated, its behavior is somewhat different than its bare counterpart. The defective sites that result from Ar bombardment may not necessarily react with the innershell, but can also react with neighboring polymer chains. In the case of the bare SWNT bundle, the nanotubes have many cross-links between their neighbors. In contrast, the SWNT inside the PS matrix does not cross-link with the chains as much as the DWNT.

Over the course of the irradiation, the polymer region above the nanotube is etched away, but the nanotube effectively protects the PS regions below it. On average, the Ar atoms reached a

depth of 27 Å in the Bundle, 27 Å in the SWNT and 30 Å in the DWNT. Comparing Ar irradiation simulations on pure PS, the polymer etches away more rapidly without any nanotube barriers. On average, the Ar atoms penetrate the pure polymer surface 25% deeper than comparable depositions on the composites. Thus, the simulations predict that the presence of nanotubes embedded within the PS limits the depth and extent of surface etching.

Over time, the polymer over the carbon nanotube is etched away thus exposing the nanotube to more direct impacts. Figure 5-6 illustrates the average number of products emitted from the composite after irradiation and equilibration. Products of lower atomic weight are more common with those with higher atomic weight. Most of the products consist of C₂H_n fragments, such as C₂H₂, but there are incidents of larger fragments, including some with masses greater than 70 g/mol.

Figure 5-6 also indicates that there is no significant difference in mass distribution between the DWNT-PS and the SWNT-PS composites. The bundle-PS has fewer cross-links than the other two composites. It is interesting to note that the product emission from the bundle-PS composite is greater than the other two, even though its polymer mass is lower. The bundle array can be thought of a composite with a low degree of nanotube dispersion, as opposed to the SWNT-PS composite which is representative of a composite with high dispersion. This analysis implies that composites with low dispersion are more likely to emit polymer fragments upon irradiation than cross-link. Conversely, composites with higher nanotube dispersion were shown to have less polymer emission since there are higher volumes of polymer surrounding each fiber.

Nanotube Pullout Analysis

The pullout simulations were performed by Byeongwoo Jeong, a Visiting Scientist in the Sinnott group. Figure 5-7 plots the axial pullout forces of the nanotube systems before and after irradiation with respect to the surrounding PS. In the case of the unmodified SWNT-PS

composite the onset of slippage between the SWNT and the PS matrix occurs at a pullout load of about 0.1625 nN, as indicated in Figure 5-7A. The interfacial strength is predicted to be about 10.8 MPa, which is higher than the value of 2.8 MPa predicted previously.^{76,77,144} The difference is attributed to variations in the system's size and simulation conditions. For the unmodified DWNT-PS and bundle-PS composites in Figure 5-7A, the onset of slippage between the CNTs and the PS matrix occurs at a pullout load of about 0.095 and 0.100 nN, respectively which are lower rather than the value for the SWNT-PS. However, the pull out load is low and the nanotubes are short (3 nm long) so comparing the pullout loads quantitatively is difficult.

In Figure 5-7B, the irradiated SWNT-PS based composites has an onset of initial slippage between the SWNT and the PS matrix at 0.305 nN, and the CNT pulls out from the PS matrix at a pullout load of 0.790 nN. These values are about 1.88 and 4.86 times higher, respectively, than the value the unmodified SWNT-PS composite. The hybridization analysis showed that there are not many cross-links between the PS backbone and the SWNT wall relative to the DWNT-PS system. However, there are many sites where the carbon atoms on the SWNT wall bonded with hydrogen. These extensions hinder the pullout movement of the SWNT. If there were more cross-links between the PS backbone and the nanotube the pullout force would be expected to be even higher.

In the irradiated DWNT-PS composite, Figure 5-7C, the onset of initial slippage between the DWNT and the PS is 0.560 nN, and then the CNT pulls out of the matrix at a pullout load of about 1.333 nN, 5.89 and 14.03 times higher, respectively, than the value in the unirradiated composite counterpart. The significant increase in pullout force when compared to the SWNT-PS composite is because there are more crosslinks between the shell(s) and polymer in the DWNT-PS.

The irradiated bundle-ps system has its two topmost SWNTs in the bundle closest to the surface are bonded to each other and to the PS matrix, Figure 5-7D. Thus, when the pullout loads are applied to all SWNTs in the bundle, the two lower SWNTs are pulled out of polymer matrix in the same way as the unmodified composites. However, the topmost tubes have higher pullout loads. This suggests that bonds between SWNTs in the bundle are as important as those between the SWNTs and the PS to achieve a significant increase of pullout forces or interfacial strength between the bundle and matrix.

To determine the pullout loads for the topmost SWNTs in the bundle, the pullout loads are applied to only these two SWNTs. In this case, the onset of initial slippage between top two SWNTs and the PS matrix occurs at a pullout tensile load of about 0.255 nN, and the CNTs pull out of the PS matrix at a load of about 0.850 nN. These values are about 2.55 and 8.50 times higher, respectively, than the value in the case of unmodified bundle-PS composites.

Conclusions

Three different systems of carbon nanotube-polystyrene composites were irradiated with 100 Ar atoms that had incident energies of 80 eV were examined: a DWNT-PS composite, a SWNT-PS composite, and a bundle of four SWNTs in PS composite. The carbon hybridization analysis shows that there is a significant difference between the three systems when considering the bonding of the carbon nanotube(s). The curvature of the carbon nanotube plays a role in the defects under irradiation. Nanotubes of smaller curvature are more ready to react, and are more reactive on the outside or convex portion of the tube. The DWNT has more occurrences of cross-links between its shells than with the neighboring PS. A comparative analysis done by irradiating bundles of DWNTs and SWNTs show a similar distribution of cross-links. The DWNTs would rather link the outer shells with the inner shells than form cross-links to neighboring structures, regardless of whether the neighbors are another nanotube or the polymer matrix.

An analysis of the distribution of the emitted irradiation products by mass indicates that there is little dependence on the type of composite considered. The occurrences of products for all three systems are similar. The majority of the products that were emitted have molecular weights of about 30 g/mol; however, there are several occurrences of products with molecular weights up to 100 g/mol. The differences in polymer emission when comparing the bundle-PS results to those of the DWNT-PS and SWNT-PS composites suggest that dispersion among the nanotubes in the matrix does have an effect on product emission and cross-linking. Composites that have less polymer volume around the nanotube tend to cross-link less and emit more.

Table 5-1. Effect of incident angle during C_3F_5 irradiation on a SWNT-PS composite. The system size and computational resources were not large enough to effectively model angles higher than 30° for 80 eV, however the trends are apparent for 50 eV. “Bond” means that a chemical bond was predicted to form on the time scales of the MD simulations. The penetration depth is given in terms of nanometers and defines how far below the particle traveled below the substrate surface.

	80eV			50eV		
	Penetration Depth	% Implants	Bonds	Penetration Depth	% Implants	Bonds
0°	2.8	38.7	Yes	2.1	42	No
30°	1.6	50	Yes	1.5	55	No
45°	0	0	No	1.4	45	No

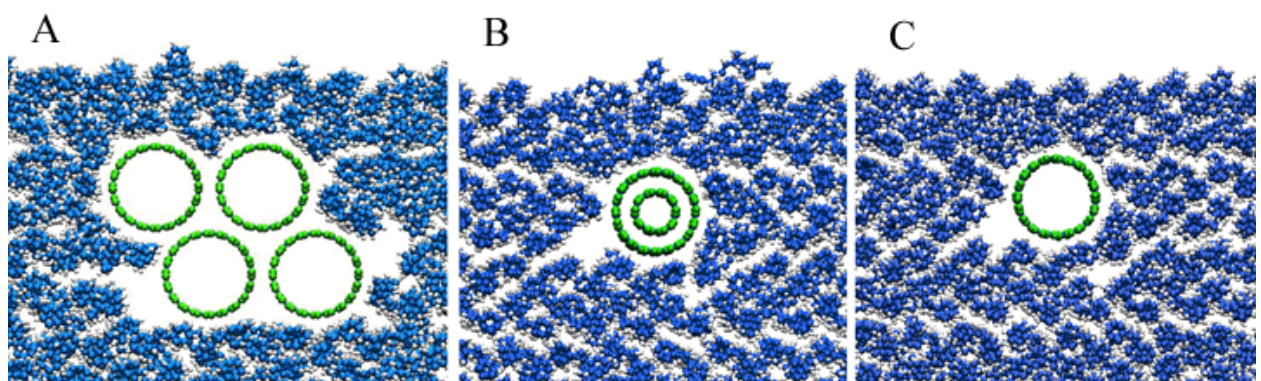


Figure 5-1. Nanocomposite structures of A) Bundle, B) DWNT, and C) SWNT before irradiation.

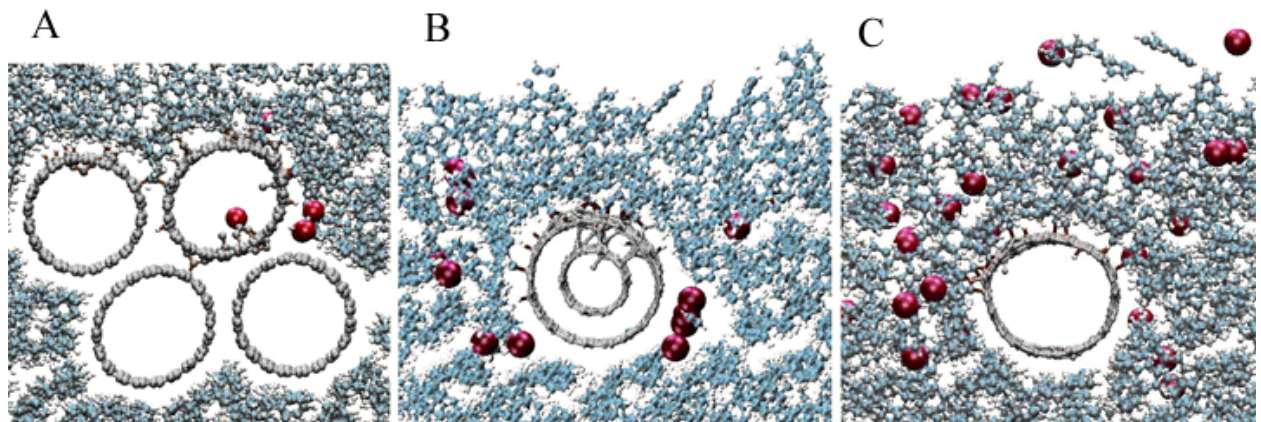


Figure 5-2. Snapshots of A) Bundle, B) DWNT, and C) SWNT composites after 100 Ar irradiated particles at 80 eV/ion. The Ar particles are shown in pink.

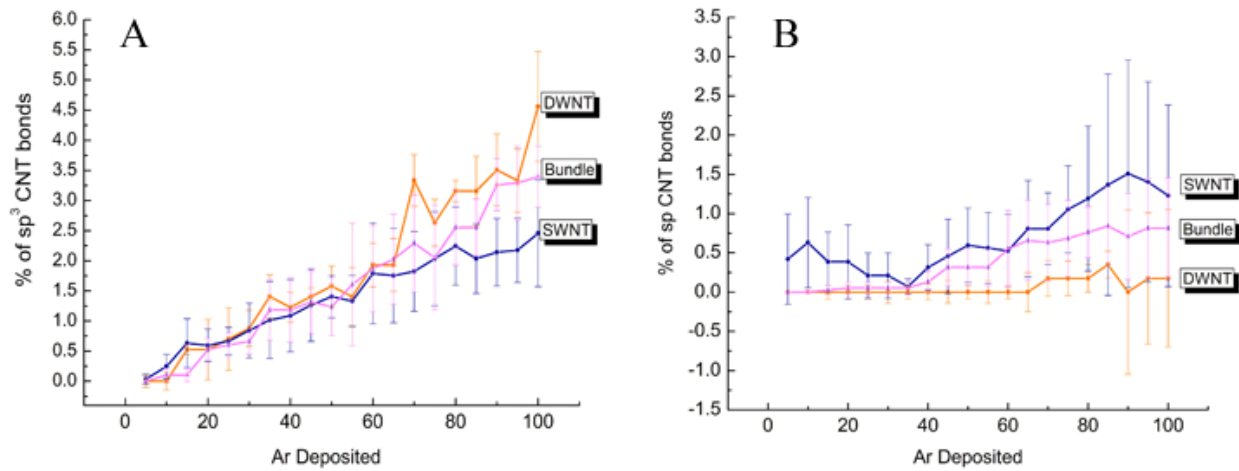


Figure 5-3. Hybridization analysis of CNT, A) sp^3 analysis B) sp analysis on the carbon nanotube(s) damage under Ar irradiation.

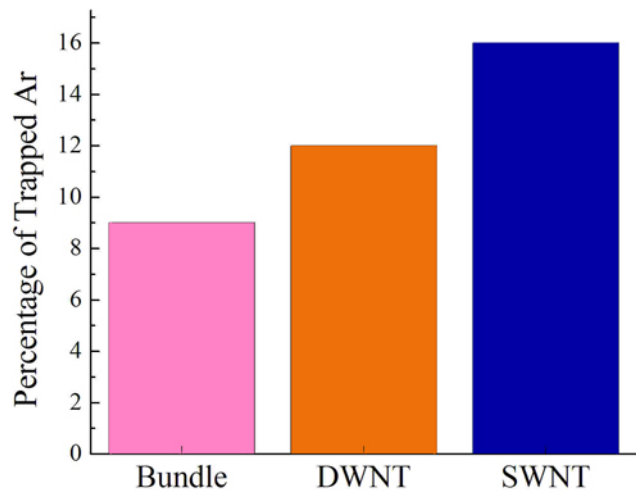


Figure 5-4. Average number of trapped Ar atoms.

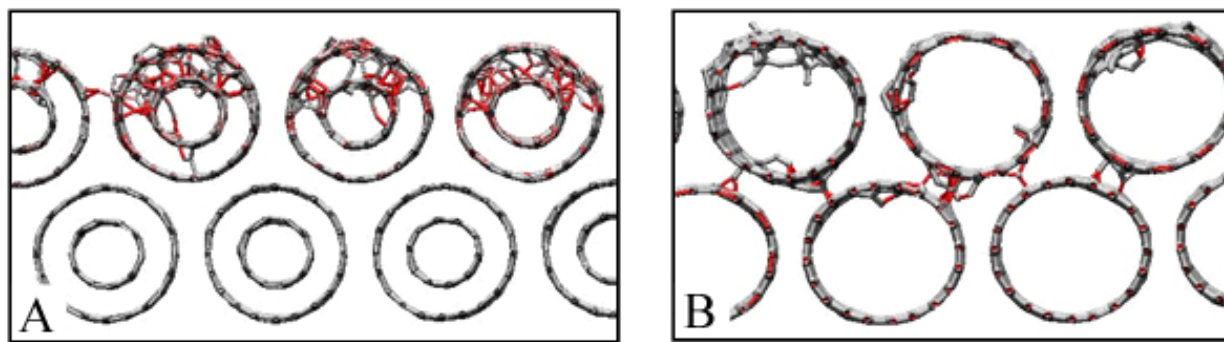


Figure 5-5. Effects of curvature in irradiation damage between A) DWNT and B) SWNT. The inner shell of the DWNT is stiffer and is more susceptible to breakage.

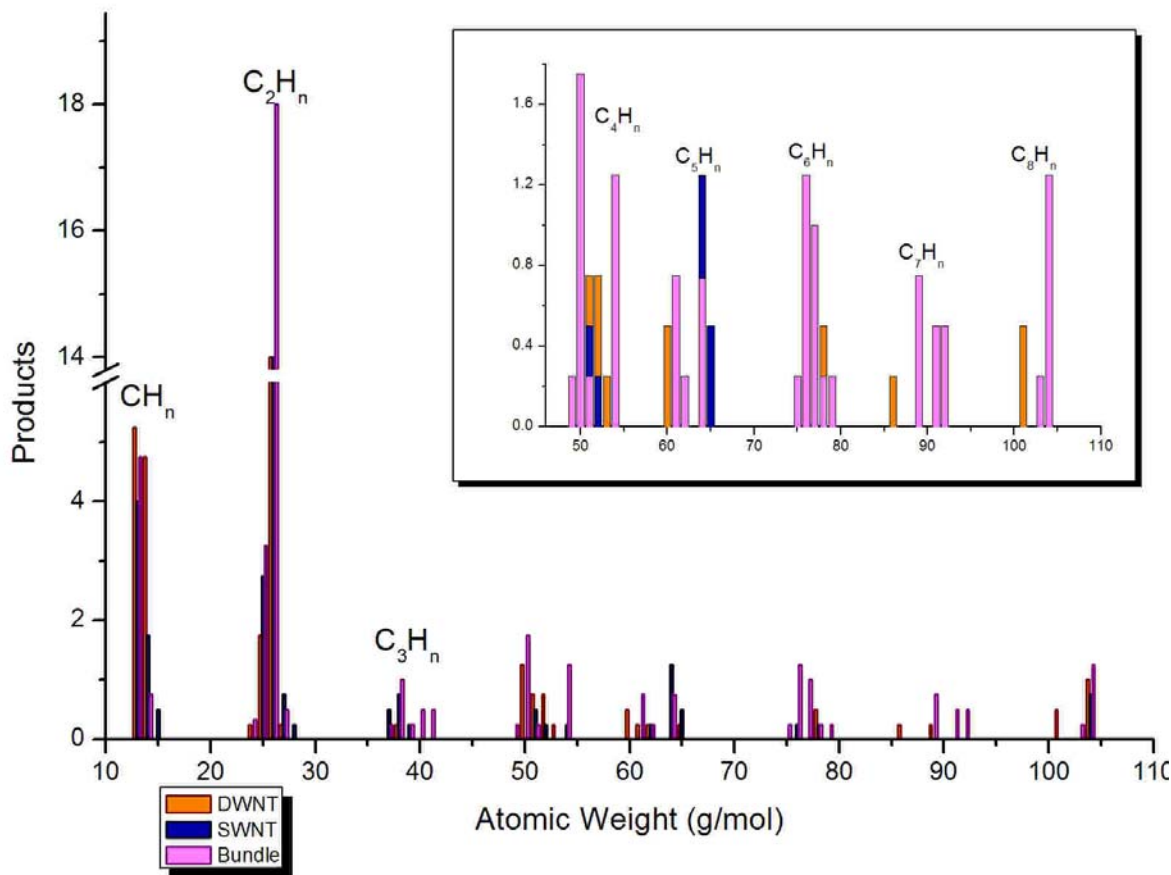


Figure 5-6. Average masses of the polymer products after irradiation and equilibration. The inset is a blowup view of the products greater than 50 g/mol.

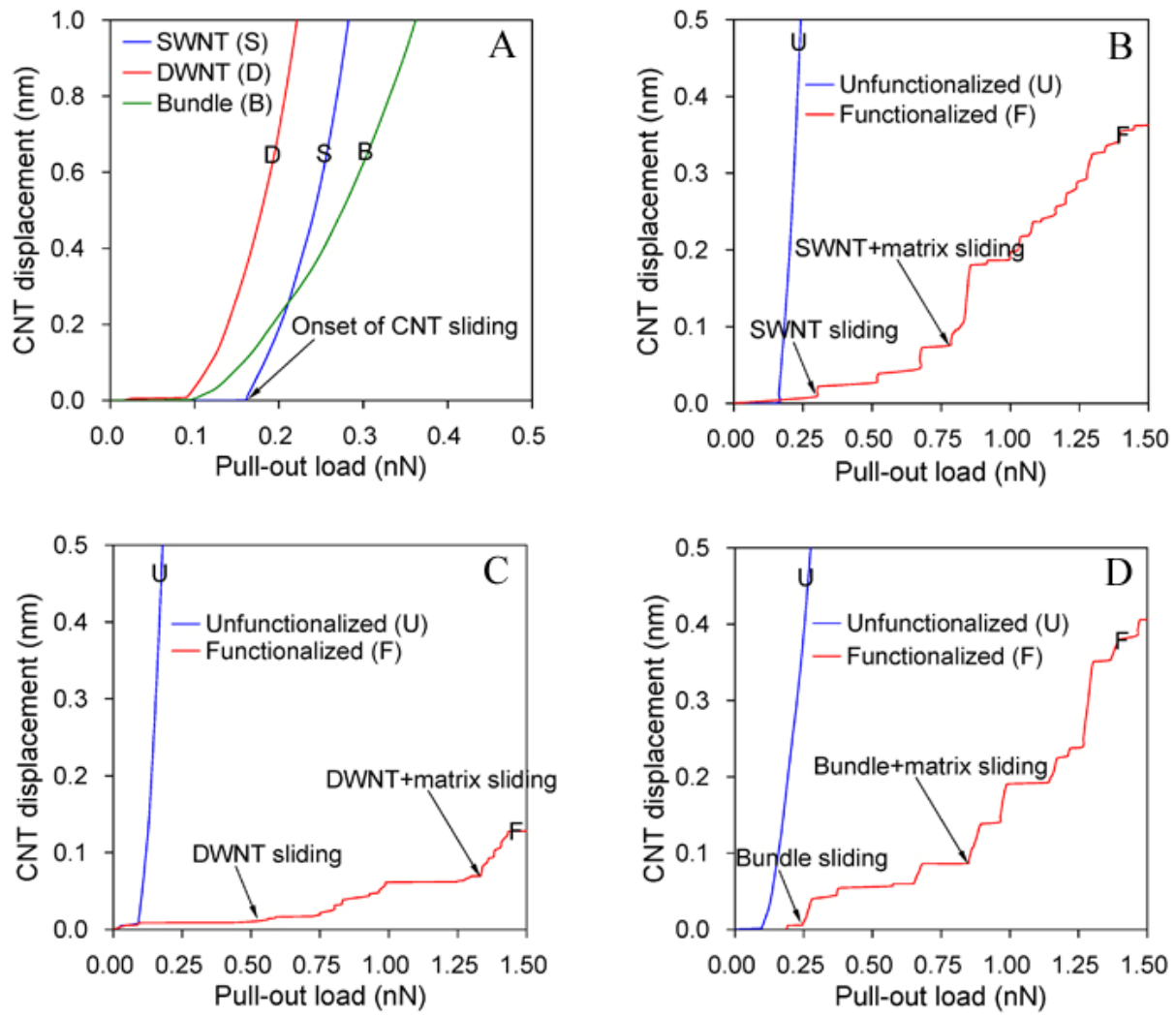


Figure 5-7. Pullout load curves of CNTs. A) Unfunctionalized nanocomposites. B) SWNT based composites. C) DWNT based composites. D) Bundle based composites. The displacement of functionalized Bundle is the value of two SWNTs of upper side

CHAPTER 6

MOLECULAR DYNAMICS AND MONTE CARLO STRUCTURE EVALUATION WITH ORGANIC SEMICONDUCTORS

The previous chapters reviewed the properties of carbon nanostructures for mechanical applications and composite technologies. Other applications of carbon nanostructures, particularly fullerenes and hydrocarbons, include functioning as organic semiconductors, photovoltaic cells, organic light emitting devices for display and lighting technology, photo detectors, and thin film transistors.

An important condition for the fabrication of organic photovoltaic cells is an active region of phase separated donor and acceptor molecules percolated on the nanoscale to ensure ideal efficient exciton diffusion and charge collection. There have been numerous ways to obtain this ideal structure.^{145,146}

This chapter discusses a joint project with the Xue group at the University of Florida that combines experimental characterization of pentacene:C₆₀ films with computational simulation. The computational work examines thin films of pentacene and C₆₀ molecules that are mixed together at different molecular ratios to determine how their morphology ultimately affects their performance in experimental devices.

System Background

Mixtures of pentacene and C₆₀ of different ratios were built with two different methods. In the first approach, named the periodic method, different unit cells of pentacene and C₆₀ were created manually at particular molecular ratios, and replicated in three dimensions. In the second approach, a builder was used to produce thin films of pentacene and C₆₀ with random orientation. Both sets of structures were then relaxed in molecular dynamics (MD) simulations. The goal was to investigate the difference the initial morphology has on the final equilibrated structure.

The cohesive energies were calculated for bulk C₆₀ and bulk pentacene using the AIREBO potential and are compared to experimental results in Table 6-1. The calculations show that the energies from AIREBO are relatively close to the values given by experiment.^{147,148} The AIREBO potential was fitted for hydrocarbon molecular interactions.¹²⁷ Parameters such as enthalpy, pair correlation functions, and bond energy were fit with experimental values. The relative close values of the cohesive energies in Table 6-1 verifies that AIREBO is an adequate tool for studying the short range and long range evolution of the pentacene:C₆₀ films.

Intermolecular interactions across a pentacene:C₆₀ interface are shown in Figure 6-1. The C₆₀ region packed as a face centered cubic FCC, which is how C₆₀ is in crystalline solid form. Pentacene molecules form a triclinic structure. At a molecular separation of 0.25 nm across the interface of the (100) planes for both crystals, the predicted minimum interaction energy is -6.31 eV/atom. This value is comparable to the interaction energy for the C₆₀:C₆₀ system of -6.82 eV/atom, while the pentacene-pentacene system interaction energy minimum is -5.50 eV/atom at intermolecular separations of 0.20 nm.

Ordered Structures

One approach to generating virtual films of pentacene and C₆₀ to be examined in atomic-scale simulations was to build a sample unit cell and repeat it in three dimensions. For this dissertation, this method will be labeled the “ordered structure” approach. Three such ordered structures were built in different initial configurations of pentacene:C₆₀ at a (1:1) molar ratio at various overall molecular densities. In particular, the fullerene molecules were arranged into a face-centered closed pack (FCC) or body- centered closed pack (BCC) arrangement with the pentacene molecules added in the appropriate molar ratio to maximize the density of the sample. A simple cubic (SC) structure was also constructed with a distinct C₆₀ and pentacene interface. Figure 6-2 illustrates the three structures after equilibration for the A) 1.08 g/cm³ density, SC

separated structure, B) 0.78 g/cm³ density, FCC mixed structure and C) the 0.49 g/cm³ density, BCC mixed structure. Figure 6-2A was built with a distinct interface between the C₆₀ and pentacene molecules, whereas B and C consisted of one pentacene and one C₆₀ in the repeating cell thus creating a distributed arrangement when the cell was duplicated.

Another structure of pentacene:C₆₀ at a 6:1 molar ratio, illustrated in Figure 6-3, was built in attempt to achieve a high density structure. Six pentacene molecules were curved around each C₆₀ molecule, which was labeled the ‘orange-peel’ pattern. The unit cell was repeated as a SC structure to make a supercell with a density of 1.0 g/cm³ so the molecules had adequate room to translate in the given periodic boundaries, as was the case for the structures from Figure 6-2A.

Random Structures

A different set of films were generated with a film builder program that uses elements from Monte Carlo (MC) simulations to randomize the rotation and translation of two different molecules. During experimental thermal deposition, the molecules are ejected from two separate nodes and are assumed to be completely mixed when they reach the sample substrate. Therefore, a new tool was programmed for computational studies to construct films of two different molecules with random orientation. Monte Carlo is ideal for this type of simulation because of its use of randomly generated numbers.¹¹⁹ A general illustration of the MC technique and algorithms is the approximation of π . A circle is inscribed in a square and random points are plotted throughout the square. If the points are uniformly distributed, then the portion of the points those are inside the circle to the portion that are inside the square are approximately, $\pi/4$, specifically:

$$\pi \approx \frac{4\tau_{hit}}{\tau_{shot}} \quad (6-1)$$

The accuracy of π depends on the quality of the random number generator. For example, if the points were plotted in a corner of the square, then the points are not uniformly distributed, or if a few points appeared throughout the square then the results would give a poor approximation of π .

The nature of the MC method is used here to construct films that have a truly random orientation. The random number generator constructed films where molecules' positions are determined in an arbitrary manner. The layer would not start with a repeated cell, but would be truly amorphous within the given periodic boundaries. This approach assumes that the initial structures are not ordered, which is a better analog to the experimentally deposited films where the molecules are deposited at thermal temperatures and are not expected to undergo much rearrangement from their initial, random positions on the surface.

The random film builder starts with coordinates of two different molecules, and creates a list to match the user defined ratio and number of desired molecules. Each molecule is then randomized about its origin and translated across a given plane. The equations for x, y, and z rotations and translation based on matrices are given as:

$$\begin{aligned}x' &= \cos(\phi) \cos(\Theta) x - \sin(\phi) y - \cos(\phi) \sin(\Theta) z + dx \\y' &= \sin(\phi) \cos(\Theta) x + \cos(\phi) y - \sin(\phi) \sin(\Theta) z + dy \\z' &= \sin(\Theta) x + \cos(\Theta) z + dz\end{aligned}\tag{6-2}$$

The random film builder program produces an atomic packing factor of 0.56 for bulk, randomized C₆₀ molecules which is consistent with the random packing factor for perfect spheres at 0.59-0.63.¹⁴⁹

Before these new random coordinates are accepted, the distances between all the molecules' center of masses must be greater than a given value depending on the types of

molecules used. If a deposited molecule is not too close to previously deposited molecule then the move is accepted and the new random coordinates are saved. Otherwise, new random translations and rotations are predicted until it fits on the plane.

The random film builder program generates single layers of pentacene and C₆₀. Three distinct layers were superimposed to create a 5x5x6 nm supercell. The distances between the centers of each layer were placed 1.1 and 1.3 nm apart depending on how the randomization affects the interface of the layer beneath. The ratios generated were pentacene:C₆₀ (1:1) molar ratio and pentacene:C₆₀ (1:2) molar ratio.

Equilibration Using Molecular Dynamics

Molecular dynamics simulations were used to relax mixtures of C₆₀ and pentacene, whether the films were built with the random film builder or the periodic approach, to allow for the relaxation of the system and molecular mixing or separation to occur. For this system the potential energy curve as a function of molecular position is considered as a flat potential energy surface. However, there are numerous local minima which can be obtained by varying the initial structures of the molecules, which is the motivation for building an ordered and random pentacene:C₆₀ structure.

After the films were built, they were allowed to evolve using MD and the AIREBO potential. Two different methods of equilibration were used to mimic experimental deposition rates. Experimental high deposition rates were mimicked by setting all the atoms in the system to be Langevin thermostat atoms that were heated to 300 K. When the system reached the desired temperature, the thermostat was lifted, allowing all the molecules to evolve in time according to Newton's equations with no constraints. In contrast, low deposition rates were mimicked by first equilibrating sections of the film (33% of the entire supercell, one layer at a time) before the next section was "deposited". This method was only performed on the random built films. In

experimental film deposition, lower molecular deposition rates give the molecules ample time to equilibrate before the next set of molecules appears. On the other hand, during higher deposition rates, the molecules have a shorter time of equilibration as many molecules are being continuously deposited.

The morphology of the films with differing molecular ratios was analyzed. Effects such as molecular segregation, stacking, and mixing were determined and the results compared to the experimental findings.

Results

Phase Separation in Pentacene:C₆₀ Mixtures

The phase separation in the pentacene:C₆₀ films made by experiment was investigated with X-ray diffraction or XRD with varying the mixing ratios of the two species. The crystalline planes surfaces of (001)' and (001) for pure pentacene was reported at $2\theta = 5.7^\circ$ and 6.1° respectively, with the inter-layer spacing d of 1.55 nm and 1.45 nm which agrees with the reported d value of thin film and bulk phases, shown in Figure 6-4. When C₆₀ is incorporated into the pure pentacene the higher diffraction peaks diminish which indicate there is a loss in the periodicity of the pentacene. The peaks disappear at the pentacene:C₆₀ (1:2) weight ratio. There are weak aggregations that are observed at the (1:1) weight ratio but no distinct diffraction peaks observed in the pentacene:C₆₀ (1:2) weight ratio suggest that the structure is amorphous.¹⁵⁰

Atomic force microscopy images (AFM) in Figure 6-5 were performed on A) pentacene, B) C₆₀, C) pentacene:C₆₀ (3:1) weight ratio D) pentacene:C₆₀ (1:1) weight ratio. Figure 6-5A of the pentacene shows complete coverage for the first layer, and island growth in the second and third layers. The AFM image of C₆₀, Figure 6-5B, shows a smooth surface with little features and indicates that the layer is amorphous with a root-mean-square surface roughness (R_{rms}) at 1.5 nm. The following AFM images of the pentacene:C₆₀ mixtures, C) 3:1 and D) 1:1 weight ratios, have

a higher R_{rms} than the pure samples and have a different morphology. Between the two ratios, the heavier pentacene mixture has smaller protrusions and more flat domains than the pentacene:C₆₀ (1:1) weight ratio mixture.¹⁵⁰ With the intensity changes in pentacene from XRD results in Figure 6-4, the flat domains are believed to indicate aggregation of pentacene, while the peaks are signs of amorphous pentacene.

Molecular dynamics were then used to equilibrate the structures of pentacene:C₆₀ (1:1) molar ratios whose final configuration is shown in Figure 6-2. From the image, it is clear that the C₆₀ molecules have a tendency to aggregate. The pentacene molecules also aggregate, but they do so to a lesser extent than the fullerenes. This is analogous to what is seen in the XRD and the AFM images where a higher concentration of C₆₀ molecules hinders high domains of pentacene aggregation. These simulations show that at low densities the molecules aggregate in a non uniform manner; however there is a degree of agglomerates between the same molecule types.

From the periodic structures, the pentacenes and C₆₀ show aggregation of similar molecules with one another without complete phase separation, as illustrated in Figures 6-2 and 6-3. Figure 6-3 shows snapshots of the pentacene:C₆₀ (6:1) molar ratio system after equilibration at 300 K. The pentacene:C₆₀ (1:1) molar ratio structures showed similar behavior in Figures 6-2B and C. The structure in Figure 6-2A shows a thicker region of C₆₀ and pentacene when compared to Figure 6-2B and C. The density of the structure in Figure 6-2A is larger than B and C and the structure started as completely phase separated rather than mixed as with B and C. However, this shows that the molecules have a preference to mix rather than stay in their respective non-crystalline phases.

The pentacene:C₆₀ (6:1) molar ratio structure showed that the pentacene molecules tended to stack commonly in pairs and even up to four molecules whereas the stacking in the (1:1)

molar ratio structure had very few pentacene stacking. Figure 6-3B is a snapshot of the pentacene structure isolated from the C₆₀ from the (6:1) molar ratio and shows the stacking of pentacene molecule. After equilibration the stacked pentacene in Figure 6-3B was analyzed by quantitatively counting based on the molecules' agreement in directional vectors and plotted in Figure 6-6. The results indicate that about 25% of the pentacene molecules stack in pairs while 10% of the molecules form stacks of three or four pentacenes. The stacking of the pentacene is quantified as a combination of pairwise distance calculations with a correlation in a molecular vector. Each pentacene molecule is assigned a longitudinal and transverse vector, which are used to match up with neighboring pentacenes to determine a stacked pair. The distances between the pentacenes of interested are within a cutoff of 0.66 nm with a vector angle variation of 10°. The aggregation and stacking of the pentacenes were also observed in the XRD and AFM results. The first peak in Figure 6-4 increases its amplitude as the concentration of C₆₀ molecules decrease. There are more pentacene molecules present and more chances for them to form a pair, or stack.

The fullerenes were isolated from the pentacenes in Figure 6-3C to show the aggregation of the molecules. A pair distribution of the equilibrated pentacene:C₆₀ (6:1) molar ratio structure from Figure 6-3C, showed that the system achieved an amorphous state and is plotted in Figure 6-7. When compared to the (FCC) mixed C₆₀ crystal, the peaks of the equilibrated C₆₀s show slight bumps in line with the FCC peaks. This suggests that there is some attraction between the C₆₀ in the mixture, and is not completely amorphous. As molecules translate in the supercell, trends such as C₆₀ agglomeration and pentacene stacking are apparent regardless of initial orientation. This phenomena is related to the flat nature of the surface potential energy and the different configurations are exploring the surface's local minima.

Controlling Film Morphology

The effects of morphology are described in this section in terms of two processing parameters, the mixing ratio and deposition rate. Figure 6-8 shows AFM images of pentacene:C₆₀ at weight ratios A) 1:1, B) 1:2, and C) 1:4. As observed in Figure 6-5, the bumps from the AFM images decrease as the density of C₆₀ molecules increase. In the pentacene:C₆₀ (1:1) weight ratio samples, the bumps are clear but they are nearly lost in the (1:4) weight ratio film. It is believed that these bumps are evolved from the flat domains observed in the thin mixed film and related to thin film pentacene phase aggregation. Figure 6-9 shows the pentacene:C₆₀ (1:1) weight ratios of different deposition rates A) 0.6 Å/s and B) 6 Å/s. The roughness between the two films is very different which indicates that deposition rate generates a more uniform structure where pentacene aggregation is suppressed.¹⁵⁰

In the MD simulations, pentacene:C₆₀ (1:1) molar ratios and pentacene:C₆₀ (1:2) molar ratios are considered under the conditions that mimic high and low deposition experimental results, that are described earlier in this chapter. Figure 6-10A illustrates the evolution of the (1:1) molar ratio film over 100 ps equilibration time. The aggregation behaviors are similar in this structure as well as distinct aggregation of pentacene and C₆₀ as shown in the previous simulations. Figures 6-10B and 6-10C shows the isolated pentacene and C₆₀ molecules, respectively to clarify the degree of aggregation. At the pentacene:C₆₀ (1:1) molar ratio, the pentacene does not show a strong tendency to stack when compared to films with a higher pentacene concentration. This is comparable to the XRD finding in Figure 6-4, which indicates that a decrease in pentacene concentration diminishes crystallinity or stacking. This trend is also seen in computational results as the pentacene:C₆₀ (6:1) molar ratio systems, where a structure that is pentacene heavy has more stacking than the pentacene:C₆₀ (1:1) molar ratios. The C₆₀ molecules have the same aggregation behavior as shown in the pair distribution graph in Figure

6-11. The curve is higher for the pentacene:C₆₀ (1:1) molar ratio than the pentacene:C₆₀ (6:1) molar ratio, which indicates that a higher concentration of C₆₀ results in more nearest neighbors, or agglomeration. The pentacene:C₆₀ (6:1) molar ratio structure is relatively heavy in pentacenes, which have a tendency to agglomerate and stack. Therefore, these pentacene domains prevent C₆₀ molecules from existing in larger groups.

In the low rate deposition simulation, each layer is equilibrated before the next layer is superimposed. In this case, the molecules have time to equilibrate on the surface before the next set of molecules is “deposited”. Within the first 10 ps of the MD simulation relaxation of these films, the molecules contracted and showed a tendency to attract to each other as well as similar molecules aggregating which is comparable to the trends seen in the high deposition random structures and the ordered structures. Figure 6-12 shows the trajectories of the A) pentacene:C₆₀ (1:1) molar ratio and B) pentacene:C₆₀ (1:2) molar ratio structures. The structure with the heavier fullerene concentration, Figure 6-12B, showed more C₆₀ aggregation due to the presence of more fullerene molecules than in Figure 6-12A. However, the pair distribution plot in Figure 6-13 indicates that the radial distribution between the two systems is fairly similar. The height of the first nearest-neighbor peak for the pentacene:C₆₀ (1:2) molar ratio structure is slightly higher than the corresponding peak for the pentacene:C₆₀ (1:1) molar ratio. Higher C₆₀ concentrations result in more C₆₀ packing with itself. However, as Figure 6-13 indicates, the height difference is slight, which indicates that the above some critical concentration the extent of C₆₀ packing is relatively invariant. Importantly, the long-range C₆₀ packing is amorphous. Under lower deposition rates, the molecules have more time to relax and organize themselves. Furthermore, the fullerenes have a stronger radial distribution than in the high-deposition case, which indicates that the molecules had time to relax without being affected by steric hindrance.

Conclusions

A good understanding of DA mixtures is important to explore in order to achieve efficient organic heterojunction photovoltaic device. Experiment and computation methods were combined to investigate the morphology of C₆₀ and pentacene films. The cohesive energies of the molecules in AIREBO correspond to the referenced experimental values and provide quantitative information of the mixture morphology. Simulations show a similar trend to XRD and AFM results, where there is strong aggregation of pentacene.

Computation used two different methods to build the mixture for morphology study: cell multiplication and a random layer builder to generate the thin films. Between these two methods, the equilibration result was nearly indistinguishable. Pentacenes have continued to stack as well as C₆₀. However, the stacking nature of the pentacene is lost with a higher concentration of C₆₀. By using MD to equilibrate ordered and random structures of pentacene:C₆₀, similar trends of C₆₀ and pentacene aggregation and stacking were noticed and compared to experimental values. Pair distribution plots between C₆₀ molecules showed that there is short range order that is dependent on concentration which implies molecule agglomeration, and long range order that is independent of concentration and implies that the structures are amorphous. Using different initial configurations, whether it was ordered or random, allowed the exploration of different equilibration minima across the potential energy surface. Molecular dynamics allowed us to study the orientation of the films and their behavior on the molecular scale with varying ratios, initial structure, and simulated deposition rate.

Table 6-1. Cohesive energies calculated by AIREBO compared to experiment.

<i>eV / molecule</i>	AIREBO	Experiment
C ₆₀	1.70	1.74 ¹⁴⁷
Pentacene	1.38	1.30 ¹⁵¹

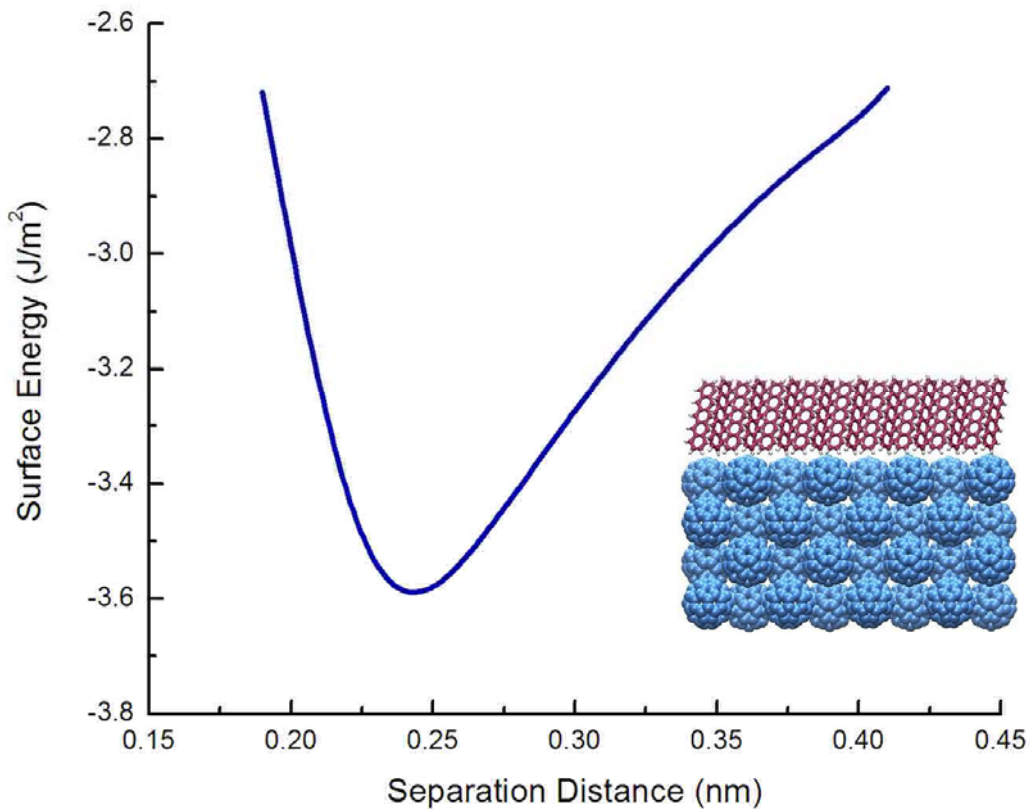


Figure 6-1. Plot of interfacial energy between (100) surfaces of FCC C₆₀ and (100) Pentacene.

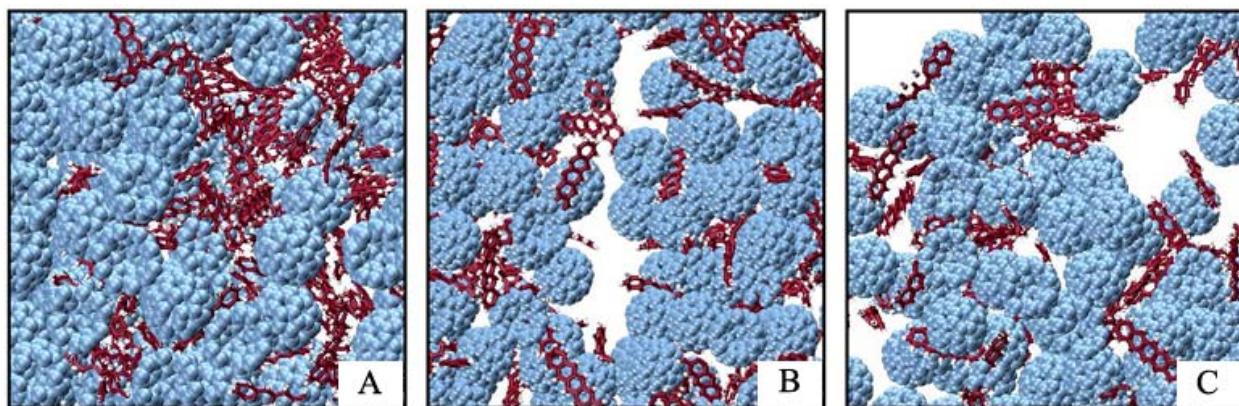


Figure 6-2. Pentacene:C₆₀ (1:1) molar ratios of A) 1.08 B) 0.78 and C) 0.49 g/cm³ structures that were built by the ordered method and equilibrated at 300K.

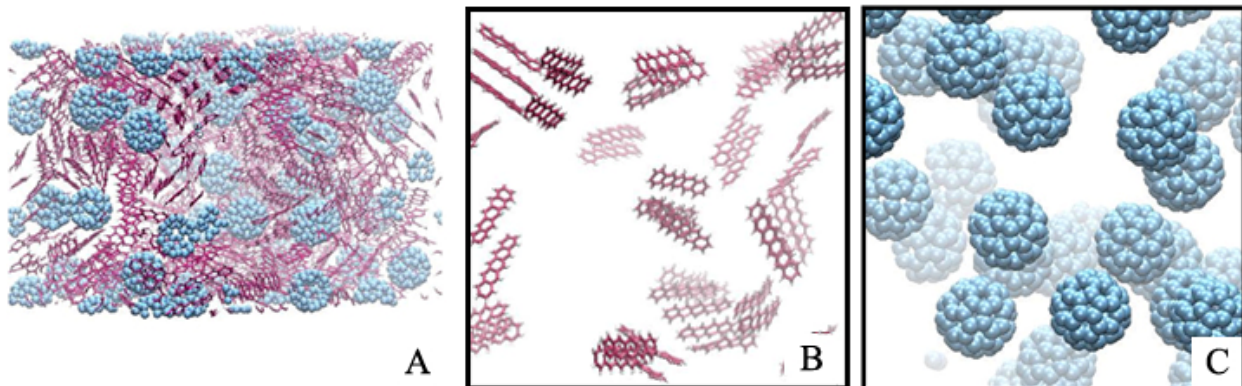


Figure 6-3. Molecular model of A) pentacene:C₆₀ (6:1) molar ratio mixture after 100 ps equilibration with B) the pentacenes isolated to clarify their stacking, and C) C₆₀ isolated Periodic boundaries are applied in three dimensions.

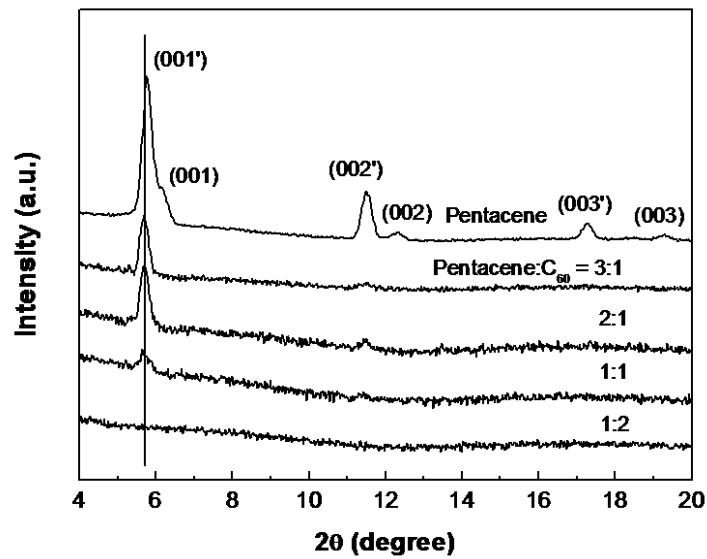


Figure 6-4. XRD pattern performed by Ying of pure pentacene and varying weight ratios of C₆₀.

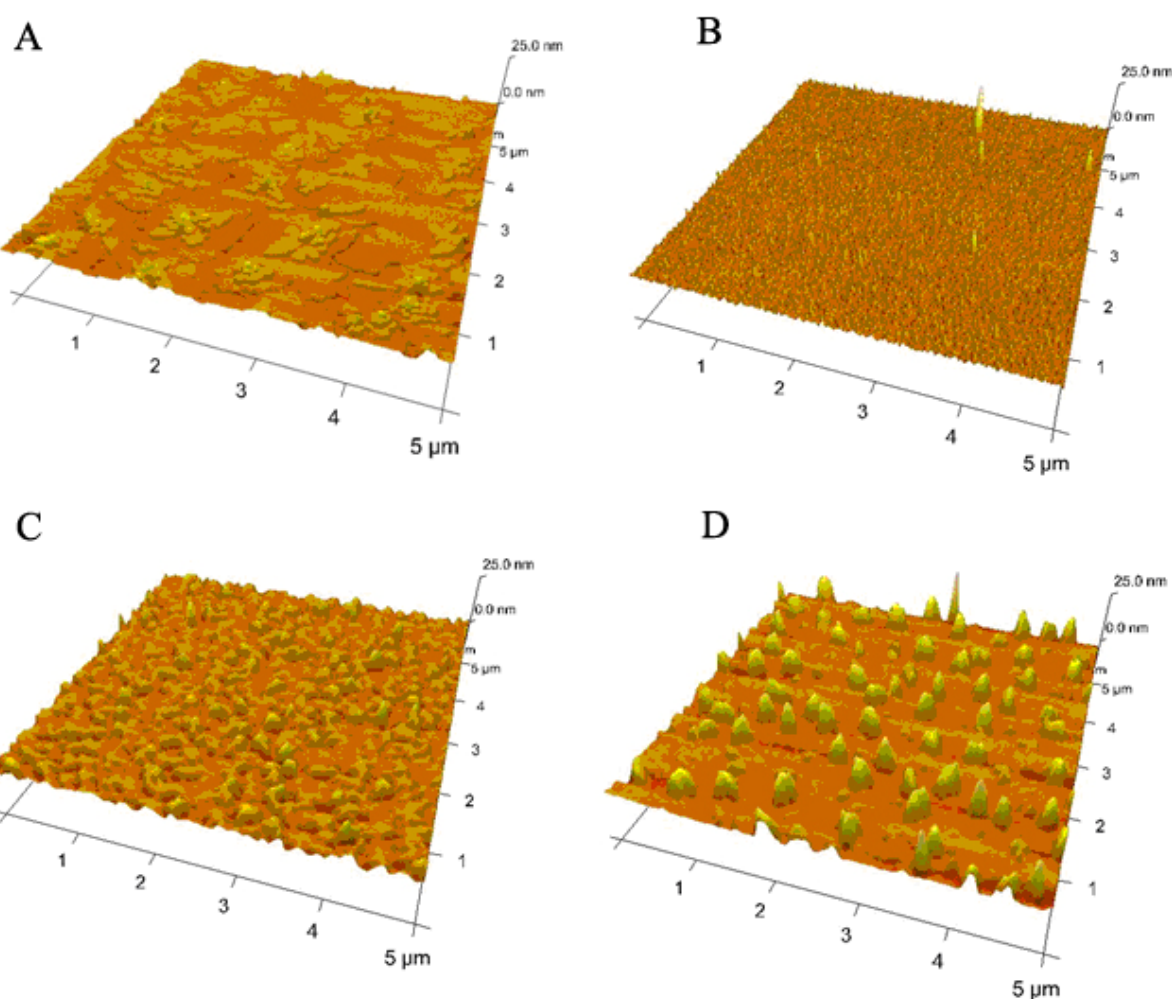


Figure 6-5. AFM images by Ying of A) pentacene, B) C₆₀, C) pentacene:C₆₀ (3:1) weight ratio
D) pentacene:C₆₀ (1:1) weight ratio.

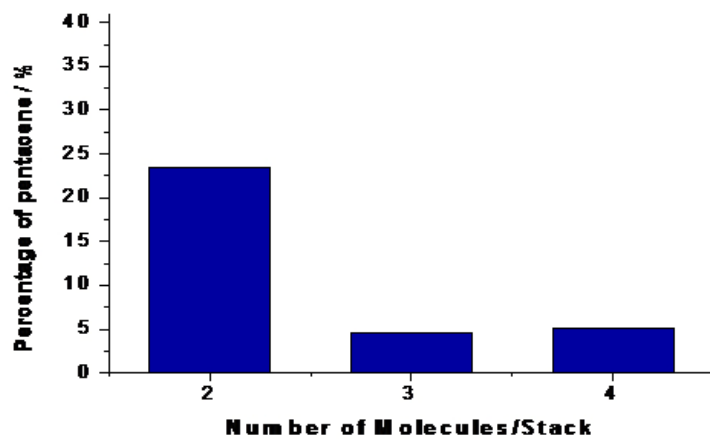


Figure 6-6. Pentacene stacking analysis for the pentacene:C₆₀ (6:1) molar ratio build by the ordered method.

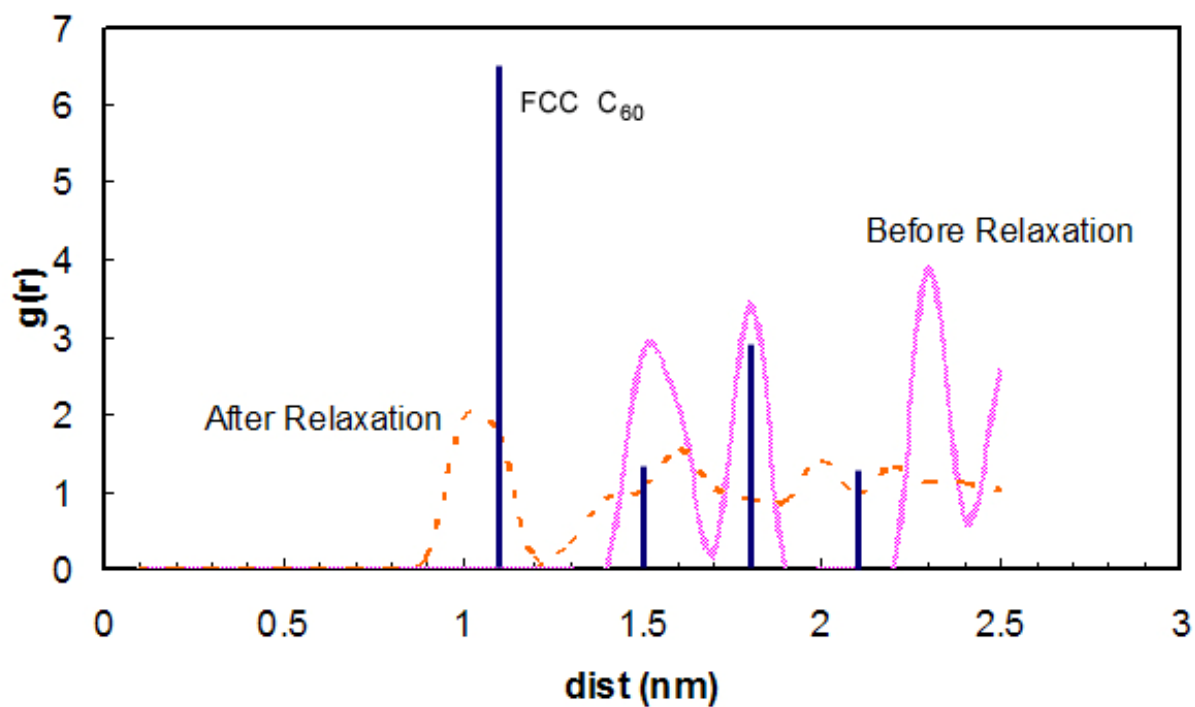


Figure 6-7. Pair distribution analysis of the C₆₀ interactions in the pentacene:C₆₀ (6:1) mixture after 100 ps equilibration.

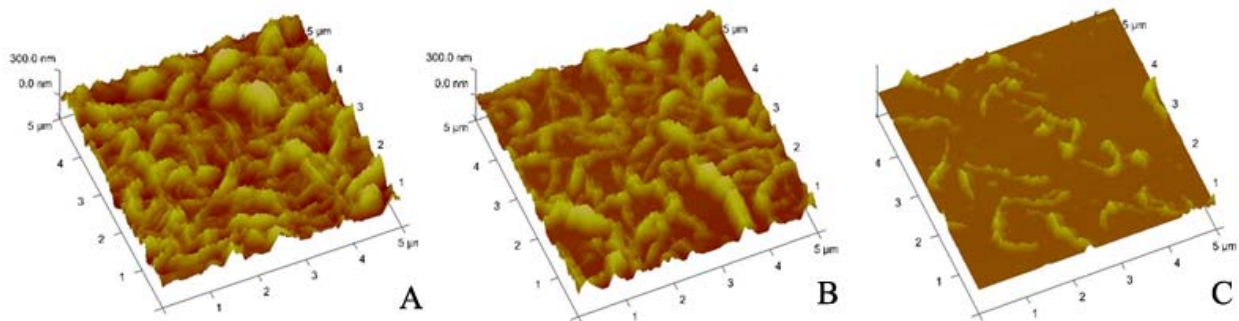


Figure 6-8. AFM images of pentacene:C₆₀ A) 1:1, B) 1:2, and C) 1:4. weight ratios deposited at 0.6 Å/s.

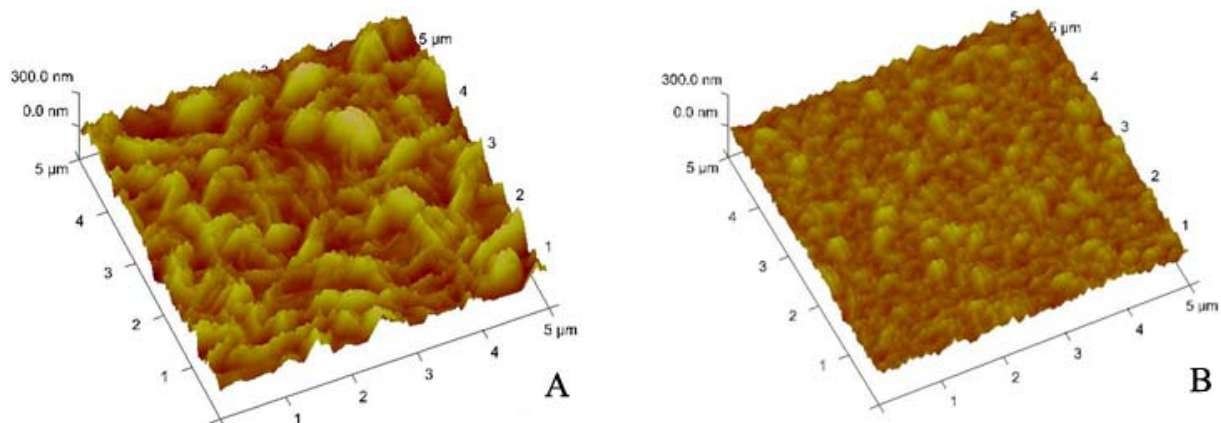


Figure 6-9. AFM images of pentacene:C₆₀ A) 1:1 weight ratio at 0.6 Å/s deposition rate and B) 1:1 weight ratio deposited at 6 Å/s.

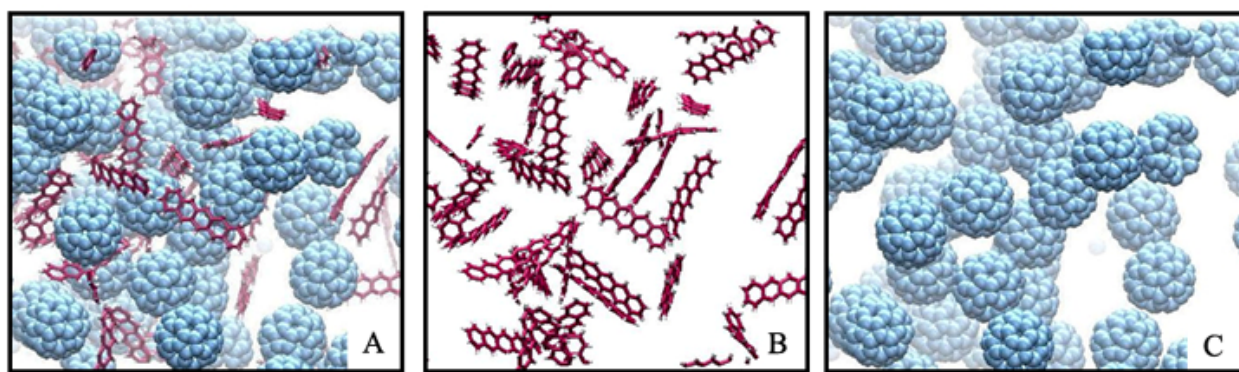


Figure 6-10. Random layer built C₆₀:Pentacene (1:1) molar ratio films A) 25 ps of relaxing at 300 K B) pentacenes isolated, C) C₆₀s isolated.

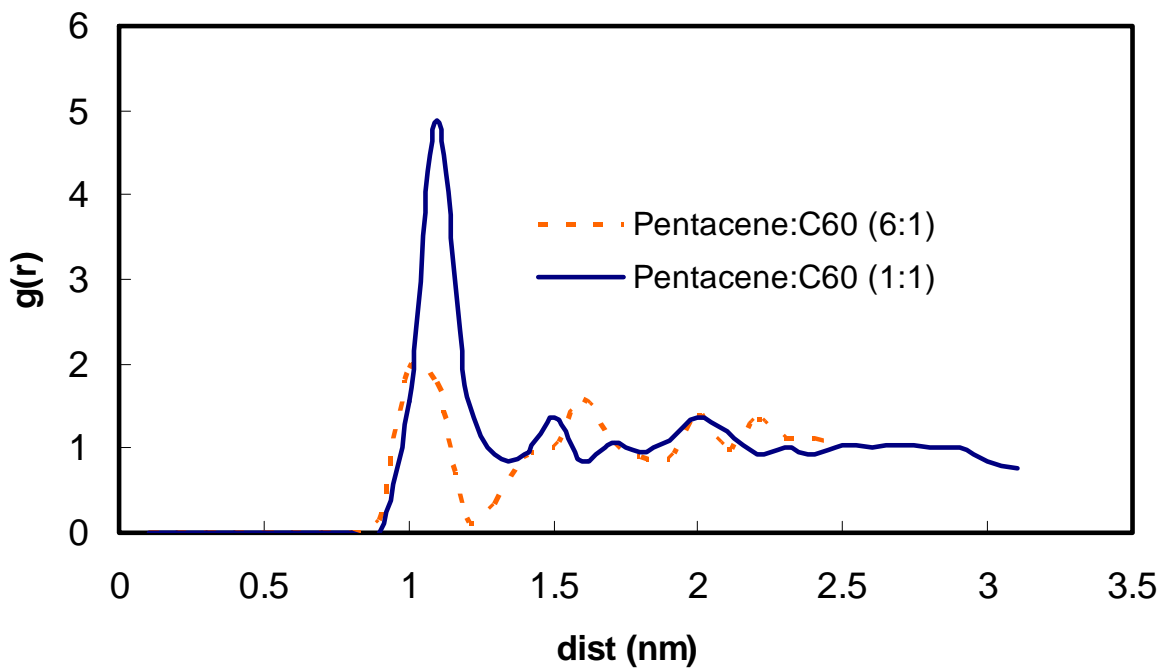


Figure 6-11. Pair distribution plot of FCC ordered (6:1) molar ratio and random built (1:1) molar ratio that were produced by the ordered method and equilibrated with MD.

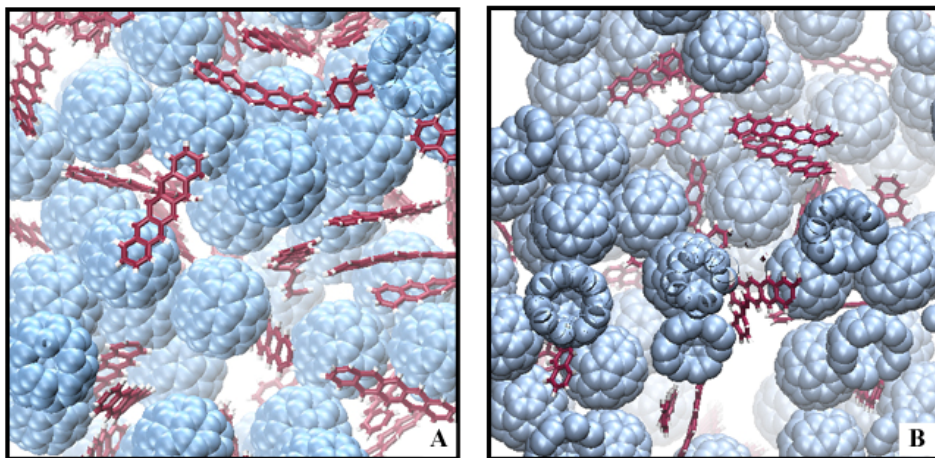


Figure 6-12. Random layer built films on low deposition A) pentacene:C₆₀ (1:1) molar ratio and B) (1:2) molar ratio.

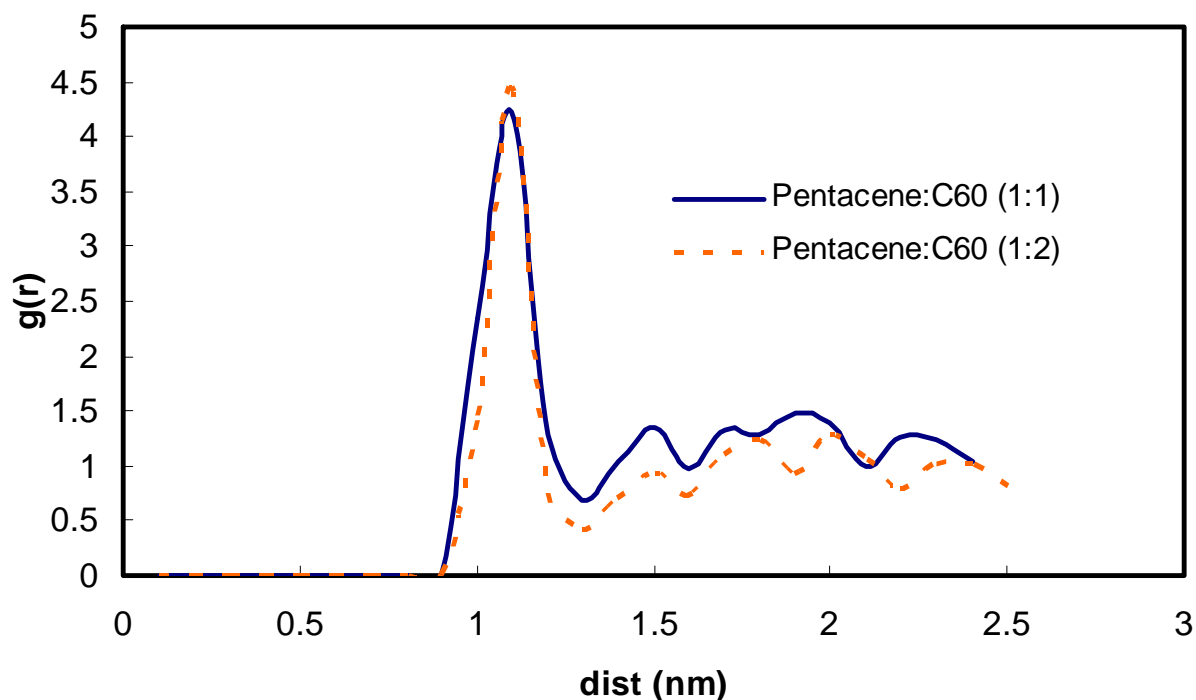


Figure 6-13. Pair distribution function plot between pentacene:C₆₀ (1:1) and (1:2) molar ratios that were produced by the random layer builder and equilibrated with MD.

CHAPTER 7 GENERAL CONCLUSIONS

The fundamentals of irradiation and nanomechanics were investigated in carbon nanostructures, graphite and various forms of carbon nanotubes, and carbon nanotube – polymer composites using classical MD simulations with the REBO or AIREBO potential. The potentials' effectiveness for describing short range and long range interactions was also used for investigating the morphology pentacene and C₆₀ organic semiconductors. The computational findings were compared with experimental results and gave insight to the morphology and chemistry on the atomic scale.

STM images had shown a broad site of defects over a graphite surface after being bombarded by Ar irradiation. AIREBO simulations of Ar irradiation in graphite showed an evolution of defects in three stages. First stage is where there is little damage, then starts to grow at the second stage of irradiation, and in the last stage starts to rearrange itself to be stable. These trajectories would be nearly impossible to monitor during an experimental irradiation procedure. The defect formation energies from AIREBO simulations were compared to DFT results and were found to be very consistent, therefore AIREBO is an adequate tool for illustrating how defects accumulate in graphite under repeated impacts.

MD has modeled how irradiation of different particles, CF₃, Ar, and an electron, has an effect on a MWNT's chemistry and as a result limiting sword in sheath deformation during axial strain. It has been found that the incident particle that impacts the MWNT has an effect on the cross link distribution in the radial direction. The crosslink density across the MWNT's radial face determines how the MWNT will deform under axial load. Particle irradiation that induced crosslinks on the upper portion of the radial face gave a plastic deformation pullout, while

electron irradiation affected the entire radial face of the MWNT which resulted in a brittle deformation pullout.

Since the interest of analyzing sword in sheath deformation in irradiated MWNT concerns with nanocomposite research, similar simulations were carried out on carbon nanocomposites embedded in a polystyrene matrix. Composites of this nature are of interest in satellite applications where these materials are in a heavy irradiation environment in the Earth's low orbit. Therefore, incorporating carbon nanotubes in polymers have been conducted to improve the surface chemistry of the composite, specifically resisting polymer etching. Three different structures were studied, DWNT-PS, SWNT-PS, and a bundle of four SWNTs in a PS matrix. Curvature of the nanotubes plays a significant role under irradiation. Tubes of smaller radii are under more stress and have a tendency to break under bombardment and are more reactive on the convex portion of the tube due to a shift in the π -orbitals. Emitted products and incident particle depth were analyzed after the composites were irradiated and found that dispersion of the nanotube in the polymer has an effect on product emission and crosslinking.

REBO and AIREBO packages were and ideal choice to use when modeling large (few nanometers) systems for carbon and hydrocarbon systems. The research topics mentioned above utilized a key feature in using (AI)REBO over standard molecular mechanic in which bonds can be broken and reform while keeping the correct atom hybridization. Other useful features in the AIREBO package is how effectively it can describe short and long range interactions in carbon nanostructures and small hydrocarbons. The morphology of organic semiconductor films of various pentacene and C₆₀ ratios have been studied with AIREBO and compared to XRD and AFM results to experimental built films. Cohesive energies were calculated under the AIREBO

potentials and were found to be very consistent with references results. Quantitatively, the computational results have been consistent with the findings from XRD and AFM analysis.

REBO and AIREBO have been proven to be an effective tool in modeling systems that are nearly unattainable by experiment. Irradiation, mechanical pullouts, and small molecule equilibration have shown various applications of research with carbon nanostructures where the features of (AI)REBO bridged with experiment can be a vital tool in carbon research.

LIST OF REFERENCES

- (1) Fahy, S.; Louie, S. G.; Cohen, M. L. *Physical Review B* **1987**, *35*, 7623-7626.
- (2) Frenklach, M.; Taki, S.; Matula, R. A. *Combustion and Flame* **1983**, *49*, 275-282.
- (3) Kroto, H. W.; Heath, J. R.; Obrien, S. C.; Curl, R. F.; Smalley, R. E. *Nature* **1985**, *318*, 162-163.
- (4) Kratschmer, W.; Lamb, L. D.; Fostiropoulos, K.; Huffman, D. R. *Nature* **1990**, *347*, 354-358.
- (5) Iijima, S. *Nature* **1991**, *354*, 56-58.
- (6) Terrones, M. *Annual Review of Materials Research* **2003**, *33*, 419-501.
- (7) Zhang, J.; Cheng, Y.; Lee, Y. Z.; Gao, B.; Qiu, Q.; Lin, W. L.; Lalush, D.; Lu, J. P.; Zhou, O. *Review of Scientific Instruments* **2005**, *76*.
- (8) Deheer, W. A.; Chatelain, A.; Ugarte, D. *Science* **1995**, *270*, 1179-1180.
- (9) Graham, A. P.; Duesberg, G. S.; Hoenlein, W.; Kreupl, F.; Liebau, M.; Martin, R.; Rajasekharan, B.; Pamler, W.; Seidel, R.; Steinhoegl, W.; Unger, E. *Applied Physics a-Materials Science & Processing* **2005**, *80*, 1141-1151.
- (10) Nguyen, C. V.; Ye, Q.; Meyyappan, M. *Measurement Science & Technology* **2005**, *16*, 2138-2146.
- (11) Mintmire, J. W.; Dunlap, B. I.; White, C. T. *Physical Review Letters* **1992**, *68*, 631-634.
- (12) Wildoer, J. W. G.; Venema, L. C.; Rinzler, A. G.; Smalley, R. E.; Dekker, C. *Nature* **1998**, *391*, 59-62.
- (13) Iijima, S.; Brabec, C.; Maiti, A.; Bernholc, J. *Journal of Chemical Physics* **1996**, *104*, 2089-2092.
- (14) Geim, A. K.; MacDonald, A. H. *Physics Today* **2007**, *60*, 35-41.
- (15) Kasuya, D.; Yudasaka, M.; Takahashi, K.; Kokai, F.; Iijima, S. *Journal of Physical Chemistry B* **2002**, *106*, 4947-4951.
- (16) Novoselov, K. S.; Jiang, D.; Schedin, F.; Booth, T. J.; Khotkevich, V. V.; Morozov, S. V.; Geim, A. K. *Proceedings of the National Academy of Sciences of the United States of America* **2005**, *102*, 10451-10453.
- (17) Fasolino, A.; Los, J. H.; Katsnelson, M. I. *Nature Materials* **2007**, *6*, 858-861.

- (18) Carlsson, J. M. *Nature Materials* **2007**, *6*, 801-802.
- (19) Geim, A. K.; Novoselov, K. S. *Nature Materials* **2007**, *6*, 183-191.
- (20) Novoselov, K. S.; Geim, A. K.; Morozov, S. V.; Jiang, D.; Katsnelson, M. I.; Grigorieva, I. V.; Dubonos, S. V.; Firsov, A. A. *Nature* **2005**, *438*, 197-200.
- (21) Barone, V.; Hod, O.; Scuseria, G. E. *Nano Letters* **2006**, *6*, 2748-2754.
- (22) Han, M. Y.; Ozyilmaz, B.; Zhang, Y. B.; Kim, P. *Physical Review Letters* **2007**, *98*.
- (23) Nair, R. R.; Blake, P.; Grigorenko, A. N.; Novoselov, K. S.; Booth, T. J.; Stauber, T.; Peres, N. M. R.; Geim, A. K. *Science* **2008**, *320*, 1308-1308.
- (24) Schedin, F.; Geim, A. K.; Morozov, S. V.; Hill, E. W.; Blake, P.; Katsnelson, M. I.; Novoselov, K. S. *Nature Materials* **2007**, *6*, 652-655.
- (25) Stankovich, S.; Dikin, D. A.; Dommett, G. H. B.; Kohlhaas, K. M.; Zimney, E. J.; Stach, E. A.; Piner, R. D.; Nguyen, S. T.; Ruoff, R. S. *Nature* **2006**, *442*, 282-286.
- (26) Nic, M.; Jirat, J.; Kosata, B. In *IUPAC Compendium of Chemical Terminology*; ICT, Ed. Parague, 1995.
- (27) Delhaes, P. In *World of Carbon*; Delhaes, P., Ed.; CRC Press, 2001; Vol. 1.
- (28) Mingo, N.; Broido, D. A. *Physical Review Letters* **2005**, *95*.
- (29) Saito, K.; Nakamura, J.; Natori, A. *Physical Review B* **2007**, *76*.
- (30) Arnold, L. *Windscale 1957: Anatomy of a Nuclear Accident*; Palgrave Macmillan: London, 1995.
- (31) Dresselhaus, M.; Dresselhaus, G. *Science of Fullerenes and Carbon Nanotubes*; Academic Press: New York, 1996.
- (32) Vonhelden, G.; Hsu, M. T.; Gotts, N.; Bowers, M. T. *Journal of Physical Chemistry* **1993**, *97*, 8182-8192.
- (33) Haufler, R. E.; Conceicao, J.; Chibante, L. P. F.; Chai, Y.; Byrne, N. E.; Flanagan, S.; Haley, M. M.; Obrien, S. C.; Pan, C.; Xiao, Z.; Billups, W. E.; Ciufolini, M. A.; Hauge, R. H.; Margrave, J. L.; Wilson, L. J.; Curl, R. F.; Smalley, R. E. *Journal of Physical Chemistry* **1990**, *94*, 8634-8636.
- (34) Lamb, L. D.; Huffman, D. R. *Journal of Physics and Chemistry of Solids* **1993**, *54*, 1635-1643.

- (35) Diederich, F.; Ettl, R.; Rubin, Y.; Whetten, R. L.; Beck, R.; Alvarez, M.; Anz, S.; Sensharma, D.; Wudl, F.; Khemani, K. C.; Koch, A. *Science* **1991**, *252*, 548-551.
- (36) Kroto, H. *Science* **1988**, *242*, 1139-1145.
- (37) Cheung, J. T.; Sankur, H. *Crc Critical Reviews in Solid State and Materials Sciences* **1988**, *15*, 63-109.
- (38) Howard, J. B.; Lafleur, A. L.; Makarovskiy, Y.; Mitra, S.; Pope, C. J.; Yadav, T. K. *Carbon* **1992**, *30*, 1183-1201.
- (39) Smith, B. W.; Luzzi, D. E. *Journal Of Applied Physics* **2001**, *90*, 3509-3515.
- (40) Iijima, S.; Ichihashi, T. *Nature* **1993**, *363*, 603.
- (41) Niyogi, S.; Hamon, M. A.; Hu, H.; Zhao, B.; Bhowmik, P.; Sen, R.; Itkis, M. E.; Haddon, R. C. *Accounts Of Chemical Research* **2002**, *35*, 1105-1113.
- (42) Jishi, R. A.; Dresselhaus, M. S.; Dresselhaus, G. *Physical Review B* **1993**, *47*, 16671-16674.
- (43) Treacy, M. M. J.; Ebbesen, T. W.; Gibson, J. M. *Nature* **1996**, *381*, 678.
- (44) Krishnan, A.; Dujardin, E.; Ebbesen, T. W.; Yianilos, P. N.; Treacy, M. M. J. *Physical Review B* **1998**, *58*, 14013.
- (45) Robertson, D. H.; Brenner, D. W.; Mintmire, J. W. *Physical Review B* **1992**, *45*, 12592-12595.
- (46) Falvo, M. R.; Clary, G. J.; Taylor, R. M.; Chi, V.; Brooks, F. P.; Washburn, S.; Superfine, R. *Nature* **1997**, *389*, 582-584.
- (47) Lourie, O.; Cox, D. M.; Wagner, H. D. *Physical Review Letters* **1998**, *81*, 1638-1641.
- (48) Thostenson, E. T.; Tsu-Wei, C. *Carbon* **2004**, *42*, 3003-3042.
- (49) Wang, C. Y.; Ru, C. Q.; Mioduchowski, A. *International Journal of Solids and Structures* **2003**, *40*, 3893-3911.
- (50) Akita, S.; Nakayama, Y. *Japanese Journal Of Applied Physics Part 1-Regular Papers Short Notes & Review Papers* **2003**, *42*, 3933-3936.
- (51) Liew, K. M.; Wong, C. H.; He, X. Q.; Tan, M. J.; S.A., M. *Physical Review B* **2004**, *69*, 115429.

- (52) Yu, M. F.; Yakobson, B. I.; Ruoff, R. S. *Journal Of Physical Chemistry B* **2000**, *104*, 8764-8767.
- (53) Wagner, H. D.; Lourie, O.; Feldman, Y.; Tenne, R. *Applied Physics Letters* **1998**, *72*, 188-190.
- (54) Hu, Y. H.; Sinnott, S. B. *Journal Of Materials Chemistry* **2004**, *14*, 719-729.
- (55) Xia, Z.; Curtin, W. A. *Physical Review B* **2004**, *69*, 233408.
- (56) Huhtala, M.; Krasheninnikov, A. V.; Aittoniemi, J.; Stuart, S. J.; Nordlund, K.; Kaski, K. *Physical Review B* **2004**, *70*, 045404.
- (57) Callister, W. D. *Materials Science and Engineering and Introduction*; 4th ed.; John Wiley & Sons, Inc.: New York, 1997.
- (58) Thostenson, E. T.; Li, C. Y.; Chou, T. W. *Composites Science and Technology* **2005**, *65*, 491-516.
- (59) Chawla, K. *Composites Materials Science and Engineering*; 2nd ed.; Springer: New York, 1998.
- (60) Gojny, F. H.; Wichmann, M. H. G.; Kopke, U.; Fiedler, B.; Schulte, K. *Composites Science And Technology* **2004**, *64*, 2363-2371.
- (61) Ajayan, P. M.; Schadler, L. S.; Braun, P. V. *Nanocomposites Science and Technology*; Wiley-VCH: Weinheim, 2003.
- (62) Sinnott, S. B.; Shenderova, O. A.; White, C. T.; Brenner, D. W. *Carbon* **1998**, *36*, 1-9.
- (63) Hu, Y. H.; Shenderova, O. A.; Hu, Z.; Padgett, C. W.; Brenner, D. W. *Reports on Progress in Physics* **2006**, *69*, 1847-1895.
- (64) Wang, Y. *Nature* **1992**, *356*, 585-587.
- (65) Sariciftci, N. S.; Smilowitz, L.; Heeger, A. J.; Wudl, F. *Science* **1992**, *258*, 1474-1476.
- (66) Uchida, S.; Xue, J. G.; Rand, B. P.; Forrest, S. R. *Applied Physics Letters* **2004**, *84*, 4218-4220.
- (67) Veenstra, S. C.; Malliaras, G. G.; Brouwer, H. J.; Esselink, F. J.; Krasnikov, V. V.; vanHutten, P. F.; Wildeman, J.; Jonkman, H. T.; Sawatzky, G. A.; Hadzioannou, G. *Synthetic Metals* **1997**, *84*, 971-972.
- (68) Yoo, S.; Domercq, B.; Kippelen, B. *Applied Physics Letters* **2004**, *85*, 5427-5429.

- (69) Lee, K.; Kim, H. *Current Applied Physics* **2004**, *4*, 323-326.
- (70) Tai, N. H.; Yeh, M. K.; Liu, H. H. *Carbon* **2004**, *42*, 2774-2777.
- (71) Ogasawara, T.; Ishida, Y.; Ishikawa, T.; Yokota, R. *Composites Part A-Applied Science And Manufacturing* **2004**, *35*, 67-74.
- (72) Thostenson, E. T.; Chou, T. W. *Journal Of Physics D-Applied Physics* **2003**, *36*, 573-582.
- (73) Thostenson, E. T.; Ren, Z. F.; Chou, T. W. *Composites Science and Technology* **2001**, *61*, 1899-1912.
- (74) Schadler, L. S.; Giannaris, S. C.; Ajayan, P. M. *Applied Physics Letters* **1998**, *73*, 3842-3844.
- (75) Qian, D.; Dickey, E. C.; Andrews, R.; Rantell, T. *Applied Physics Letters* **2000**, *76*, 2868-2870.
- (76) Frankland, S. J. V.; Caglar, A.; Brenner, D. W.; Griebel, M. *Journal Of Physical Chemistry B* **2002**, *106*, 3046-3048.
- (77) Frankland, S. J. V.; Harik, V. M. *Surface Science* **2003**, *525*, L103-L108.
- (78) Ajayan, P. M.; Schadler, L. S.; Giannaris, C.; Rubio, A. *Advanced Materials* **2000**, *12*, 750-+.
- (79) Hu, Y.; Jang, I.; Sinnott, S. B. *Composites Science And Technology* **2003**, *63*, 1663-1669.
- (80) Sinnott, S. B. *Journal Of Nanoscience And Nanotechnology* **2002**, *2*, 113-123.
- (81) Garg, A.; Sinnott, S. B. *Chemical Physics Letters* **1998**, *295*, 273-278.
- (82) Srivastava, D.; Brenner, D. W.; Schall, J. D.; Ausman, K. D.; Yu, M. F.; Ruoff, R. S. *Journal of Physical Chemistry B* **1999**, *103*, 4330-4337.
- (83) Banhart, F. *Reports On Progress In Physics* **1999**, *62*, 1181-1221.
- (84) Krasheninnikov, A. V.; Nordlund, K. *Nuclear Instruments & Methods In Physics Research Section B-Beam Interactions With Materials And Atoms* **2004**, *216*, 355-366.
- (85) Astrom, J. A.; Krasheninnikov, A. V.; Nordlund, K. *Physical Review Letters* **2004**, *93*, 215503.
- (86) Iwata, T.; Nihira, T. *Journal Of The Physical Society Of Japan* **1971**, *31*, 1761-&.

- (87) Sun, L. T.; Gong, J. L.; Wang, Z. X.; Zhu, D. Z.; Hu, J. G.; Lu, R. R.; Zhu, Z. Y. *Nuclear Instruments & Methods In Physics Research Section B-Beam Interactions With Materials And Atoms* **2005**, 228, 26-30.
- (88) Telling, R. H.; Ewels, C. P.; El-Barbary, A. A.; Heggie, M. I. *Nature Materials* **2003**, 2, 333-337.
- (89) Iwata, T.; Nihira, T. *Physics Letters* **1966**, 23, 631-&.
- (90) Ohr, S.; Wolfenden, A.; Noogle, T. *Electron Microscopy and Structure of Materials*; University of California Press: Berkeley, 1972.
- (91) Montet, G. L.; Myers, G. E. *Carbon* **1971**, 9, 179-&.
- (92) Volpel, R.; Hofmann, G.; Steidl, M.; Stenke, M.; Schlapp, M.; Trassl, R.; Salzborn, E. *Physical Review Letters* **1993**, 71, 3439-3441.
- (93) Banhart, F.; Ajayan, P. M. *Nature* **1996**, 382, 433-435.
- (94) Wang, S.; Buseck, P. R. *Chemical Physics Letters* **1991**, 182, 1-4.
- (95) Krive, I. V.; Shekhter, R. I.; Jonson, M. *Low Temperature Physics* **2006**, 32, 887-905.
- (96) Hu, Y. H.; Irving, D. L.; Sinnott, S. B. *Chemical Physics Letters* **2006**, 422, 137-141.
- (97) Bandow, S.; Hiraoka, T.; Yumura, T.; Hirahara, K.; Shinohara, H.; Iijima, S. *Chemical Physics Letters* **2004**, 384, 320-325.
- (98) Masonori, K.; Kazutomo, S.; Suenaga, K.; Nakamura, E. *Fullerene, Nanotubes General Symposium* **2006**, 30, 171.
- (99) Prawer, S.; Nugent, K. W.; Biggs, S.; McCulloch, D. G.; Leong, W. H.; Hoffman, A.; Kalish, R. *Physical Review B* **1995**, 52, 841-849.
- (100) Musket, R. G.; Hawleyfedder, R. A.; Bell, W. L. *Radiation Effects and Defects in Solids* **1991**, 118, 225-235.
- (101) Stone, A. J.; Wales, D. J. *Chemical Physics Letters* **1986**, 128, 501-503.
- (102) Banhart, F. *Nano Letters* **2001**, 1, 329-332.
- (103) Guan, L. H.; Shi, Z. J.; Gu, Z. N. *Carbon* **2005**, 43, 1101-1103.
- (104) Jang, I.; Sinnott, S. B.; Danailov, D.; Keblinski, P. *Nano Letters* **2004**, 4, 109-114.

- (105) Krasheninnikov, A. V.; Nordlund, K.; Keinonen, J.; Banhart, F. *Physical Review B* **2002**, *66*, 245403.
- (106) Terrones, M.; Banhart, F.; Grobert, N.; Charlier, J. C.; Terrones, H.; Ajayan, P. M. *Physical Review Letters* **2002**, *89*, 075505.
- (107) Wang, Z. X.; Yu, L. P.; Zhang, W.; Ding, Y. F.; Li, Y. L.; Han, J. G.; Zhu, Z. Y.; Xu, H. J.; He, G. W.; Chen, Y.; Hu, G. *Physics Letters A* **2004**, *324*, 321-325.
- (108) Pregler, S. K.; Sinnott, S. B. *Physical Review B* **2006**, *73*, 224106.
- (109) Bhowmik, S.; Bonin, H. W.; Bui, V. T.; Weir, R. D. *Journal of Applied Polymer Science* **2006**, *102*, 1959-1967.
- (110) Peumans, P.; Forrest, S. R. *Applied Physics Letters* **2001**, *79*, 126-128.
- (111) Peumans, P.; Uchida, S.; Forrest, S. R. *Nature* **2003**, *425*, 158-162.
- (112) Xue, J. G.; Rand, B. P.; Uchida, S.; Forrest, S. R. *Journal of Applied Physics* **2005**, *98*, -.
- (113) Dimitrakopoulos, C. D.; Malenfant, P. R. L. *Advanced Materials* **2002**, *14*, 99-+.
- (114) Tang, C. W. *Appl. Phys. Lett.* **1986**, *48*, 183-185.
- (115) Peumans, P.; Yakimov, A.; Forrest, S. R. *Journal of Applied Physics* **2003**, *93*, 3693-3723.
- (116) Heo, S. J., 2007.
- (117) Fischer, J. E. *Chemical Innovation* **2000**, *30*, 21-27.
- (118) Xue, J. G.; Sinnott, S. B., 2006.
- (119) Allen, M. P.; Tildesley, D. J. *Computer Simulation of Liquids*; Oxford University Press: New York, 1987.
- (120) Frenkel, D.; Smit, B. *Understanding Molecular Simulation*; Academic Press: San Diego, 1996.
- (121) Tersoff, J. *Physical Review Letters* **1988**, *61*, 2879-2882.
- (122) Brenner, D. W. *Physical Review B* **1990**, *42*, 9458-9471.
- (123) Brenner, D. W.; Shenderova, O. A.; Harrison, J. A.; Stuart, S. J.; Ni, B.; Sinnott, S. B. *Journal Of Physics-Condensed Matter* **2002**, *14*, 783-802.

- (124) Jang, I.; Phillips, R.; Sinnott, S. B. *Journal Of Applied Physics* **2002**, *92*, 3363-3367.
- (125) Ni, B.; Lee, K. H.; Sinnott, S. B. *Journal of Physics-Condensed Matter* **2004**, *16*, 7261-7275.
- (126) Bethe, H. *Statistical Theory of Super Lattices*; Proc. Roy. Soc.: London, 1939.
- (127) Stuart, S. J.; Tutein, A. B.; Harrison, J. A. *Journal Of Chemical Physics* **2000**, *112*, 6472-6486.
- (128) Adelman, S. A.; Doll, J. D. *Journal Of Chemical Physics* **1976**, *64*, 2375-2388.
- (129) Evans, D. J.; Morriss, G. P. *Statistical Mechanics of Nonequilibrium Liquids*; 2nd ed.; ANU E Press: Canberra.
- (130) Koike, J.; Pedraza, D. F. *Journal Of Materials Research* **1994**, *9*, 1899-1907.
- (131) Pregler, S. K.; Hayakawa, T.; Yasumatsu, H.; Kondow, T.; Sinnott, S. B. *Nuclear Instruments & Methods in Physics Research Section B-Beam Interactions with Materials and Atoms* **2007**, *262*, 240-248.
- (132) Yasumatsu, H.; Hayakawa, T.; Koizumi, S.; Kondow, T. *Journal Of Chemical Physics* **2005**, *123*.
- (133) Muto, S.; Tanabe, T. *Philosophical Magazine A-Physics Of Condensed Matter Structure Defects And Mechanical Properties* **1997**, *76*, 679-690.
- (134) Mochiji, K.; Yamamoto, S.; Shimizu, H.; Ohtani, S.; Seguchi, T.; Kobayashi, N. *Journal Of Applied Physics* **1997**, *82*, 6037-6040.
- (135) Li, L.; Reich, S.; Robertson, J. *Physical Review B* **2005**, *72*.
- (136) Xu, C. H.; Fu, C. L.; Pedraza, D. F. *Physical Review B* **1993**, *48*, 13273-13279.
- (137) Ewels, C. P.; Telling, R. H.; El-Barbary, A. A.; Heggie, M. I.; Briddon, P. R. *Physical Review Letters* **2003**, *91*.
- (138) Kelly, B. *The Physics of Graphite*; Applied Science: London, 1981.
- (139) Chandra, N.; Namilae, S.; Shet, C. *Physical Review B* **2004**, *69*, 094101.
- (140) Jensen, P.; Gale, J.; Blase, X. *Physical Review B* **2002**, *66*.
- (141) Zhou, L. G.; Shi, S. Q. *Applied Physics Letters* **2003**, *83*, 1222-1224.
- (142) Delcorte, A.; Garrison, B. J. *Journal Of Physical Chemistry B* **2004**, *108*, 15652-15661.

- (143) Sammalkorpi, M.; Krasheninnikov, A. V.; Kuronen, A.; Nordlund, K.; Kaski, K. *Nuclear Instruments & Methods In Physics Research Section B-Beam Interactions With Materials And Atoms* **2005**, 228, 142-145.
- (144) Frankland, S. J. V.; Harik, V. M.; Odegard, G. M.; Brenner, D. W.; Gates, T. S. *Composites Science and Technology* **2003**, 63, 1655-1661.
- (145) Yang, F.; Shtein, M.; Forrest, S. R. *Nature Materials* **2005**, 4, 37-41.
- (146) Coakley, K. M.; Liu, Y. X.; McGehee, M. D.; Frindell, K. L.; Stucky, G. D. *Advanced Functional Materials* **2003**, 13, 301-306.
- (147) Troullier, N.; Martins, J. L. *Physical Review B* **1992**, 46, 1754-1765.
- (148) Northrup, J. E.; Tiago, M. L.; Louie, S. G. *Physical Review B* **2002**, 66, -.
- (149) Onoda, G. Y.; Liniger, E. G. *Physical Review A* **1986**, 33, 715-716.
- (150) Zheng, Y.; Pregler, S. K.; Myers, J.; Sinnott, S. B.; Xue, J. G. *Journal Of Applied Physics* **2008**, *in prep.*
- (151) Northrup, J. E.; Tiago, M. L.; Louie, S. G. *Physical Review B* **2002**, 66.

BIOGRAPHICAL SKETCH

Sharon Pregler was born in Cebu City, Philippines in 1981 to Command Master Chief John J. Pregler and pre-school teacher Norma. M. Pregler. As part of a military family, she has traveled various parts of the world and lived in many places including Hawaii, Japan, California, and Washington. She has lived in Florida since 1996 and graduated from Orange Park High School in 1999. She received her B.S. in 2003 from the University of Florida's Materials Science and Engineering department and a Ph.D. in Materials Science and Engineering in 2008 in the Department of Materials Engineering at the University of Florida with Dr. Susan B. Sinnott.